Lateral spintronic device application of molecular beam epitaxial grown MnAs/III-As hybrid structures on GaAs(111)B

Md. Earul Islam

Japan Advanced Institute of Science and Technology, Japan

Doctoral Dissertation

Lateral spintronic device application of molecular beam epitaxial grown MnAs/III-As hybrid structures on GaAs(111)B

Md. Earul Islam

Supervisor: Associate Professor Dr. Masashi Akabori

School of Materials Science

Japan Advanced Institute of Science and Technology, Japan

March, 2018

Abstract

In spintronics electron spin is used as information carrier in addition to its charge. It is already well established metal-based spin-devices practical applications. To use spin degree of freedom into semiconductor spintronic device technology such as in spin field effect transistor (spin-FET), there are three main technological challenges are, firstly, injection of spin polarized carrier from a ferromagnetic (FM) into semiconductor (SC) channel and detection by FM, secondly, SC channel should have strong spin-orbit coupling (SOC) to precess spin during transport through SC channel, and finally, control of the spin precession by gate electric field to modulate spin signal. Therefore, exploring promising FM/SC hybrid structures are important. Here, we synthesized MnAs/III-As hybrid structures on GaAs(111)B as a possible candidate for future spin-FET and investigated the first challenging issue into the hybrid structures. We carried out successful molecular beam epitaxial (MBE) growth of MnAs(~5-200 nm)/GaAs(~0-10 nm)/thick-InAs(~200-1200 nm) /GaAs(111)B hybrid structures at low temperature MnAs epitaxial growth. In reflection high energy electron diffraction (RHEED) study, we see double step lattice transition ~4 nm of InAs from GaAs surface and abrupt lattice transition of GaAs ~3.6 nm from InAs lattice respectively. The origin of these transition is still unclear for such lattice mismatch growth. In 2θ x-ray diffraction (XRD) measurement of MnAs(~200 nm)/thick-InAs(~1200 nm) /GaAs(111)B, we see single phase epitaxial growth of hexagonal MnAs with cubic InAs and GaAs (only low temperature MnAs growth case). Also, the extracted lattice parameters are consistent with their bulk values which imply that the grown epitaxial layers are strain relaxed. To check deviation of c-axis, we carried out ω scanning. From ω and 2θ measurement, we also observed less deviation (InAs ~0.12° and MnAs~0.22°) of c-axis normal to the planes of thicker MnAs(200 nm) and InAs(1200 nm) layers. Hence, the 2θ and ω scanning indicates good epitaxial growth of MnAs and InAs. We also estimated thickness dependence threading dislocation density from the ω-θ broadening, we found reduction of the dislocation density with increasing grown layer thickness. It means better crystal quality in thicker case. Also comparatively, InAs shows less dislocation density in similar thickness than that of on GaAs(001). Besides, we also confirmed smooth surface and maze-like magnetic structures by atomic force microscopy (AFM) and magnetic force microscopy (MFM). The MnAs ~5-200 nm samples show strong magnetic anisotropy along [-2110] and [01-10] lateral and [0001] out of plane directions by superconducting quantum interference device (SQUID) magnetometry. It also reveals easy and isotropic magnetization in lateral directions which is similar to MnAs directly on GaAs(111)B. We also see higher

MnAs thickness higher saturation magnetization and lower coercive field which seems directly related to the crystal quality. The better the crystal quality the better the magnetic response. It also shows over room temperature (~300 K) magnetism (estimated Curie temperature ~320-324 K). However, to evaluate contact between MnAs/InAs on GaAs(111)B, we studied transmission line model (TLM) device and found isotropic Ohmic behaviors in lateral [-110] and [11-2] directions of cubic InAs. Specific contact resistance, of MnAs/InAs interface at ~300 K is ~(10^{-5}-10^{-4}) Ω-cm^2 which is little higher than typical Ohmic contact. However, over room temperature isotropic magnetic and isotropic electric behaviors in lateral directions gives good flexibility to design lateral spintronic device. We studied trials of lateral spin valve device of MnAs (~50 nm)/GaAs (~1, 3)/InAs (~200 nm)/GaAs(111)B grown samples in lateral spin valve device application. Through the study, we improved device processing and carried out lateral spin valve measurement using AC lock in technique. We successfully confirmed spin injection and detection through simultaneous local spin valve (LSV) and non-local spin valve (NLSV) measurements in lateral spin valve device of 1 nm GaAs barrier insertion sample at 1.5 K. We obtained large spin diffusion length ~10 μm and spin injection efficiency ~1.6% which is similar to other FM/narrow gap hybrid structures. However, ~2.0 time enhancement of NLSV signal can also be seen in FM-FM input case than that of FM-NM input case. On the other hand, at 300 K, the extracted spin diffusion length ~2.6 μm and spin injection efficiency ~6.3% which is significantly large value in comparison to other FM/narrow gap hybrid structures at 300 K. The enhancement of spin injection efficiency at 300 K is due to better impedance matching between MnAs/InAs rather than at 1.5 K.

In conclusion, we can say that large spin injection efficiency ~6.3 % of the hybrid structure is record value at ~300 K which is very promising for future spin-FET application. Further, higher GaAs thickness dependence investigations are necessary to clarify spin injection efficiency more in details as well as other two challenging issues also have to be investigated before approaching spin-FET applications.

Keywords: 1. Molecular beam epitaxy (MBE), 2. MnAs, InAs, GaAs(111)B, 3. Magnetic properties, 4. Electrical properties, 5. Lateral spin valve

Acknowledgments

I have had the opportunity over the past three years to meet and work with many talented people around me. It is only thanks to their guidance, support, and friendly response that I have experienced at Japan Advanced Institute of Science and Technology (JAIST). First of all, I am grateful to my supervisor, Associate Professor Masashi Akabori, for his encouragement, support, and guidance throughout my graduate study. This thesis would not have been possible without him. He has taught me beyond what is expected of a graduate student advisor and will remain a constant source of inspiration. I admire him as a good researcher, as a true leader, and as a genuinely good and fun person around me.

I would like to express my sincere gratitude to Professor Toshi-kazu Suzuki for his fruitful comments on my research and encouragement about learning and enjoying life at JAIST.

I also would like to express my sincere appreciation to Associate Professor Toshu An for his kind support on my sub-theme in his laboratory and also valuable comments on my major research work to understand in depth.

I also would like to express my sincere gratitude to Professor Mikio Koyano to become a reviewer of my PhD thesis. I appreciate his valuable comments on my research.

I also would like to express my sincere gratitude to Prof. Shinjiro Hara to become a reviewer of my PhD thesis. I appreciate his value comments on my research to understand from the basic point to in depth considerations.

I am also sincerely grateful to post-doc Dr. Cong Thanh Nguyen for his constant help and suggestions in the early stage of my PhD program. I am also would like to give thanks to one graduated student Kazuki Hayashida for spin valve device fabrication for my research purpose. I also would like give thanks to rest of the lab members for keeping friendly atmosphere in the

laboratory. I also would like to express my sincere gratitude to Professor Abu Bakar Md. Ismail, University of Rajshahi, Bangladesh, for his constant mental support in my bad days.

Finally, I would like to pray for my late mother without she I could not reach here today.

Contents

Chapters

1 Introduction

2 Epitaxial growth of MnAs/III-As on GaAs(111)B and its structural, electrical and magnetic characterizations

Chapter 1

Introduction

1.1 Spintronics overview

It is already well-established of electronic charge flow and manipulation in semiconductor electronic devices. The charge of electrons and holes is used as primary information carrier. The spin of electrons in addition to the charge has already unlocked way for a wide range of new device structures. Particularly, in metal based magneto-electronics, spin and charge properties of electrons are applied to obtain magneto-resistance effects like giant magneto-resistance (GMR) [1,2] tunnel magneto-resistance (TMR) [3,4] for hard disks and magnetic random access memory (MRAM) [5] for practical applications. To use spin degree of freedom with existing semiconductor technology, a related research field called semiconductor spintronic already has been emerged. In semiconductor spintronic, spin-field-effect transistor (spin-FET) and spin metal-oxide-semiconductor field-effect transistor (spin-MOSFET) which are expected to have features like non-volatility, reconfigurable logic functions and low power consumption [6-8] devices. The spin transistors require to have ferromagnetic (FM) metal source and drain for spin polarized charge carrier injection and detection, semiconducting channel for coherent spin-polarized charge carrier transport, and a gate electric field for the transport control. A combination of ferromagnetic (FM)/semiconductor (SC) hybrid structure is expected to be promising candidate for semiconductor spintronic to meet the basic requirements to realize device functionalities. For coherent-transport, spin lifetime within semiconductor necessarily to have long to be used in spintronic device. Usually semiconductor have longer spin lifetime than metal. In GaAs [9] the spin-coherent lifetime is long enough for device purposes but different semiconductors are likely to be rather different, and for devices

requiring III-V materials other than the well-studied GaAs, problems still remain. Also spin polarized charge carrier can be made to flow in the same way as conventional carrier by applying longitudinal electric field, or made to precess by transverse electric field as described by Datta and Das [6]. Favored detection of spin polarized charge carrier can be achieved using ferromagnetic contacts. However, materials for spin generation is foremost condition to realize the spintronic devices.

1.1.1 Materials for spin generation

We know, electrons have an intrinsic spin, which have two states, spin up (s =1/2) or spin down (s = -1/2). In an un-polarized charge currents, number of electrons in each spin state is equal. The number of spin up electrons with an energy E is expressed by the density of states (DOS) $N_{\uparrow}(E_f)$, and those with spin down by $N_{\downarrow}(E_f)$.The spin polarization P is defined as the ratio of the density of states of spin up and spin down electrons at a Fermi level is given by;

$$P = \frac{N_{\uparrow}(E_f) - N_{\downarrow}(E_f)}{N_{\uparrow}(E_f) + N_{\downarrow}(E_f)} \quad (1.1)$$

In order to act as a spin source a solid state spin injector is required to have unequal spin up and spin down DOS at the Fermi level. Figure 1.1 shows the DOS for three classes of materials. From Fig.1.1 (a), we see the density of states of spin up and spin down electrons are equal in paramagnetic materials, P=0 because DOS of spin up and spin down are equal. On the other hand, the density of state of spin up and spin down are different in ferromagnetic materials, P>0 but smaller than 1 as shown in Fig.1.1 (b). If a material has a band gap in the minority band at a Fermi level and shows metallic behavior in the majority band, the density of state of the minority band is zero at the Fermi level. In this case, only up-spin electrons are present at

the Fermi level, P=1 as shown in Fig.1.1 (c). This type of material is called half-metal because it shows both metallic and semiconducting behaviors.

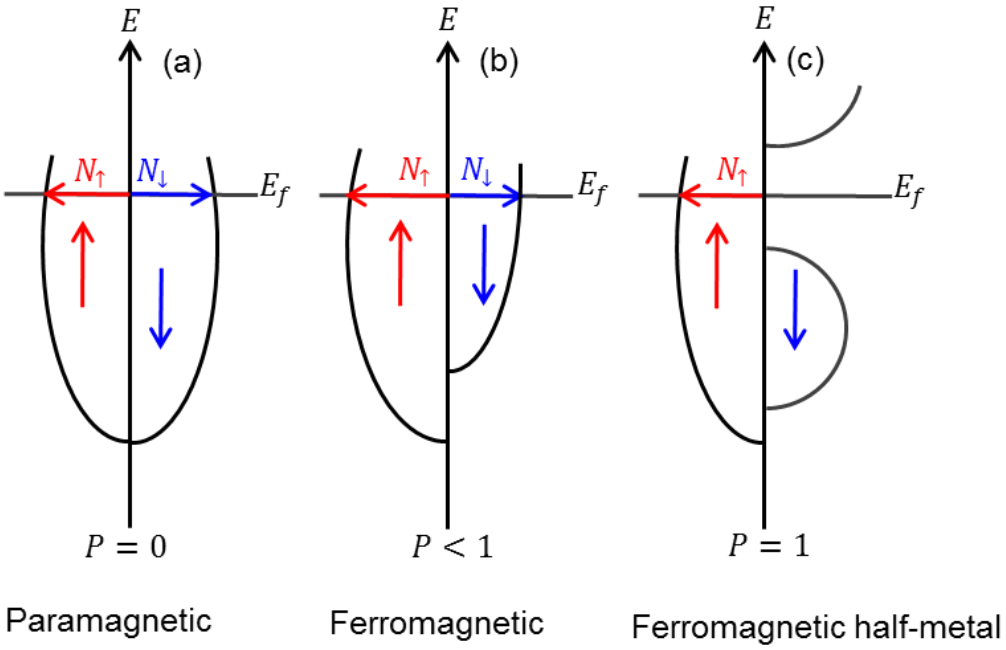

Fig.1.1 Density of states of (a) Paramagnetic, (b) Ferromagnetic and (c) Ferromagnetic half-metal materials.

We can clearly see only ferromagnetic materials can be used as a source of spin. There are four types of FM materials have been well studied for potential spin source are:

1. Dilute magnetic semiconductors (DMSs)
2. Ferromagnetic metals
3. ferromagnetic alloys
4. Half metallic ferromagnets (HMFs)

DMSs can be developed by doping non-magnetic semiconductor with magnetic ions such as transition metals (Mn, Fe, Ni, Co, etc.) or rare earth elements (Gd, Eu, Er, etc.) [10]. For example doping III-V semiconductors with magnetic atoms such as Mn. Into $Ga_{1-x}Mn_xAs$, the

Mn takes up a substitutional Ga site and acts as an acceptor. The resulting holes facilitate ferromagnetism in the material [11]. The other three injection materials act as part of hybrid system, in which non-semiconductor based magnetic materials as spin source. A wide range of materials including FM metals such as Fe, Co, Ni, ferromagnetic alloys, such as CoFe, NiFe oxides (CrO_2) and pnictides MnAs, MnSb, and HMFs such as NiMnSb and Co_2FeSi-Heusler alloy etc. However, a number of problems exist for hybrid spintronic devices, arising as a result of considerable structural, electronic and chemical differences between injection material and semiconductor.

1.1.2 Semiconductor materials for spintronic

Semiconductor materials that are used in existing electronic technology have been studied to search their applicability into spintronic devices. Commonly used semiconductor materials have already attained interest to researcher are Si, Ge, GaAs, InAs, InAlAs and InP and single-/bi-layer graphene etc. for future spintronic device application.

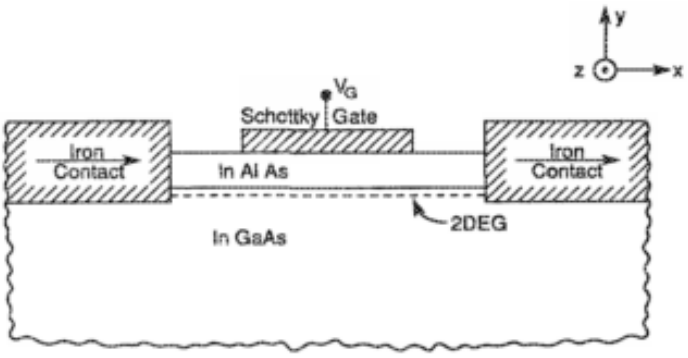

Fig.1.2 Schematic diagram of Datta Das type spin-FET [6].

We are particularly interested in spin-FET. Figure 1.2 shows a schematic diagram of spin-FET proposed by Datta and Das in 1990. For spin-FET, narrow gap two dimensional electron gas (2DEG) semiconductors are important as a channel material because narrow gap semiconductors show strong spin-orbit coupling (SOC) which is pre-requisite to realize spin-FET operation. SOC enables to control effective magnetic field in semiconductors by external gate electric field [12, 13] and hence control of spin-polarized carriers in semiconductors channel [14, 15]. However, semiconductors having weak SOC are expected to have long spin coherence, but it is difficult to control carrier spin by the electric field. Thus, generally the strength of the spin coherence length and SOC are in a trade-off relationship. The basic discussion about SOC has been discussed in appendix-A1.

1.1.3 Spin injection and detection into FM/SC hybrid structures

Electrical bias field, E across FM/SC creates non-equilibrium spin density in SC. Spin injection is known as spin-polarized charge current follow from FM to SC.

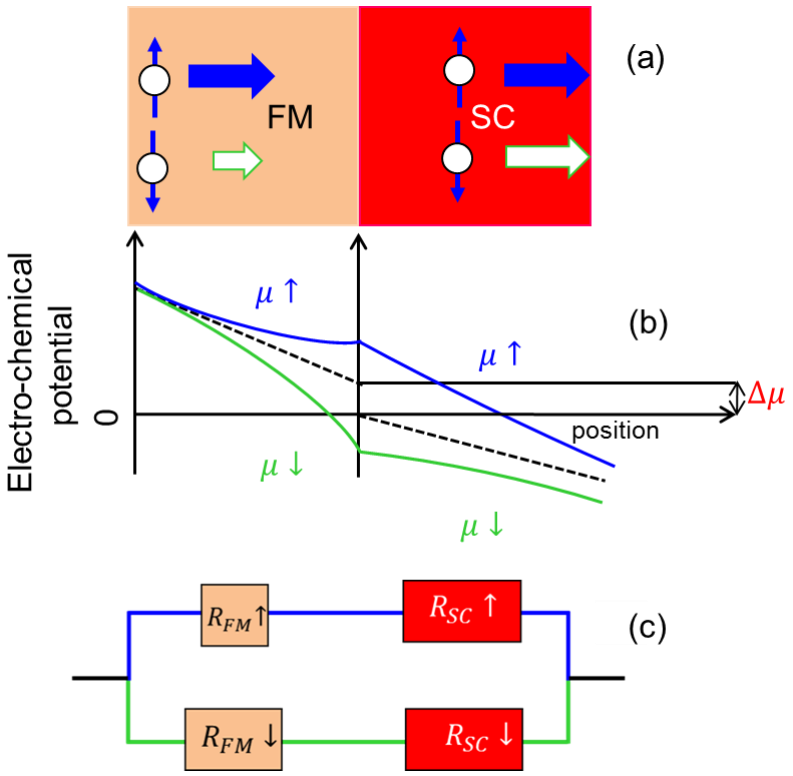

Fig.1.3 (a) FM/SC contact (assume electrical bias between FM/SC), (b) Electrochemical potential for up spin down spin electrons in FM/SC decaying profile. (c) Spin current flow model up spin and down spin electrons in FM/SC.

Also opposite direction of current flow creates non-equilibrium spin density in SC, it is known as spin extraction. Figure. 1.3 (a) shows FM/SC contact. Two spin orientations (up and down) have different resistivities i.e different density. Therefore, current density of two different spin in FM/SC hybrid structure are generally not equal. Flow of electrons spin current $j_{\uparrow,\downarrow}$ is indicated by the sum of drift current due to electric field and diffusion current due to concentration gradient. The flow of spin can be represented by using Einstein relation as;

$$D_{\uparrow,\downarrow} = \frac{\sigma_{\uparrow,\downarrow}}{e^2 N_{\uparrow,\downarrow}} \quad (1.2)$$

Where, $D_{\uparrow,\downarrow}$ and $\sigma_{\uparrow,\downarrow}$ are spin dependent diffusion constant and conductivity respectively, and e is electron charge. Therefore,

$$j_{\uparrow,\downarrow} = -E\sigma_{\uparrow,\downarrow} - eD_{\uparrow,\downarrow}\Delta n_{\uparrow,\downarrow}$$

$$j_{\uparrow,\downarrow} = \frac{-\sigma_{\uparrow,\downarrow}}{e}\left(e\Delta\phi + \frac{\Delta n_{\uparrow,\downarrow}}{eN_{\uparrow,\downarrow}}\right) (1.3)$$

Where, E and ϕ are electric field and electrostatic potential respectively and $\frac{\Delta n_{\uparrow,\downarrow}}{eN_{\uparrow,\downarrow}}$ is the electrochemical potential of spin. Now, we can use them as $\mu_{\uparrow,\downarrow} \equiv e\phi + \frac{n_{\uparrow,\downarrow}}{eN_{\uparrow,\downarrow}}$ then equation (1.3) can be written as;

$$j_{\uparrow,\downarrow} = \frac{-\sigma_{\uparrow,\downarrow}}{e}\left(\Delta\mu_{\uparrow,\downarrow}\right) (1.4)$$

Therefore, we defined the currents $j_{\uparrow,\downarrow}$ dependent on spin, which shows that the currents $j_{\uparrow,\downarrow}$ flow by the gradient of the electrochemical potential which define spin accumulation. The electro-chemical potential difference can be define as,

$$\Delta\mu = \mu_{\uparrow} - \mu_{\downarrow} (1.5)$$

$\Delta\mu$ represents non-equilibrium state having non-zero value result in spin relaxation decays exponentially in SC with spin diffusion lengths L_S. The spin current relaxation behavior of FM/SC is shown in Fig. 1.3 (a) and (b). When the SC has large resistivity in comparison with FM results in inefficient spin injection [16, 17]. This is known as conductivity mismatch or impedance mismatch problem in typical FM/SC hybrid structure. Figure.1.3 (c) shows a schematic of two current flow resistor model for the two spin channel. In the model, the

resistance for up spin and down spin are same in SC, $R_{SC\uparrow} = R_{SC\downarrow}$ but different in FM assume, $R_{FM\uparrow} < R_{FM\downarrow}$. Usually, in FM/SC contacts $R_{SC} \gg R_{FM\uparrow,\downarrow}$, total currents are equal for both spin channels as a result spin injection is insufficient [18]. Alongside spin relaxation into FM and SC are also important. However, $R_{SC} \gg R_{FM\uparrow,\downarrow}$ suggests to improve impedance mismatch problems by alternative ways like spin injection from a FM half metal having 100% spin polarization [17] or spin injection through a tunnel barrier contact [19-21]. A tunnel barrier into FM/SC, introduce tunnel contact resistance r_c, in series with R_{SC} and $R_{FM\uparrow,\downarrow}$. We can get improve impedance mismatch problem from $R_{SC} \gg R_{FM\uparrow,\downarrow}$ condition by tunnel barrier contact if and only if, $r_c \gtrsim R_{SC}$ [19].

There are two common electrical techniques called local and non-local spin valve (LSV and NLSV) measurement to evaluate spin injection and detection into FM/SC hybrid structures. Here, the meaning of local is that the spin valve signal is mediated and directly influenced by local drift electric field as represented by equation 1.3. In LSV measurements, spin-polarized charge current injection and detection is performed locally between two FM electrodes. The LSV configuration is shown in Fig.1.4 (a). The two-terminal LSV resistance can be modulated similar way to GMR [1, 2] and TMR [3, 4] operation. LSV using SC channel interesting in semiconductor spintronic device concepts [6-8] except manipulation mechanism during spin transport. The conceptual devices require efficient spin injection, transport, and detection in lateral LSV. In addition, in LSV measurement, due to flowing of spin polarized charge current in the local channel there are possibilities to affect the intrinsic signal of interest by drift electric field [22] anisotropic magnetoresistance (AMR) [23] or local Hall effect (LHE) [24]. On the other hand, in NLSV measurement such spurious effect can be avoided [25, 26] because charge current and spin current are separated in non-local arrangement. This means, NLSV study provides more direct evidence of spin injection, transport and detection into FM/SC hybrid structure. The NLSV configuration is shown Fig.1.4 (b). Therefore, both LSV and NLSV are

equally important to investigate spin injection and detection to approach semiconductor spintronic device technology.

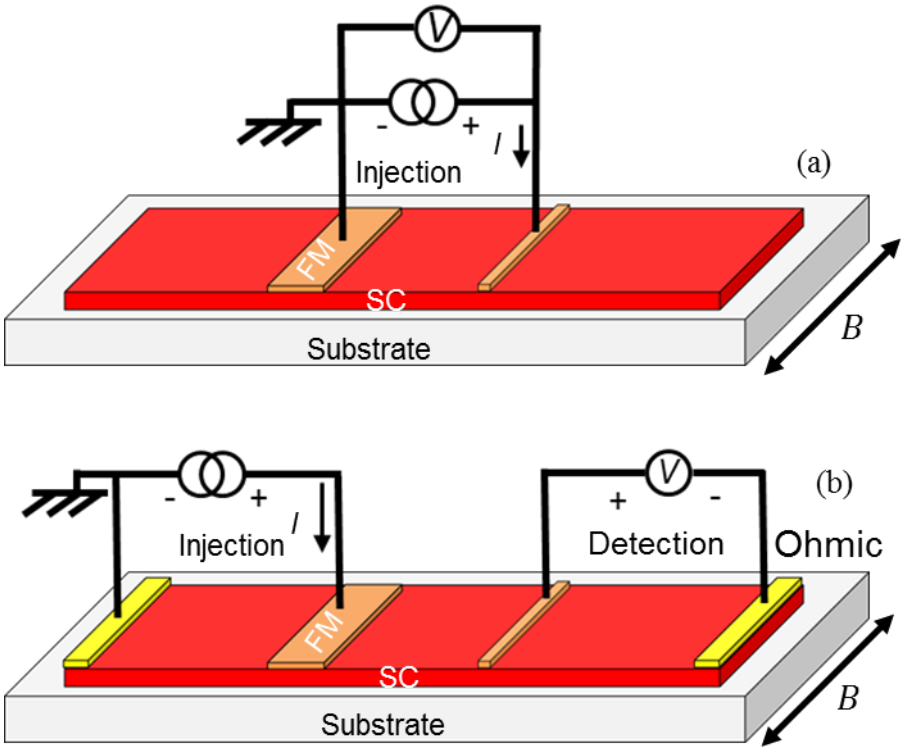

Fig 1.4 Schematic of spin valve measurement configurations (a) LSV (b) NLSV. *I* and *V* input current and measured voltage respectively.

It is obvious to have spin valve signal, we require two different aspect ratio size FM electrodes having different magnetization hysteresis behaviors. Usually, high aspect ratio of FM electrode

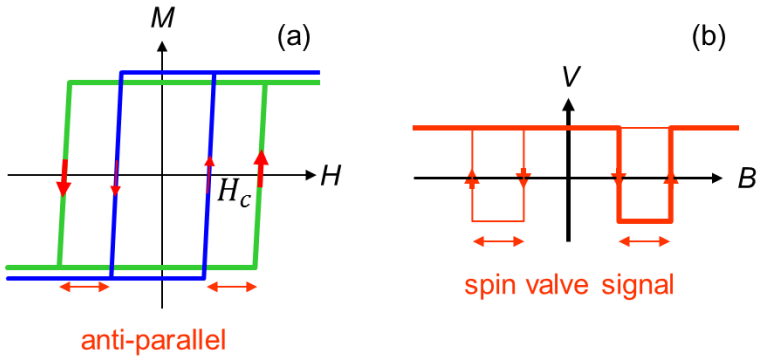

Fig 1.5 (a) Conceptual magnetization difference of low aspect (blue line) and high aspect ratio (green line) FM. (b) Ideal hysteresis behavior in spin valve

shows higher coercive field (H_c) compared to that of low aspect ratio FM electrode as shown in Fig.1.5 (a). The parallel and anti-parallel state between two FM gives hysteresis behavior in spin valve measurement as shown in Fig.1.5 (b). There are numerous FM/SC combination such as Fe [27], $FeSi_3$ [28] and CoFe [29] with Si; Co [30], Co_2FeSi-Heusler alloy[31] with Graphene; CoFe [32], Fe [33] and Co_2FeSi-Heusler alloy [34] with GaAs; and Ni [35] and NiFe [36] with InAs trials have been conducted spin valve measurements to reveal spin injection and detection in those hybrid structures to check their candidacy for semiconductor spintronic device application [6-8]. To this end, to approach future spin-FET, we consider, combination of MnAs/III-As hybrid structure as a base structure.

1.2 Motivation and organization of the thesis

Usually ferromagnetic transition metals like Fe, Co, Ni [37], MnAs [38] has higher (over room temperature) Curie temperature (T_C) than diluted magnetic semiconductor (DMS) Mn(III-V) [39]. So over room temperature magnetism is advantageous to utilize in practical spintronic device. We choose MnAs as a candidate for spin source. MnAs shows significant difference of up spin and down spin density of states at fermi-level [40] as shown in Fig. 1.6. and shows ~50% spin polarization at fermi-level [41].

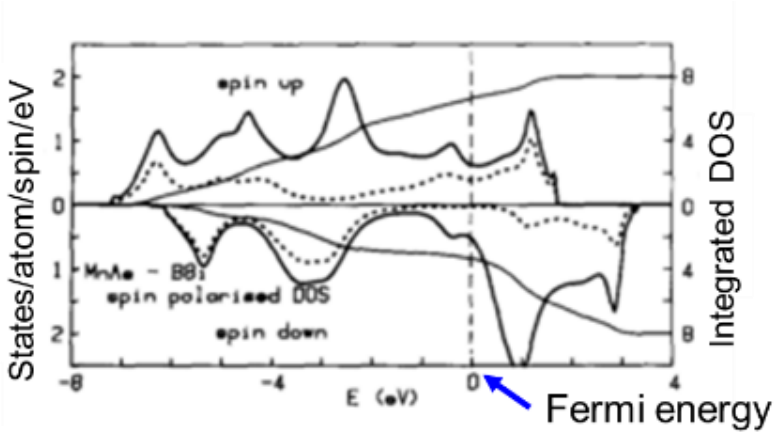

Fig. 1.6. Local density of states (dashed line: p-band, full line (p + d)-bands) for hexagonal ferromagnetic phase. (spin polarization at 0 Fermi energy.) [40]

Synthesis of transition FM metals with III-As, an unintentional mixing like Fe and As [42], Co and GaAs [43] creates magnetically dead layer (MDL) at the FM/SC interface [44] which has detrimental influences in spintronic device operation [45, 46]. Therefore, choosing MnAs epitaxial growth with III-As semiconductors in epitaxial growth, it is expected no mixing effect between MnAs and As at the interface because the MnAs also contains As which is expected as an advantageous point of MnAs epitaxial growth with III-As semiconductors. Also MnAs/III-As interface can be synthesized in the same epitaxial growth system [47] at low temperature. However, ferromagnetic Heusler-alloy shows half-metallic nature which implies

100% spin polarization are also promising candidate in spintronic device application [39]. But the main obstacle to achieve half-metallicity Heusler-alloy films are crystalline disorder , such as atomic displacement, misfit dislocation, symmetry breaking at the vicinity of the surface of the film and also there is a possibility of MDL formation. Therefore, choosing MnAs is advantageous from the material point of view. There are reports, MnAs synthesis on GaAs(001) surface MnAs shows mixed phases of hexagonal (ferromagnetic) and orthorhombic (non-magnetic) structure [48] also the c-axis laterally of the hexagonal MnAs on GaAs(001) which creates high degree of lateral magnetic anisotropy [49]. On the other hand, on GaAs(111)B surface MnAs shows controlled epitaxial (only hexagonal phase) growth of hexagonal NiAs-type structure with c-axis normal to the GaAs(111)B plane [50] and almost isotropic easy magnetization in lateral directions. It means easy to control epitaxial growth of MnAs in one direction on GaAs(111)B than that of on GaAs(001) surface. Figure 1.7 (a) and (b) shows the epitaxial relationship of hexagonal MnAs on GaAs(001) and GaAs(111)B respectively.

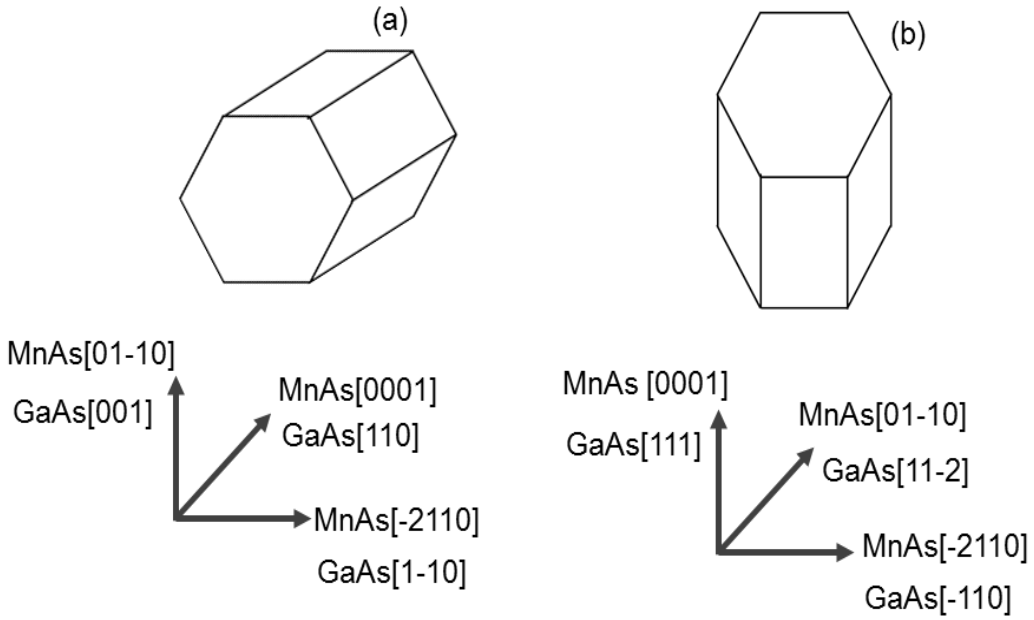

Fig. 1.7 Epitaxial relations of MnAs layers grown on (a) GaAs(001) and (b) GaAs(111)B

To this end, to evaluate spin polarized carrier injection from MnAs and detection, there are trails about spin valve measurement using MnAs/III-As(thin)/MnAs tunneling magnetoresistance (TMR) structures on GaAs(111)B where very thin layer of III-As act as a tunneling barrier not as a channel [51] with current flowing perpendicular to the GaAs(111)B substrate. There is also a report on lateral spin valve measurement with Schottky barriers contact on GaAs(001) [52] where doped III-As, GaAs act as a channel which usually has smaller SOC compared to narrow band gap. Also there is no report about spin transport properties like spin injection efficiency and spin diffusion length evaluation from MnAs into semiconductor by means of electrical study. We consider InAs a narrow gap III-As semiconductor as a channel and combination with MnAs for future spin-FET application. InAs is zinc-blende in crystal structure. It (band gap 0.35 eV at 300 K) has a surface electron accumulation layer [53] with triangular potential showing well conductive without intentional doping and large split-off energy hence higher SOC is expected which is pre-requisite to realize spin-FET operation. InAs already emerged as a promising channel material [35, 36] for spin injection and detection trials with FM. However, good 2DEG InAs epitaxial growth is important as a channel material. Comparatively, on GaAs(111)B the sliding planes with 3 sliding directions of InAs are in-plane as a result dislocation density annihilation take place on (111)B and inhibits three-dimensional growth at the interface as well, the degradation of physical properties by the dislocations become weaker by networking the dislocations than that on (001) which results in better electrical properties of InAs [54]. To our knowledge, there is a few trials of MnAs and thin-InAs combination in the form MnAs/InAs(less than 10 nm)/MnAs on GaAs(111)B [51] and MnAs/InAs(less than 10 nm)/GaAs(100) [55] but there is no trial about epitaxial growth of direct combination of MnAs and thick-InAs on GaAs(111)B. Also there is no lateral electrical and spin transport properties of MnAs/thick-InAs (channel) which are important to approach future spin-FET. Besides, the typical impedance mismatch problem

associated with MnAs/InAs hybrid structure can be improved by inserting GaAs barrier layer in between MnAs/InAs. Therefore, considering the basic properties and advantageous points of MnAs and III-As growth on GaAs(111)B substrate, we believe MnAs/III-As hybrid structures on GaAs(111)B expected to be a suitable candidate for future spin-FET. To realize spin-FET, there are three main technological challenges are, firstly, efficient injection of spin polarized charge carrier from a ferromagnetic (FM) into semiconductor (SC) channel and detection by FM, secondly, SC channel should have strong spin-orbit coupling (SOC) to precess spin during transport through SC channel, and finally, control of the spin precession by gate electric field to modulate spin signal. Therefore, to meet the technological challenging issues for spin-FET, here we report about, development of MnAs/III-As hybrid structures on GaAs(111)B by means of molecular beam epitaxy (MBE) system. We clarified structural, morphological, magnetic and basic electrical properties as well as a trial of lateral spin valve device to investigate the first technological issue about spin injection, transport and detection into the hybrid structures for spin-FET candidacy check.

Therefore, to clearly present our purpose, chapter 1 describes the background and motivation of this research including fundamental concepts of this research.

Chapter 2 describes epitaxial growth details of MnAs/III-As on GaAs(111)B, structural, morphological, basic electrical properties and magnetic properties of the as grown hybrid structure.

Chapter 3 describes fabrication process of transmission line model device (TLM) to evaluate contact properties of MnAs/III-As and also we designed and investigated spin injection and detection into a lateral spin valve device geometry of MnAs/III-As hybrid structures on GaAs(111)B.

Chapter 4 describes brief summary and future prospective of the propose hybrid structure.

References

[1]. M. N. Baibich *et al.,* Phys. Rev. Lett. **61 (**1988) 2472.

[2]. G. Binasch *et al.,* Phys. Rev. B **39** (1989) 4828.

[3]. T. Miyazaki and N. Tezuka, J. Magn. Magn. Mater. **139** (1995) 231.

[4]. J. S. Moodera *et al.,* Phys. Rev. Lett. **74** (1995) 3273.

[5]. R. C. Sousa and I. L. Prejbeanu, C. R. Physique, **6 (**2005) 1013.

[6]. S. Datta, and B. Das, Appl. Phys. Lett. **56** (1990) 665.

[7]. S. Sugahara, and M. Tanaka, Appl. Phys. Lett. **84** (2004) 2307.

[8]. K. C. Hall, and M. E. Flatté, Appl. Phys. Lett. **88** (2006) 162503.

[9]. D. Hägele *et al.,* Appl. Phys. Lett. **73** (1998) 1580.

[10]. J. K. Furdyna, J. Appl. Phys. **64** (1988) R29.

[11]. T. Dietl *et al.*, Sci. **287 (**2000) 1019.

[12]. J. Nitta *et al.,* Phys. Rev. Lett. **78** (1997) 1335.

[13]. Y. Sato *et al.,* J. Appl. Phys. **89** (2001) 8017.

[14]. K. C. Nowack *et al.,* Sci. **318** (2007) 1430.

[15]. M. Kohda *et al.,* J. Phys. Soc. Jpn. **77**, (2008) 031008.

[16]. A. Fert and H. Jaffrès, Phys. Rev. B **64** (2001) 184420.

[17]. G. Schmidt *et al.,* Phys. Rev. B **62** (2000) R4790.

[18]. J. Fabian **et al.,** Acta Physica Slovaca **57** (2007) 565.

[19]. E.I Rashba, Phys. Rev. B **62** (2000) R16267.

[20]. H. Zhu *et al.,* Phys. Rev. Lett. **87** (2001) 016601.

[21]. A. T. Hanbicki *et al.,* Appl. Phys. Lett. **80** (2002)1240.

[22]. I. Appelbaum *et al.,* Nature **447** (2007) 295.

[23]. M. Shiraishi, T Ikoma, Physica E **43** (2011) 1295.

[24]. T. Last *et al.,* J. Supercond. Nov. Magn. **18** (2005) 385.

[25]. F. J. Jedema *et al.,* Nature **410** (2001) 345.

[26]. M. Johnson and R. H. Silsbee, Phys. Rev. Lett. **55** (1985) 1970.

[27]. O.M. J. V. Erve *et al.,* Appl. Phys. Lett. **91** (2007) 212109.

[28]. Y. Ando *et al.,* Appl. Phys. Express **3** (2010) 093001.

[29]. Y. Saito *et al.,* IEEE, Trans. Magn. **48**, 2739 (2012).

[30]. T. Sasaki *et al.,* Appl. Phys. Lett. **104** (2014) 052404.

[31]. T. Yamaguchi *et al.,* Appl. Phys. Express **9** (2016) 063006.

[32]. T. Uemura *et al.,* Appl. Phys. Lett. **99** (2011) 082108.

[33]. X. Lou *et al.,* Nat. Phys. **3** (2007) 197.

[34]. P. Bruski *et al.,* Appl. Phys. Lett. **103** (2013) 052406.

[35]. K. Hamaya *et al.,* Appl. Phys. Lett. **91** (2007) 022107.

[36]. H. C. Koo *et al.,* J. Phys. D Appl. Phys. **44** (2011) 064006.

[37]. J. M. Leger *et al.,* Phys. Rev. B **6** (1972) 4251.

[38]. J. B. Goodenough and J. A. Kafalas, Phys. Rev. 157 (1967) 389.

[39]. A. Hirohata *et al.,* DOI:10.1109/TMAG.2015.2457393, IEEE Transactions on Magnetics.

[40]. M. Podloucky, J. Magn. Magn. Mater. **43** (1984) 204.

[41]. R.P. Panguluri *et al.,* Phys. Rev. B **68** (2003) R201307.

[42]. E. M. Kneedler *et al.,* Phys. Rev. B **56** (1997) 8163.

[43]. T. L. Monchesky and J. Unguris, Phys. Rev. B **74**, (2006) 241301(R).

[44]. Y.B. Xu *et al.,* Phys. Rev. B **58** (1998) 890.

[45]. G. Wastlbauer and J. A. C. Bland, Advances Physics **54** (2005) 137.

[46]. G. A. Prinz, Science New Series, **250** (1990) 1092.

[47]. M. Tanaka *et al.* Appl. Phys. Lett. **65** (1994) 1964.

[48]. M. Tanaka *et al.,* J. Appl. Phys. **76** (1994) 6278.

[49]. L. B. Steren *et al.*, Phys. Rev. B **74** (2006) 144402.

[50]. M. K*ä*stner *et al.,* Surf. Sci. **511** (2002) 323.

[51]. M. Tanaka and K. Takahashi, J. Cryst Grow. **227-228** (2001) 847.

[52]. R. Adari *et. al.*, Appl. Phys. Lett. **97**, (2010)112505.

[53]. M. Noguchi *et al.*, Phys. Rev. Lett. **66** (1991) 2243.

[54]. S.E. Hooper *et al.,* J. Cryst Grow. **127** (1993) 918.

[55]. T. W. Kim *et al.*, Appl. Phys. Lett. **88** (2006) 021915.

Chapter 2

Epitaxial growth of MnAs/III-As on GaAs(111)B and its structural, electrical and magnetic characterizations

2.1 Introduction

As discussed in Chap. 1, the importance of the propose structure but a number of questions remain unanswered including not limited:

- Epitaxial relation of MnAs/InAs on GaAs(111)B substrate
- Surface morphology
- Magnetic behavior of the structure
- Basic electric properties

This chapter details the preliminary work undertaken in attempting to answer these questions. In section 2.2, molecular beam epitaxial growth (MBE) procedure to grow MnAs/thick-InAs/GaAs(111)B hybrid structure is discussed alongside by in-situ reflection high energy electron diffraction (RHEED) images demonstrating surface reconstruction. Also ex-situ x-ray diffraction (XRD) study to elucidate crystal structure of the hybrid structure in section 2.3, atomic force microscopy (AFM) and magnetic force microscopy (MFM) to observe surface morphology in section 2.4, superconducting quantum interference device (SQUID) magnetometer to study magnetic behaviors in section 2.5, and Hall effect measurement to study basic electrical properties in section 2.6 of the as grown sample structure have been presented. A brief conclusion of this chapter has been discussed in section 2.7.

2.2. MBE growth

MBE was first succeeded with III-V semiconductors by Arthur [1] and Cho [2] at Bell Laboratories in 1960s. The method allows for the controlled growth of thin film crystalline materials on substrates composed of either the same (homoepitaxy) or different (heteroepitaxy) material. The main advantageous points of this technique the ability to control the layer thickness to the sub-monolayer level, the ability to fine tune electronic properties such as the band gap through epitaxial strain and the growth of multilayer structures. This method needs ultra-high vacuum (UHV) chambers. This is particularly important where either or both of the electronic properties and crystallographic structure are adversely affected by the incorporation of contaminants. Figure.2.1 shows a basic building block of our ultra-high vacuum MBE system. The three chambers are separated by gate valve. The main growth chamber with source cells and in-situ RHEED system is separated from load lock chamber by a buffer chamber in between to avoid direct expose of main chamber with atmosphere during loading and unloading samples. The pump systems are connected to each chamber continuously running for evacuation of the chamber.

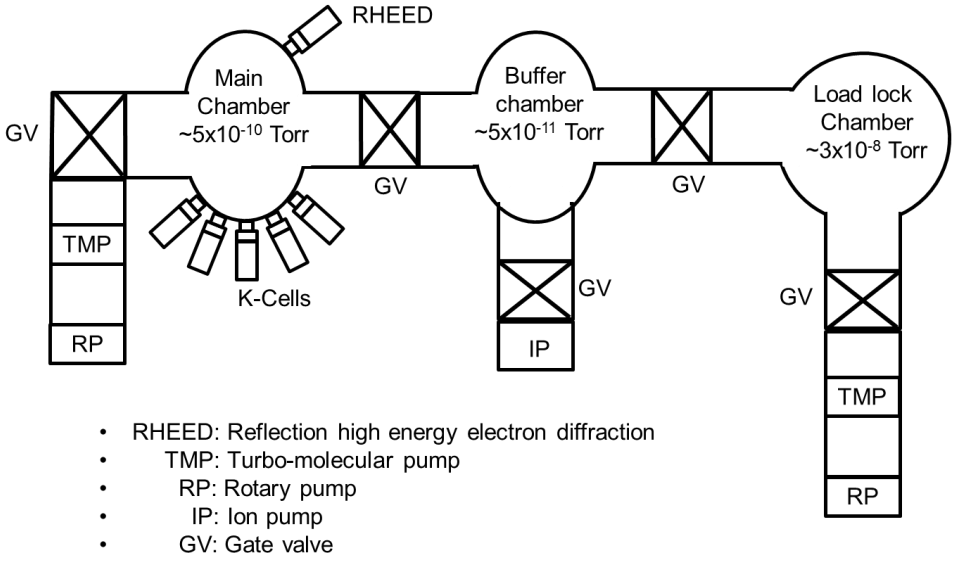

Fig.2.1 Basic building block of our ultra-high MBE system.

However, in this following section we will discuss about MBE growth condition of the hybrid structure and in-situ RHEED observation.

2.2.1 Growth and in-situ RHEED observation

MnAs/InAs and InAs/GaAs interfaces is expected to have misfit dislocations due to lattice mismatch (MnAs/InAs ~14% and InAs/GaAs ~7%). However, on GaAs(111)B the sliding planes with 3 sliding directions of MnAs and InAs are expected to be in-plane, the degradation of physical properties by the dislocations is expected to become weaker by networking the dislocations. We carried out molecular beam epitaxial (MBE) growth of MnAs(~5-200 nm)/GaAs(~0-10 nm)/thick-InAs(~200-1200 nm) /GaAs(111)B hybrid structures. First, we optimized epitaxial growth conditions of MnAs/III-As hybrid structures on GaAs(111)B. To do so, we consider, MnAs/InAs/GaAs(111)B. To carry out epitaxial growth, we choose InAs growth temperature ~480 °C which is in between typical growth temperature ~ (450-500) °C [3, 4] in MBE system. For MnAs growth, we choose two substrate temperatures one at high ~480 °C same as InAs growth temperature to get MnAs/InAs interface at same temperature, and another one is ~250 °C which is typical growth temperature ~(200-250) °C [5, 6] of MnAs. The target layer hybrid structure details is shown in Fig.2.2 (a). To carry out the growth, we used semi-insulating GaAs(111)B substrate with 12 mm X 15 mm and carried out organic cleaning in acetone 5 minutes, in methanol 5 minutes and in deionized water (DIW) 5 minutes and inorganic cleaning in semico-clean 10 minutes and in DIW 5 minutes followed by organic cleaning. Then it is loaded into a conventional solid source MBE system mounting on molybdenum block by Indium (In). After preheating of the substrate up to ~370°C in the vacuum, it is transferred into the growth chamber for growth. We grow three samples of MnAs, one at high temperature (HT) ~480 °C and two at low temperature (LT1,LT2) ~250 °C. In the

case of HT and LT1 samples, Mn cell was at ~900 °C during InAs growth. Actually, due to the result of LT1 sample, we carried out LT2 sample at Mn cell standby temperature ~450 °C during InAs growth. MBE growth conditions are shown in Fig. 2.2. (b) GaAs(111)B substrates always exposed to an excess As ambient with beam equivalent pressure (BEP) ~1.5×10^{-5} Torr. After native oxide removal at ~600 °C in 15 minutes, temperature stabilized at ~480 °C.

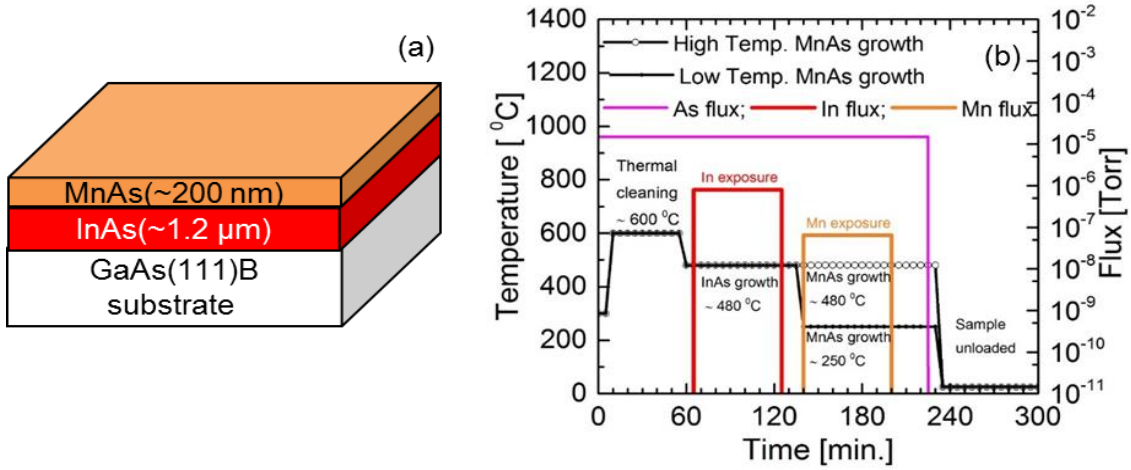

Fig.2.2 (a) Target layer hybrid structure (b) MBE growth conditions of the hybrid structures.

We used in-situ RHEED system at 15 KV and 50 µA condition to monitor surface reconstruction of the samples during growth along GaAs<-110> lateral directions. Just before starting InAs growth, we observe GaAs(111)B surface by RHEED and it shows GaAs(111)B-(2x2) as shown in Fig.2.3 (a) surface along GaAs<-110> directions. At substrate stabilized temperature at ~480 °C thick InAs growth of 1.2 µm (In BEP ~8.0×10^{-7} Torr) were carried out in 1 hour with different Mn cell temperatures. The RHEED patterns show InAs(111)-(2x2) as shown in Fig.2.3 (b) streaky patterns for the all samples which is similar to InAs on GaAs(111)A [7], with time, the RHEED streak distance shrinkage laterally by keeping (2x2) streaky pattern which implies lattice transition from GaAs to InAs. When InAs growths were finished, again substrate temperature were stabilized for MnAs growths and MnAs growths

were carried out in 1 hour (Mn BEP ~6.4×10^{-8} Torr) for HT, LT1, and LT2 samples. HT growth of MnAs vanishes the As-terminated (2x2) surface with time no periodic pattern as shown in Fig.2.3 (c). But in the case, LT1 and LT2 samples shows MnAs(0001)-(2x2) surface and we observe, with time, the RHEED streak distance increases laterally by keeping (2x2) as shown in Fig.2.3 (d) streaky pattern which implies lattice transition from InAs(111) to MnAs(0001) surface similar to MnAs(0001) directly grown on GaAs(111)B surface [8-10]. The streaky patterns at LT1 and LT2 samples suggest layer by layer (two dimensional) epitaxial growth of MnAs and InAs on GaAs(111)B. This is also known as Frank-van der Merwe growth mode. On the other hand, the disappearance of RHEED streak indicates the growth layer might be coalescence [11] (induced by lattice mismatch between two layers) into InAs layer which may result in poly-crystalline growth. This type of growth related to three-dimensional growth known as Volmer-Webber mode.

Therefore, the low temperature MnAs growth suggests good layer by layer epitaxial growth of the hybrid structure. From now, we concentrate on low temperature MnAs growth condition for the rest of the samples in the work.

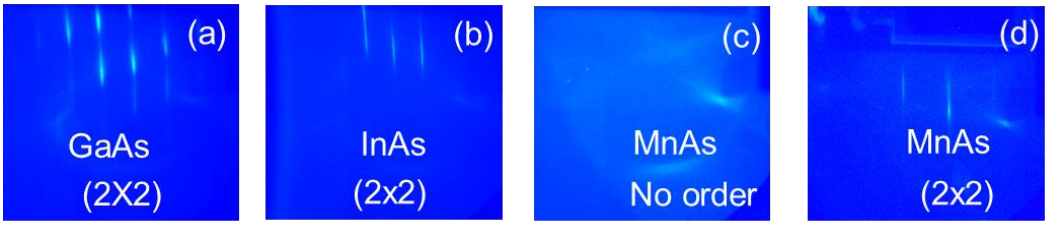

Fig.2.3 RHEED observation images of MnAs(200 nm)/InAs(1.2 μm)/GaAs(111)B hybrid structures.

Now, we plan to grow MnAs/GaAs/InAs/GaAs(111)B hybrid structure at low temperature MnAs growth. The GaAs growth temperature has been kept to ~480°C to grow epitaxial growth rather than high temperature growth [12]. The reason is to keep InAs layer insensitive to temperature during GaAs growth. The details of MnAs/GaAs/InAs/GaAs(111)B hybrid

structure is shown in Fig.2.4 (a). Figure.2.4 (b) shows details of MBE growth conditions. The growth rate of GaAs was 3.6 nm/min.

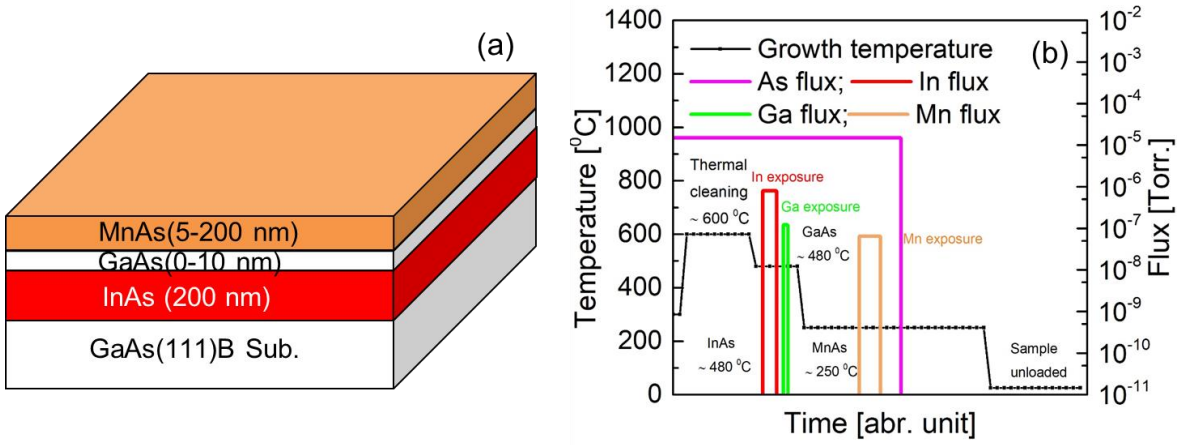

Fig.2.4 (a) Target layer hybrid structure (b) MBE growth conditions of the hybrid structures.

The RHEED observation of InAs and MnAs shows similar surface periodicity as already earlier at low temperature MnAs case. Here, we closely monitor the growth behavior of GaAs insertion. The growth rate of GaAs was 3.3 nm/min. In RHEED observation along <-110> directions, for 1 and 3 and 10 nm GaAs barrier, we see 1 and 3 nm show no changing of lateral lattice distance. We only see that 10 nm GaAs barrier shows changing of lateral lattice distance (*d*) as shown in Fig.2.5. Thus it seems InAs surface changes to GaAs in the case of 10 nm GaAs barrier.

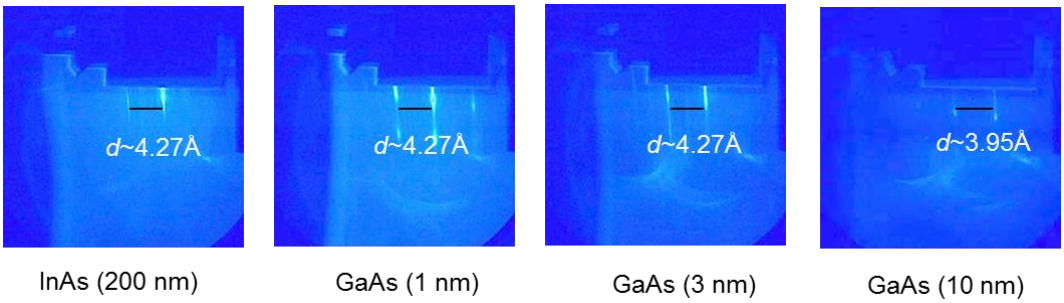

Fig.2.5 In situ RHEED pattern for different barrier thickness GaAs on InAs.

We also carried out time evaluation of RHEED images to see lattice transition of InAs and GaAs shown in Fig.2.6 (a) and (b) respectively. We see double step lattice transition ~4 nm of InAs from GaAs surface and abrupt lattice transition of GaAs ~3.6 nm from InAs lattice respectively. The origin of these transition is still unclear for such lattice mismatch growth. The diffraction from <-110> directions and considering strain relaxed InAs layer the extracted lattice parameter of GaAs is close to bulk value (~5.65 Å). However, MnAs lattice transition estimation was difficult to be evaluated due to surface change during reduction of growth temperature as shown in Fig.2.2 (b).

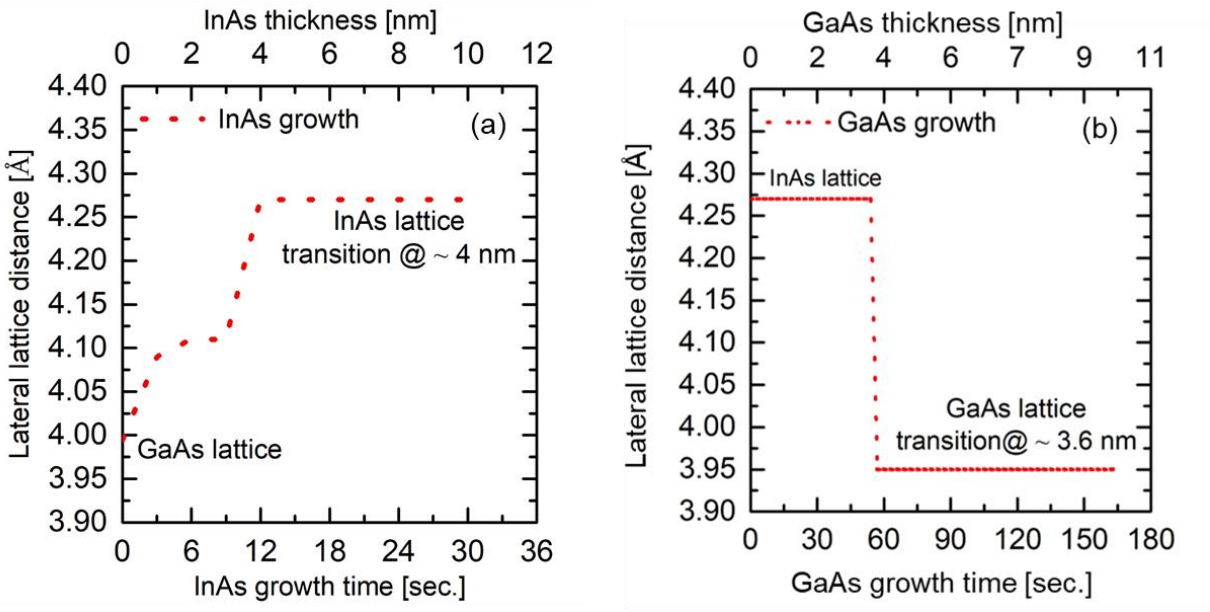

Fig.2.6 Growth time versus lateral distance (*d*) curves for (a) InAs (b) GaAs.

2.3 Epitaxial relations

In order to clarify the crystal structures and their relations. We carried out XRD measurement by X'Pert PANalytical diffractometer at room temperature for HT, LT1 and LT2 samples. The basic principle of XRD measurement has been discussed in appendix-A2. The incident x-ray beam wavelength was 1.540598 Å. Figure 2.7 shows the 2θ scanning result between 20° and

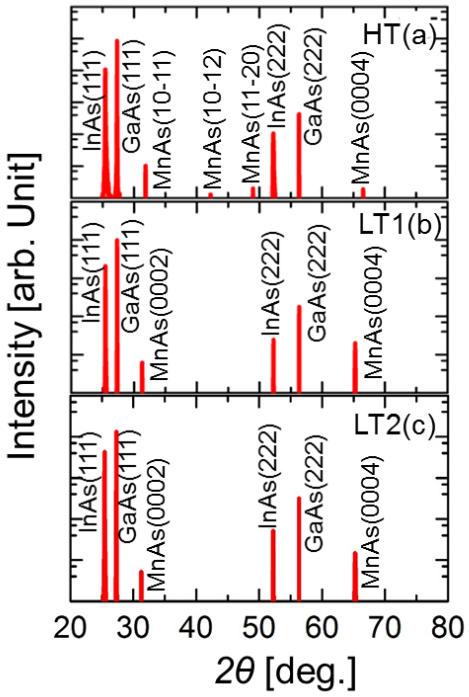

Table 2.1 Extracted lattice parameters

samples	GaAs	InAs	MnAs
	a [Å]	a [Å]	c [Å]
HT	5.65	6.06	5.69
LT1, LT2			5.71

Fig. 2.7. XRD spectra of MnAs/InAs/GaAs(111)B obtained by 2θ-scanning for (a) HT, (b) LT1 and (c) LT2 samples.

80°. For HT sample, in Fig. 2.4 (a), we see strong peaks of zinc-blende GaAs(111) and (222) at ~27.31° and ~56.36°, and InAs(111) and (222) at ~25.44° and ~52.24°. We also see weak peaks at ~31.87°, ~42.23°, ~49.00°, and ~65.56°. According to the powder diffraction data of hexagonal MnAs [13], these indicate hexagonal MnAs (10-11), (10-12), (11-20) and (0004) respectively. The results suggest poor alignment of hexagonal MnAs layer with zinc-blende InAs and GaAs. It seems poly-crystalline growth of MnAs at HT sample. For LT1 and LT2

samples, in Fig. 2.4 (b) and (c), we see zinc-blende GaAs(111) and (222), and InAs(111) and (222) similar to the HT sample. We also see relatively strong peaks at ~31.29° and ~65.26°, which are hexagonal MnAs(0002) and (0004) respectively. In LT1 and LT2 samples, peaks from hexagonal MnAs(0002) and (0004) and no additional peaks observed that means single crystalline epitaxial growth of MnAs which are similar to MnAs directly grown on GaAs(111)B [14]. From the 2θ data, of GaAs(111), InAs(111), MnAs(0004) the extracted lattice parameter GaAs, InAs and MnAs for HT, LT1 and LT2 samples has been summarized in table 2.1. From the table, we see the extracted lattice parameter for hexagonal MnAs of c ~ 5.69 Å for HT sample having little angle shift (0.3 deg.) of (0004) which is differ from LT1, LT2 samples lattice parameter c ~ 5.71 Å a similar value to bulk case[15]. The poly-crystalline growth mixing of different plane results strained c-axis of hexagonal MnAs result in not relaxed. The angle shift of HT MnAs(0004) implies tensile strain exist in the film result in no relaxation layer. Also we see lattice parameters for cubic InAs and GaAs of a ~ 6.06 Å and a ~ 5.65 Å, respectively for HT, LT1 and LT2 samples. The LT1 and LT2 samples' lattice parameters are consistent with their bulk values [15, 16] which imply that the grown epitaxial layers are strain relaxed and lattice mismatch. The LT1 and LT2 samples results suggest good alignment of hexagonal MnAs on zinc-blende InAs and GaAs(111)B and no coexisting of hexagonal (0002) and orthorhombic plane in 2theta measurement. Therefore, we mainly concentrated on low temperature grown MnAs samples. However, the GaAs grown layer on InAs/GaAs(111)B is possibility of broadening GaAs peaks through lattice relaxation because of underneath InAs layer having larger lattice constant (a ~ 6.05 Å) than that of GaAs (a~5.65 Å). To clarify any effect of GaAs barrier on GaAs substrate peak. We carried out simulation in Omega/2theta scanning. It seems the 10 nm relaxed GaAs(111)B makes the GaAs peak broadening as shown in Fig. 2.8. But in XRD study, InAs and MnAs and GaAs grown layers shows similar peak positions with GaAs insertion samples as shown in Fig.2.9. The GaAs insertion effect seems not apparent in the present study. Larger GaAs thickness dependent study are necessary.

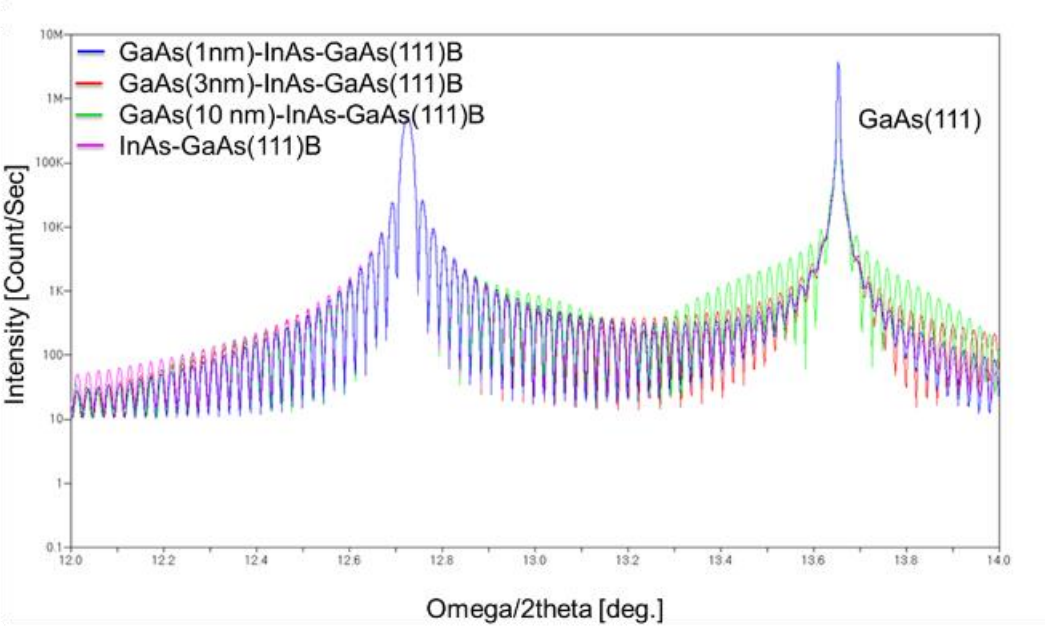

Fig.2.8 Simulation of GaAs effect on GaAs substrate peaks.

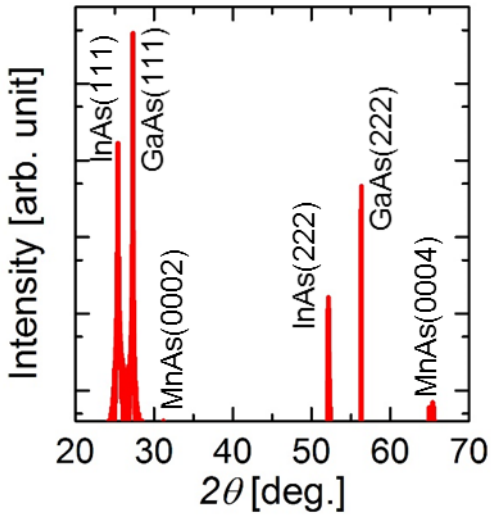

Fig. 2.9 XRD spectra of MnAs/GaAs/InAs/GaAs(111)B obtained by 2θ-scanning.

We carried out ω scanning of InAs(111) and MnAs(0002) to elucidate the deviation of c-axis normal to the planes as shown in Fig.2.10 (a) and (b). Peak positions are almost zero, i.e. the ω values at the peaks are almost same as the θ values in 2θ scanning. The result indicates almost no tilting of both InAs and MnAs layers to GaAs substrate. From the peak broadening

of InAs(111) and MnAs(0002), we estimated the threading dislocation densities using the following expression;

$$(\Delta\beta)^2 = K_0 D \quad (2.1)$$

Where, $\Delta\beta$ is the full-width at half maximum at $\beta\,(\omega - \theta)$ plotting, D is the threading dislocation density and K_0 is a constant that can be find theoretically [17] and experimentally [18]. K_o can be theoretically estimated by the following expression;

$$K_0 = 2\pi \ln 2 (b)^2 \quad (2.2)$$

Where, b is the length of Burgers vector and the estimated smallest threading dislocation density are ~5.5×10^8 and ~2.5×10^9 cm^{-2} for InAs (1200 nm) and MnAs (200 nm), respectively as shown in Fig. 2.10 (c). The value for InAs seems relatively smaller than that on (001) assuming same thickness [18]. Hence, from 2θ and ω scanning results, we can conclude good stacking of MnAs(0001)/InAs(111)B on GaAs(111)B with less dislocation density at thicker InAs and MnAs grown layer cases. MnAs tendency seems little bit higher slope due different InAs thickness layer underneath it.

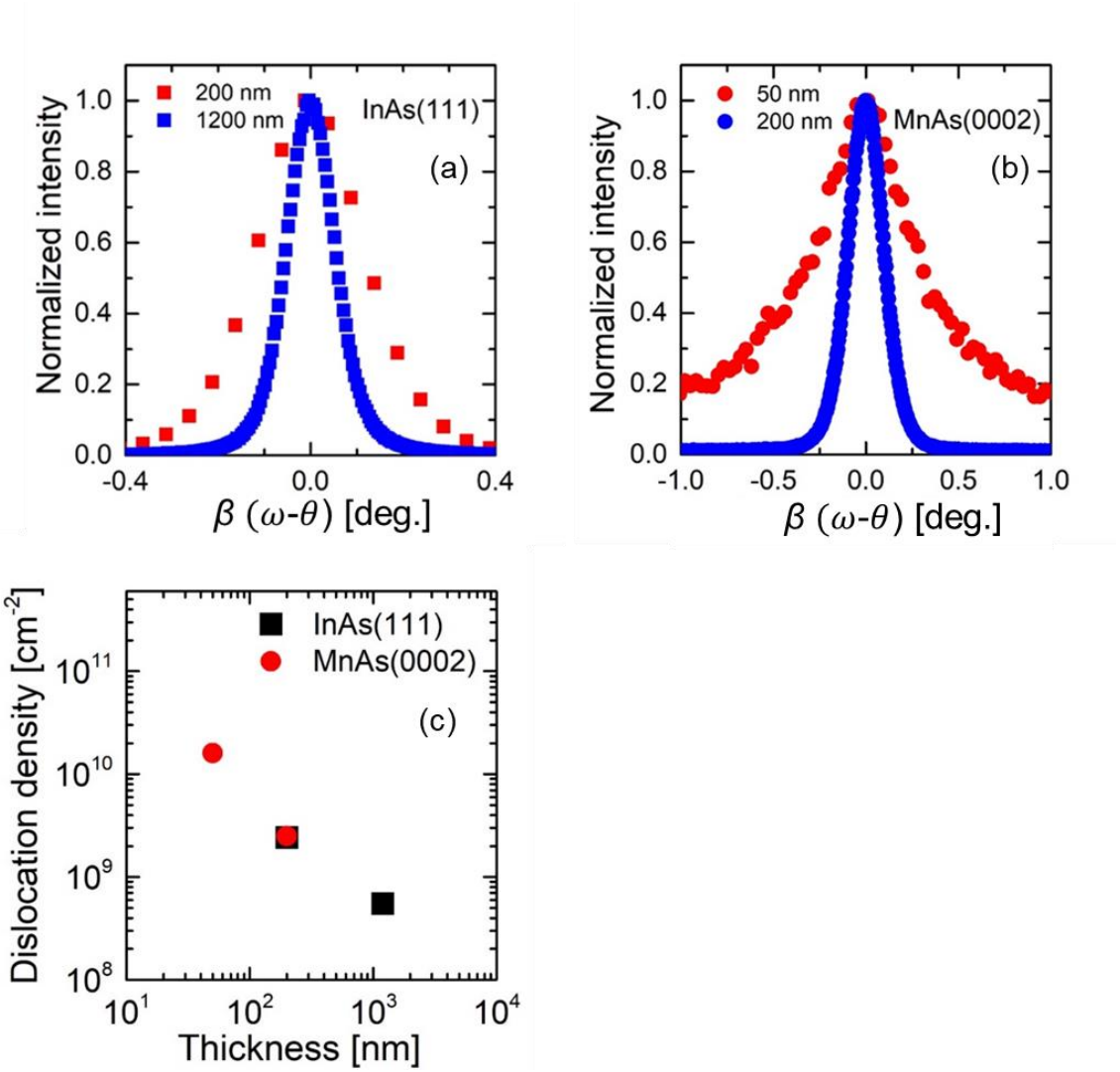

Fig. 2.10 $\beta(\omega\text{-}\theta)$ scanning curves of (a) InAs(111) and (b) MnAs(0002) (c) Thickness dependence threading dislocation density of InAs(111) and MnAs(0002).

For LT1 sample, we also performed lateral φ scanning for MnAs(10-12), InAs(004), and GaAs(004) planes as shown in Fig.2.11 (a). The incident X-ray direction at φ = 0° was along [-211] of GaAs(111)B. We confirmed 6-fold rotational symmetry of MnAs, and 3-fold rotational symmetry of InAs and GaAs. The results indicate that MnAs[-2110], InAs[-110], and GaAs[-110] are parallel each other. We can clearly see the relations among hexagonal MnAs and pseudo-hexagonal GaAs and InAs as shown in Fig.2.11 (b). This result shows good alignment of hexagonal MnAs and cubic InAs epitaxial layers with cubic GaAs substrate. In addition, LT2 sample shows similar result to LT1.

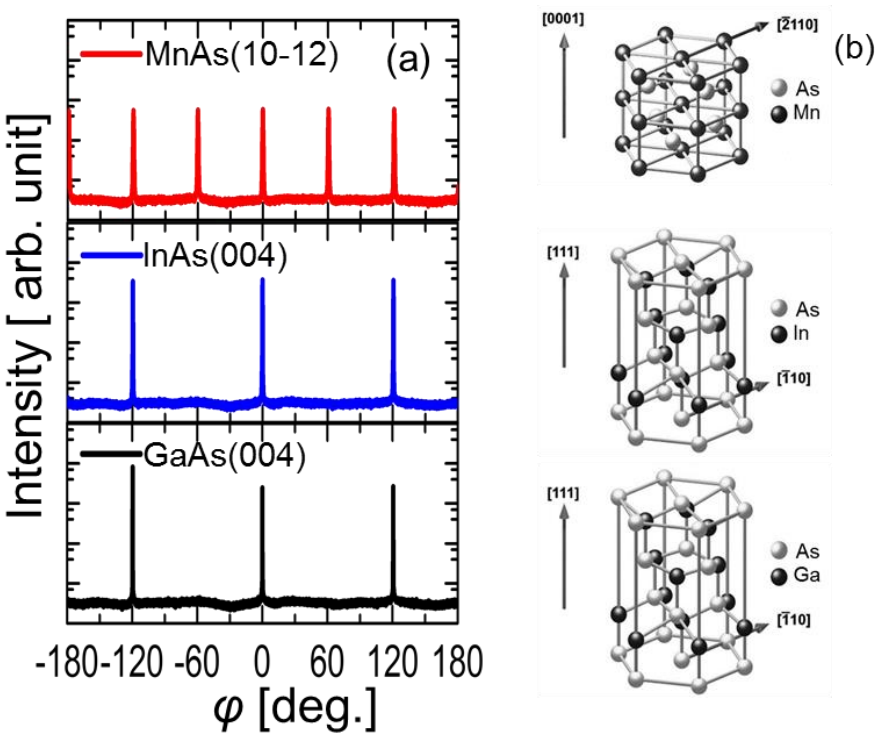

Fig.2.11 (a) Lateral φ-scanning for MnAs(10-12), InAs(004), and GaAs(004) planes for LT1 sample (b) Crystal structures and epitaxial relation between the hexagonal MnAs and pseudo-hexagonal GaAs and InAs [10].

2.4 Surface morphology of MnAs

We used Nanoscope IIIa tool that perform atomic force microscopy (AFM) and magnetic force microscopy (MFM) to study surface morphology and magnetic structure of the HT, LT1 and LT2 samples. We proceeded magnetization perpendicular to the sample surface of magnetic etched silicon cantilever (MESP) coated with Co/Cr having hard moment (HM) before the measurements. We measured MFM at the same position of the samples followed by AFM measurement. The scan size was 4 μm X 4 μm. HT sample shows large surface root mean square (RMS) ~104.6 nm in the AFM image Fig.2.12 (a) and the MFM image Fig.2.12 (d) seems includes much morphological contribution, however, we can see some differences between AFM and MFM. Therefore, we think that there is a ferromagnetic structure on the surface. In Figs 2.12 (b) and (e), LT1 sample shows very smooth surface RMS ~1.1 nm in the AFM image and maze-like magnetic structure in the MFM image respectively, which indicates the MnAs layer is ferromagnetic. In Fig. 2.12 (c) and (f), LT2 sample shows also smooth surface RMS ~0.8 nm and contrast maze like magnetic structure in MFM image respectively which is similar to LT1 sample behavior. In MFM measurement, the RMS information is excluded. Magnetic cantilever tip is sensitive to out-of-plane components of MnAs stray field. The interaction between tip and the stray field depends on the relative orientation of cantilever tip and stray field directions (up or down). To clarify the complex maze like magnetic structure contrast, assume a ferromagnetic stripe is divided into oppositely oriented bar magnets along width of the ferromagnetic stripe. The stripe has easy magnetization along the width of the stripe. The magnetic stray field of the bar magnet-like domains will either point up or point down, as shown by arrows in Fig.2.12 (g). Parallel and antiparallel magnetization directions of tip and stray field creates an attractive and repulsive interaction which results in bright and dark contrast respectively in imaging.

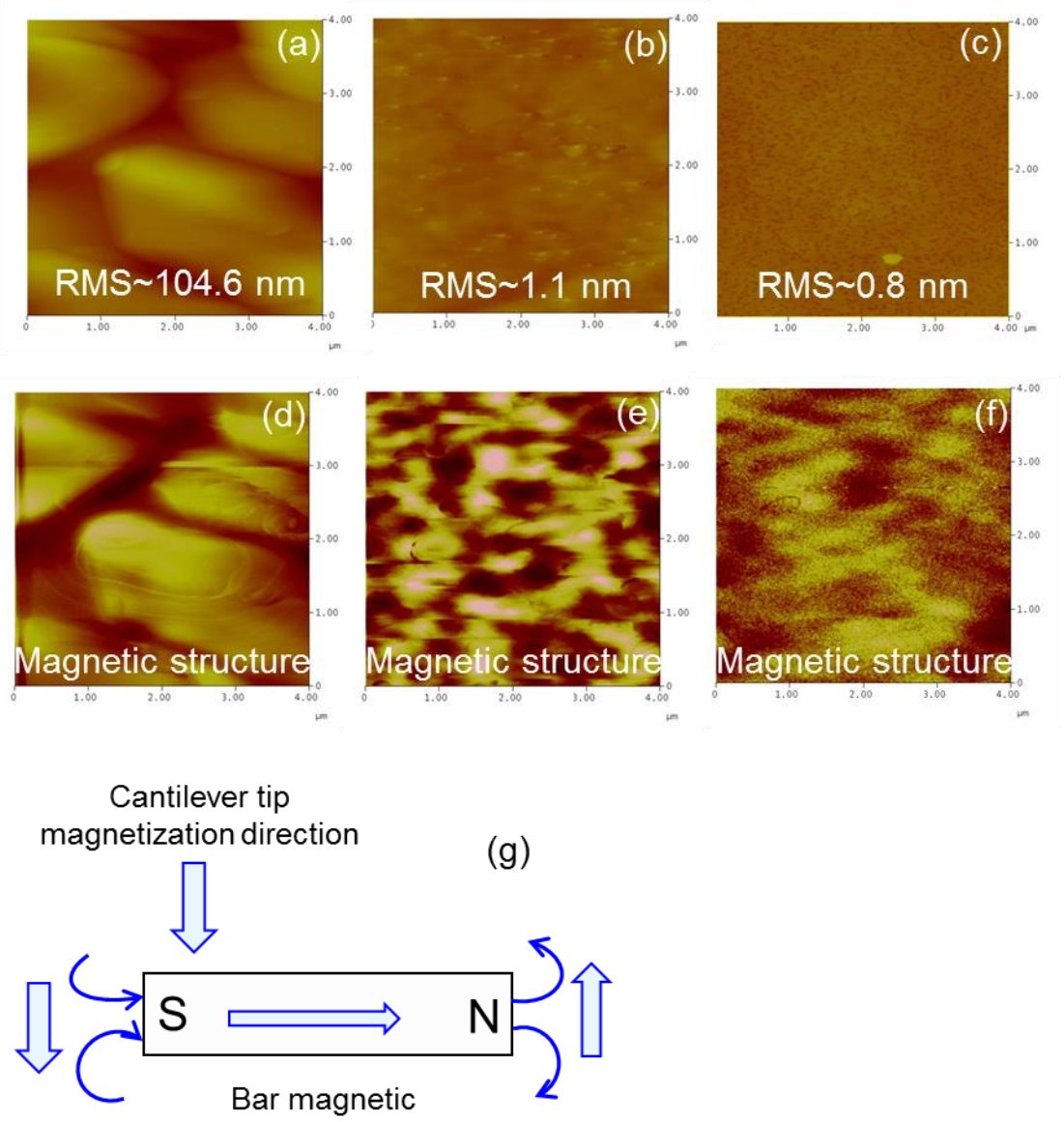

Fig.2.12. AFM and MFM images: (a) and (d) for HT, (b) and (e) for LT1, and (c) and (f) for LT2 samples respectively. (g). Cantilever and out-of-plane stray magnetic field interaction mechanism in MFM images.

2.5 Basic electrical properties

It is important to know basic electrical properties of like sheet (thin film) resistance (ρ_s), mobility (μ), sheet carrier density (n_s) and carrier type of the grown samples before proceed to spintronic device application. We perform Hall effect measurement by van der Pauw technique [19] at room temperature. We prepared 5 mm x 5 mm size sample. We see, in HT sample, ρ_s ~369.5 Ω/sq. which is much higher than that of LT1 sample (ρ_s ~6.3 Ω/sq.). The large ρ_s in HT sample is seems reasonable due to large surface roughness as discussed in section 2.4. We found p-type conduction of all samples. We also measured one bare InAs(~1.2 μm)/GaAs(111)B as reference sample to evaluate in details. Interestingly, p-type conduction of HT, LT samples seems hided the n-type conduction of bare InAs(~1.2 μm)/GaAs(111)B by higher sheet carrier concentration MnAs. The details of Hall measurement are show in table 2.2.

Table 2.2 A summary of Hall effect measurement data

Sample	ρ_s [Ω/sq.]	μ [cm^2/V-s]	n_s[cm^{-2}]	Mn cell status @InAs growth	Conduction type
InAs/GaAs(111)B	219.0	10150	2.5×10^{12}	300 °C	n
HT	369.5	91	1.8×10^{14}	900 °C	p
LT1	6.3	35	2.8×10^{16}	900 °C	
LT1-MnAs etched	553	4145	2.7×10^{12}		n

The complete etched out MnAs in LT1, shows InAs sheet ρ_s increase and μ decrease which explains effect of Mn cell status on InAs layer. It seems possibility of Mn into n-type InAs layer which can act as donor results in decreasing mobility. Therefore, we only concentrate on LT2 growth condition seems better for epitaxial growth.

2.6 Magnetic behaviors

To confirm detail magnetic properties of the hybrid structure, we performed magnetization (M) measurements of low temperature MnAs growth sample using magnetic property measurement system (MPMS), which is a superconducting quantum interference device (SQUID). The magnetization of up to 10^{-6} emu can be measured even under high magnetic field environment. We prepared (5x4) mm^2 sample for the measurement. Figure 2.13 (a) and (b) shows the normalized magnetization of the hybrid structure at 300 K as a function of applied magnetic field (H) along two lateral [-2110], [01-10] and out-of-plane [0001] directions of hexagonal MnAs. We found easy magnetization along lateral directions is isotropic and hard magnetization along out-of-plane. This behaviors are similar to MnAs directly on GaAs(111)B [20]. The saturation magnetizations (M_s) are ~430 emu/cm^3 and ~200 emu/cm^3 and the coercive fields (H_c) are ~200 Oe and ~600 Oe along lateral and out-of-plane, respectively which implies strong anisotropy between lateral and out of plane. Here, we have not subtracted the influence of diamagnetic influence of GaAs and InAs into the magnetization. In the case of lateral measurement, the magnetic moment of MnAs after the saturation is ~100 times larger than that of diamagnetic GaAs and InAs at 2000 Oe. Therefore, the diamagnetic contribution is almost negligible. However, in the case of out-of-plane measurement, the diamagnetic moment becomes ~15 times larger at 30000 Oe. Therefore, it can give significant contribution into the total magnetic moment and the difference of saturation magnetization between lateral and out-of-plane measurements. Since there are also magneto-crystalline anisotropy and demagnetizing field anisotropy, these can give the difference of coercive field between lateral and out-of-plane measurements. For thin films the demagnetizing factor can be calculated using ellipsoidal model [21]. In our sample, the thickness of MnAs(200 nm) is much smaller than its length (5 mm) and width (4 mm). We assume flat sample and using the model [21], we roughly calculated the demagnetizing factors along lateral directions 0 and along out-of-plane 4π. It

seems, the large demagnetizing factor along out-of-plane contributes largely to demagnetizing field (~1200 Oe at saturation magnetization) which affect the magnetization along out-of-plane. This results in different magnetic response between lateral and out-of-plane magnetizations. However, the lateral isotropic easy magnetization behavior expected to flexible for magnetic direction which can be helpful to design lateral spintronic device.

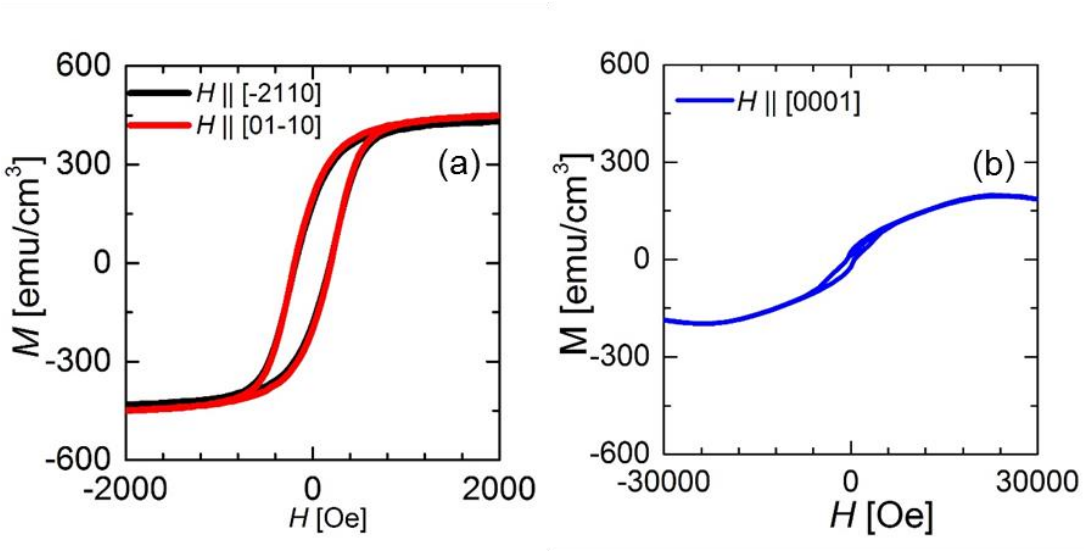

Fig.2.13 (a) Magnetization curves at 300 K along (a) lateral [-2110], and [01-10] (b) out-of-plane [0001] directions of hexagonal MnAs.

To study in details, we investigated about lateral magnetization behaviors at varying MnAs thickness. Figure 2.14 (a) shows the magnetization behaviors of 5, 50 and 200 nm MnAs-thickness samples. The 5 nm sample shows gradual magnetization switching. It might happen if the film thickness become discontinuous. The 50 and 200 nm samples show step magnetization which may be due to continuous film thickness. We also extracted H_c field of the three different MnAs-thickness samples as shown in Fig.2.14 (b). The reduction of H_c with increasing magnetization with MnAs thickness increasing may affected by the different dislocation density and other structurally related phenomena that affect the nucleation and

movement of magnetic domains [22]. The 200 nm MnAs-thickness sample seems better in-terms of low H_c to device application. We investigate in more details of 200 nm MnAs sample. We carried out lateral angle dependence magnetization at 2000 Oe as shown in Fig.2.15 (a) which reveals similar magnetization at 2000 Oe (Fig. 2.13 (a)) at different lateral angles. This implies complete lateral easy isotropic magnetic behaviors.

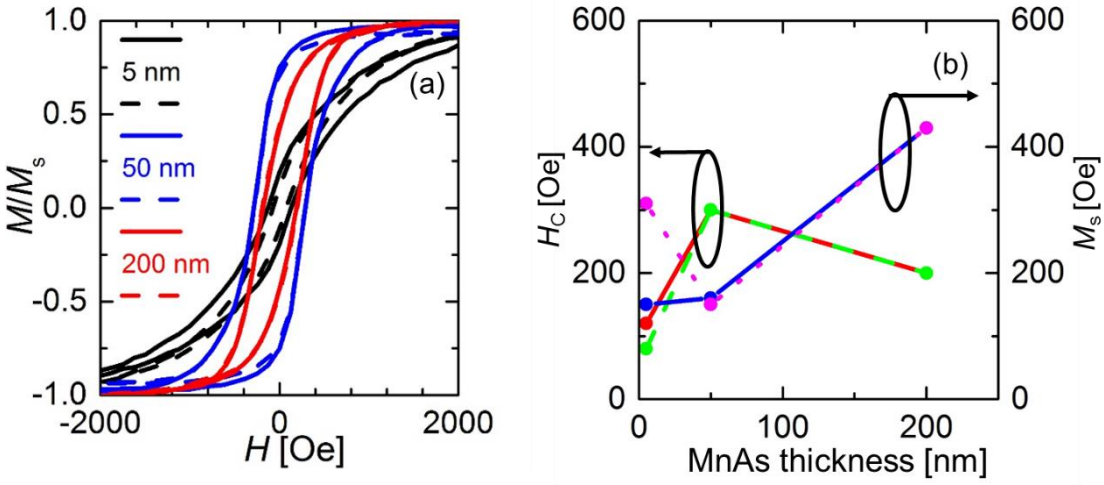

Fig.2.14 (a) Magnetization curves at 300 K along lateral [-2110] (solid line), [01-10] (broken line) directions of (a) of 5, 50 and 200 nm MnAs-thickness. (b) MnAs-thickness versus coercive field and magnetization curve.

We also studied magnetic phase transition temperature (T_c) of MnAs as a function of temperature at magnetic field of 2000 Oe along [-2110] and [01-10] lateral directions. From

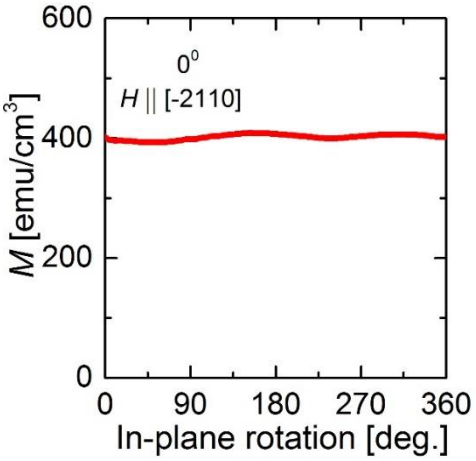

Fig.2.15 Magnetization curves with lateral rotation angle.

Fig.2.16 (a), we see the sample shows second order phase transition character from ferromagnetic to paramagnetic (FM-PM) transition is similar along both lateral directions. In the temperature range between 4 K and 200 K, it seems almost no change of spontaneous magnetization. Above 200 K the sample shows significant decrease of the magnetization with increase of temperature. We also extracted T_c value by first derivative of magnetization versus temperature curve [23] as shown in Fig.2.16 (b). The minimum gives the T_c ~324 K which is slightly higher than bulk valve of 313 K. The result might originate from some differences between thin film and bulk [24].

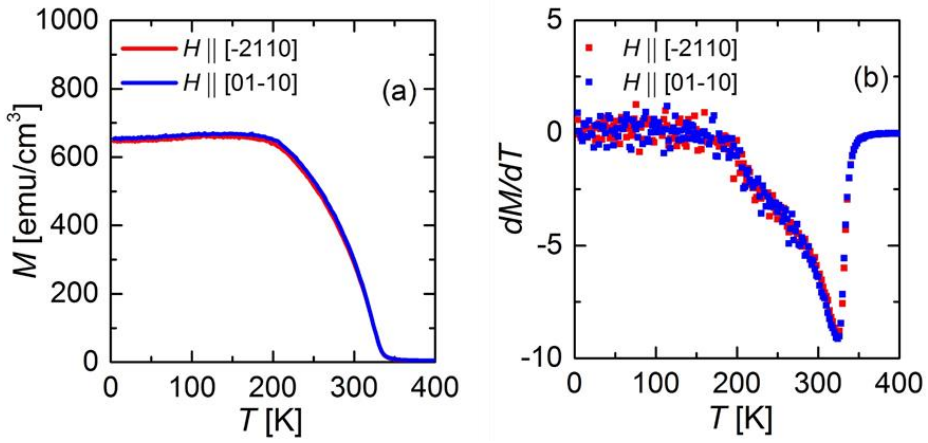

Fig.2.16 (a) Magnetization versus temperature curve and (b) its first derivative.

2.7. Conclusion

We carried out successful molecular beam epitaxial (MBE) growth of MnAs(~5-200 nm)/GaAs(~0-10 nm)/thick-InAs(~200-1200 nm) /GaAs(111)B hybrid structures at low temperature MnAs epitaxial growth. We see double step lattice transition ~4 nm of InAs from GaAs surface and abrupt lattice transition of GaAs ~3.6 nm from InAs lattice respectively in RHEED study. The origin of these transition is still unclear for such lattice mismatch growth. In 2θ x-ray diffraction (XRD) measurement, we see single phase epitaxial growth of hexagonal MnAs with cubic InAs and GaAs. Also, the extracted lattice parameters are consistent with their bulk values which imply that the grown epitaxial layers are strain relaxed. To check deviation of c-axis, we carried out ω scanning. From ω and 2θ measurement, we also observed less deviation (InAs ~0.12° and MnAs~0.22°) of c-axis normal to the planes of MnAs(200 nm) and InAs(1200 nm). The 2θ and ω scanning indicates good epitaxial growth of MnAs(0001)/InAs(111)B/GaAs(111)B. We see reduction of estimated thickness dependence threading dislocation density from the ω-θ broadening with increasing grown layer thickness following pair annihilation mechanism. It means better crystal quality in thicker case.

The low temperature grown MnAs sample shows better basic electrical properties than HT sample. The p-type conduction of MnAs hided the n-type conduction of underneath InAs layer. Besides, we also confirmed smooth surface and maze-like magnetic structures on the low-temperature grown samples by AFM and MFM measurements. By SQUID magnetometry measurement, the MnAs/III-As/GaAs(111)B grown sample shows strong magnetic anisotropy along [-2110] and [0-110] lateral and [0001] out of plane directions. It shows easy and isotropic magnetization in lateral directions. The MnAs isotropic behavior almost similar to MnAs directly on GaAs(111)B. We see higher MnAs thickness higher saturation magnetization in lateral directions which seems related to crystal quality. In lateral directions, it shows over

room temperature magnetism (estimated Curie temperature ~320-324 K). Over room temperature T_c value and isotropic magnetic behaviors in lateral directions gives a good choice of MnAs for lateral spintronic device design on GaAs(111)B. Therefore, we believe that the MnAs/InAs/GaAs(111)B can be a base structure for future spin-FETs.

References

[1]. J. Arthur, J. Appl. Phys. **39** (1968) 4032.

[2]. A. Y. Cho, J. Appl. Phys. **41** (1970) 2780.

[3]. S.E. Hooper *et al.,* J. Cryst Grow. **127** (1993) 918.

[4]. H. Yamaguchi *et al.,* Appl. Phys. Lett. **69** (1996) 776.

[5]. M. Tanaka *et al.,* Appl. Phys. Lett. **65** (1994) 1964

[6]. M. Tanaka *et al.,* J. Appl. Phys. **76** (1994) 6278.

[7]. H. Yamaguchi *et al.,* Phys. Rev. B **55** (1997) 1337.

[8]. M. Tanaka *et al.* J., Magn. Magn. Mater. **198** (1999) 719.

[9]. J. Sadowski *et al.,* Appl. Surf. Sci. **166** (2000) 247.

[10]. M. Kastner *et al.,* Surf. Sci. **511** (2002) 323.

[11]. J. B. Park *et al.,* J. Crys. Growth **273** (2005) 396.

[12]. N. Chad, J. Cryst. Growth **97** (1989) 415.

[13]. S. Haneda *et al.,* J. Phys. Soc. Jpn. **42** (1977) 1201.

[14]. Y. Morishita *et al.,* Jpn. J. Appl. Phys. **36** (1997) L1100.

[15]. M. Tanaka and K. Takahashi, J. Cryst. Growth **227-228** (2001) 847.

[16]. I. Vurgaftman *et al.,* J. Appl. Phys. **89** (2001) 5815.

[17]. J.E. Ayers, J. Crystal Growth **135** (1994) 71.

[18]. Y. Jeong *et al.,* J. Crystal Growth **301-302** (2007) 235.

[19]. L. J. van der Pauw, Philips Tech. Rev. **20** (1958) 220.

[20]. L. B. Steren *et al.,* Phys. Rev. B **74** (2006) 144402.

[21]. J.A. Osborn, Phys. Rev. **67** (1945) 351.

[22]. M. Tanaka *et al.,* J. Appl. Phys. **76** (1994) 6278.

[23]. J. Varalda *et al.,* J. Appl. Phys. **100** (2006) 093524.

[24]. N. Mattoso *et al.,* Phys. Rev. B **70** (2004) 115324.

Chapter 3

Device processing and electrical characterization of MnAs/III-As/GaAs(111)B

3.1 Introduction

It is important to know contact information between ferromagnetic (FM)-MnAs and III-As semiconductor (SC) on GaAs(111)B. As MnAs is metal, no band gap exist between valence band and conduction band. However, usually metal and semiconductor contact nature depends on work function of metal and semiconductor. If metal work function ($q\emptyset_m$) differ to semiconductor work function ($q\emptyset_s$) band bending take place into semiconductor which results in rectifying or Ohmic contact depending on the semiconductor conduction type [1]. The amount of band bending is given by the difference of work functions of metal and semiconductor. This can be expressed in terms of barrier height $q\emptyset_b$ as follows;

$$q\emptyset_b = q\emptyset_m - q\emptyset_s \quad (3.1)$$

To this end, for, MnAs/InAs contact, we assume no contribution of surface dipole to the work functions of metal and semiconductor. We roughly estimated MnAs work function as ~4.21 eV from MnAs/Si interface [2] using 0.16 eV barrier height (between MnAs/Si) and Si electron affinity 4.05 eV by neglecting (E_c-E_F) of n-doped (~4.4x10^{15} cm^{-3}) Si as shown in Fig. 3.1(a). Since, InAs fermi level just over the conduction band then neglecting the (E_c-E_F) of InAs, we assume InAs work function similar to InAs electron affinity ~4.90 eV [3] at room temperature which is higher than MnAs work function. According to equation (3.1) the negative barrier height (~ -0.69 eV) between MnAs/InAs contact and fermi level pinning over conduction band edge of InAs [4] expected to show barrier free Ohmic contact. The estimated carrier

concentration at the band bending of two dimensional electron gas of (2DEG) InAs is ~7x10^{16} m^{-2}. Using the estimated carrier concentration, we also estimated electric field ~7.9x10^{7} V/m. Hence, we estimated bending distance position at constant electric field from the interface which is around ~9 nm. The estimated contact profile of MnAs/InAs and MnAs/GaAs/InAs can be represent in terms of energy band diagram with GaAs affinity (χ) as shown in Fig.3.1(b) and Fig.3.2 in details. Here, E_C , E_V and E_F are energy level of conduction band minimum, valance band maximum and fermi-level respectively.

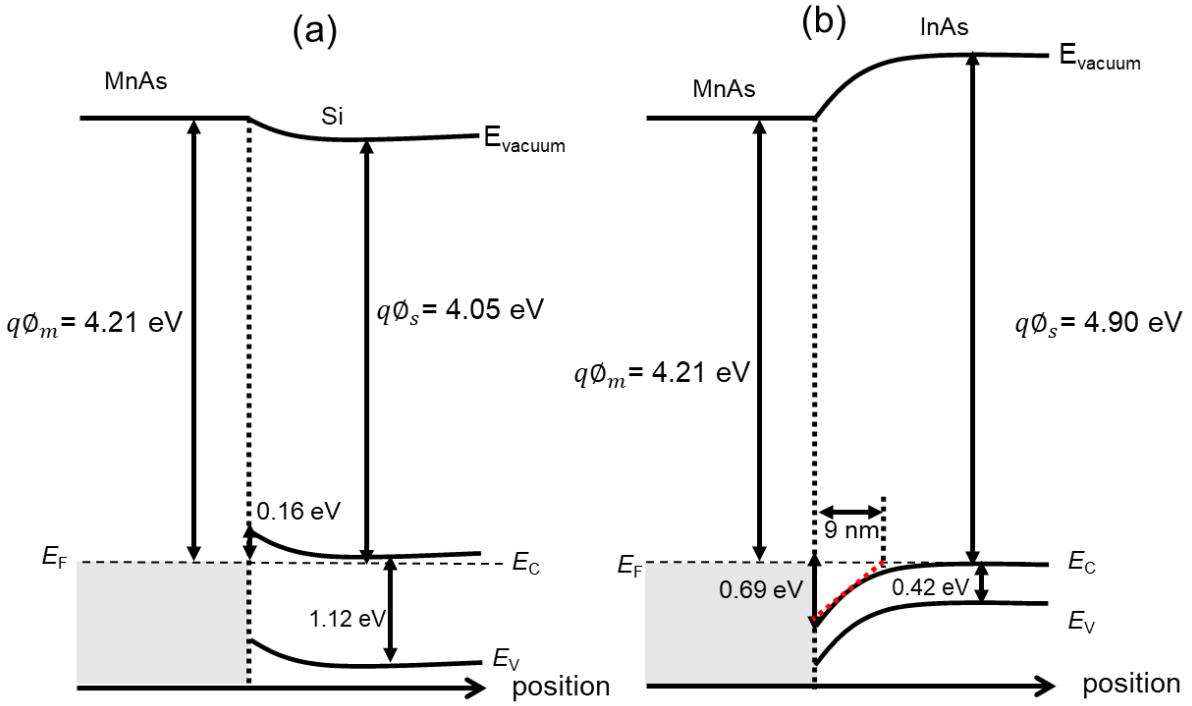

Fig.3.1 Energy band diagram of (a) MnAs/Si [2]; (b) MnAs/InAs contact expected from (a).

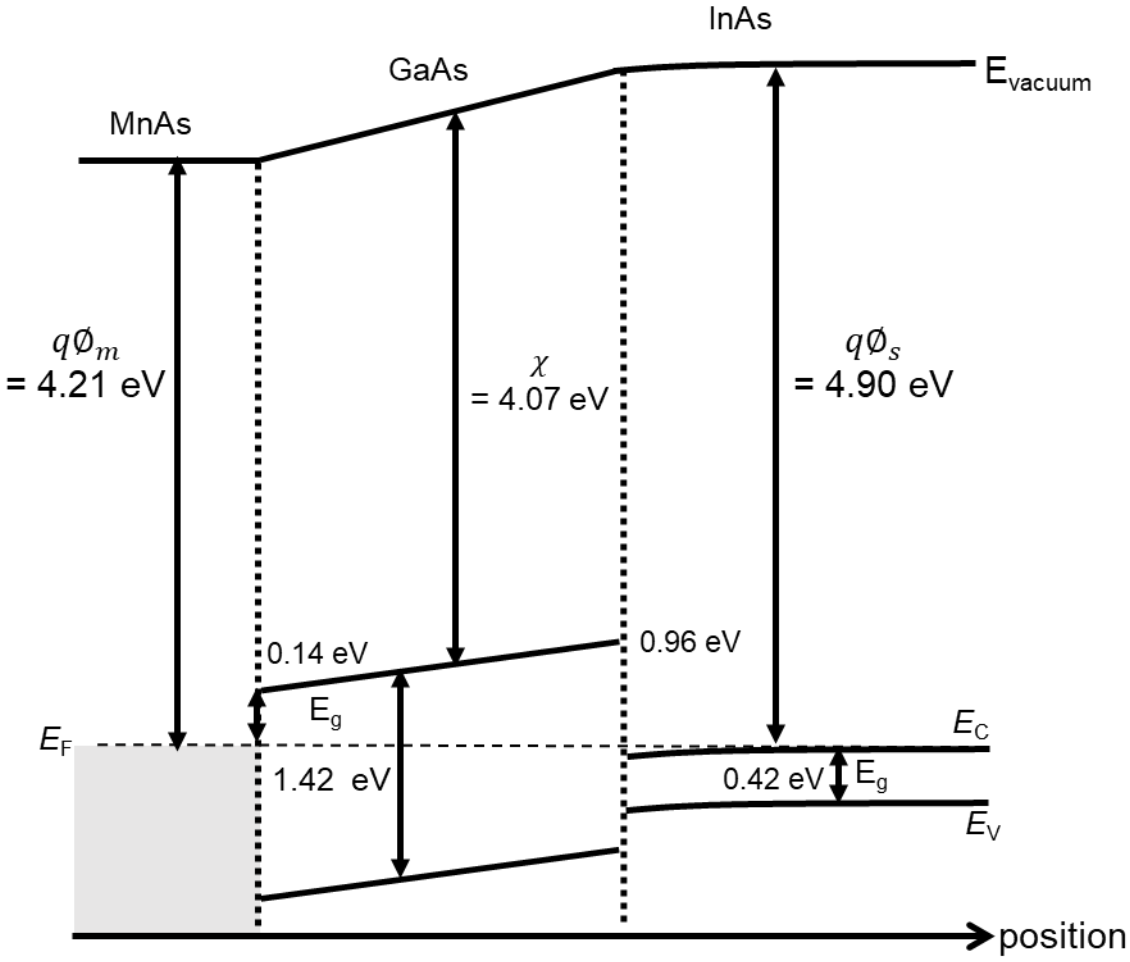

Fig.3.2 Energy band diagram of MnAs/GaAs/InAs contact.

However, to understand tunneling probability of conduction electron through the GaAs barrier. A details theoretical discussion has been carried out in appendix-A3.

However, to know expected Ohmic contact between MnAs/InAs, we studied transmission line model (TLM) device [5]. TLM is a lateral device structure. We study TLM to extract contact information of HT, LT1, LT2 samples. The detail of TLM processing and measurement has been discussed under section 3.2. We also investigated a trial of lateral spin valve device application of MnAs/GaAs/InAs/GaAs(111)B hybrid structures. The details of spin valve device processing and measurement has been discussed under section 3.3. Finally, a brief conclusion of this chapter has been discussed in section 3.4.

3.2 Transmission line model (T LM) device

To measure contact information between metal and semiconductor, there is resistance associated with Ohmic metal-to-semiconductor. The details of TLM basic has been discussed in appendix-A4. To evaluate the contact properties in detail, a test pattern composed of differently spaced contacts pad are prepared through TLM device processing. The detail of TLM processing and measurement has been discussed in section 3.2.1 and 3.2.2 respectively.

3.2.1 Device processing

We carried out photo-lithography technique to fabricate TLM device. The schematic of the TLM device process flow is shown in Fig.3.3 and the process steps are shown in table 3.1.

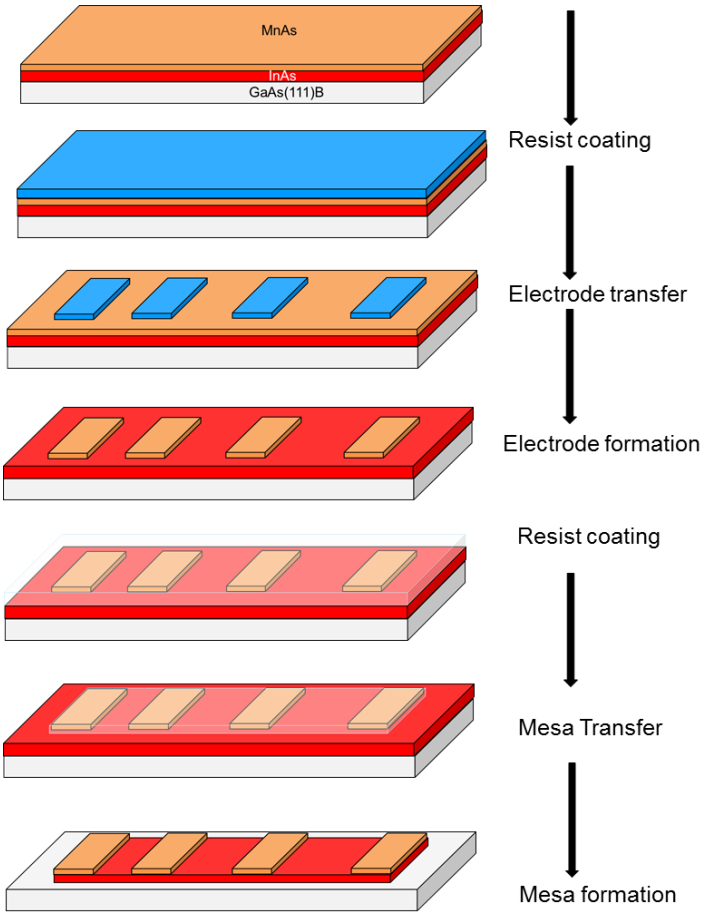

Fig.3.3 TLM device Process steps (top-down) schematic.

Table 3.1 Process steps (top-down) for TLM device

1. MnAs electrode formation		
Resist coating	Conditions & operation	comments
Image reversal (IR):		
Drying	HP 110 ^{0}C, 3min.	
Coating	AZ5214E, at 500 rpm, 3sec,4000 rpm 30 sec, 6000 rpm 2sec.(with slope 2)	
Baking	at 110 ^{o}C, 1min.	
UV exposure	60 mJ/cm^2, 5.5 sec.	With desired mask
Reversal bake	at 115 ^{o}C, 2min.	Critical
Flood exposure	300 mJ/cm^2, 27.5 sec.(10.9mw/cm^2)	Without mask
Developing	NMD-W 2min., DIW 2min. N_2 blowing	
Checking	Under microscope	Clean pattern
Etching		
Ashing	O plasma, 10w, 25Pa, 30sec.	
Etching	Etching: H_3PO_4: H_2O_2:H_2O (3:1:200) , 2min. DIW 2min., N_2 blowing	Etching of MnAs (240nm)
AZ5214E resist removal	In 1165 HP 60 ^{0}C, 15min. Acetone 5min., Methanol 5min. N_2 blowing	Avoid DIW for MnAs

2. InAs MESA formation		
Resist coating		
Drying	at HP 110 ^{0}C 3min.	
Coating	TSMR 8900, 500rpm 3sec, 4000 rpm ,60sec. 6000 rpm 2sec(slope 2sec)	
Baking	HP 110 ^{0}C, 1 min.	
Masking	Exposure 75mJ/cm^2 , 6.9 sec.	Make sure good alignment
Developing	NMD-W 1min. DIW 2min.	
Mesa formation		
Descum	O plasma, 10w, 25Pa, 30sec.	
Etching	H_3PO_4:H_2O_2:H_2O(3:1:50), 12min.; DIW 2min. N_2 blowing	Complete mesa: Etching rate : InAs 120nm/min, GaAs 100nm/min
Resist removal	1165 HP 60 ^{0}C, 5min, In acetone 2min. methanol. 2min. N_2 blowing	Avoid water for MnAs

Figure.3.4 shows a fabricated TLM device structure. The electrode width and length were ~180 µm and ~90 µm, respectively. This is close to design value 200 µm. The channel length were varied between ~10 µm and ~70 µm. The channel width and electrode width were same. However, due to MnAs electrode formation InAs channel etched out ~50 nm in between electrodes. Therefore we have modified TLM model by considering different thickness of InAs channel underneath MnAs electrode and in between MnAs electrodes in appendix-A4. There are significant side etching in wet chemical etching technique.

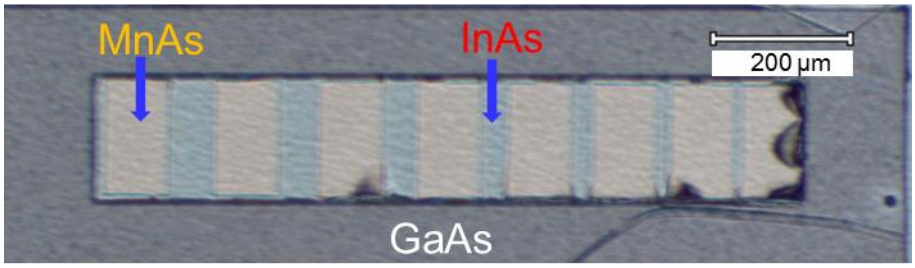

Fig.3.4 Optical microscope image of TLM device.

3.2.2 TLM measurement

Figure 3.5 shows schematic of measurement setup for TLM devices. We use device analyzer to measure the TLM devices. Figures 3.6 (a), (b) and (c) show current (I)-voltage (V)

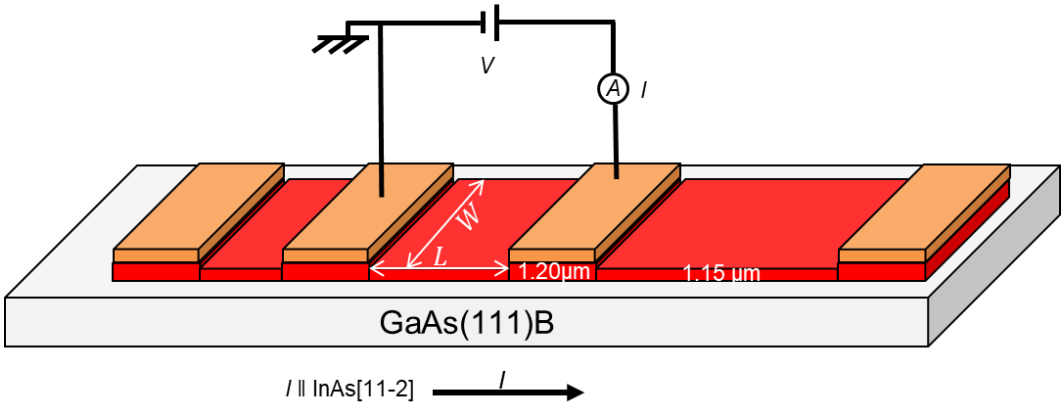

Fig. 3.5 TLM measurement configuration.

characteristics of TLM devices of HT, LT1 and LT2 samples respectively with the current flow along [11-2] lateral direction of cubic InAs. Each curve is linear. Therefore, we can conclude MnAs/InAs interface is Ohmic contact as expected.

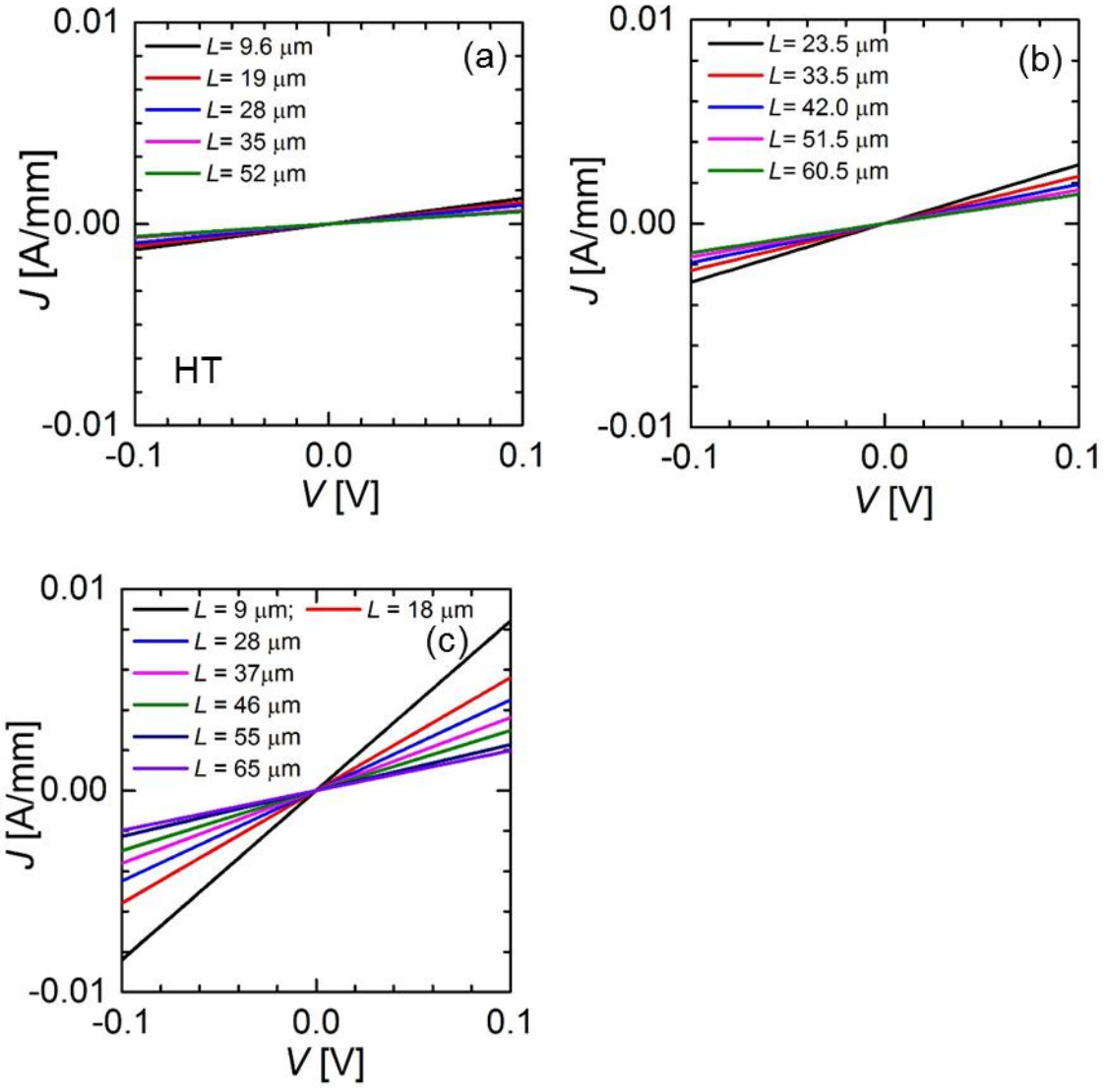

Fig.3.6 Current-voltage characteristics of TLM devices of (a) HT, (b) LT1 and (c) LT2 samples with current flow along InAs [11-2] direction.

Figure 3.7 (a) and (b) shows TLM plots of HT, LT1 and LT2 samples, and isotropic plots in-plane directions of LT1 sample (only) respectively. The extracted electrical parameters from TLM plots, sheet resistance (ρ_{s2}) of InAs channel, and sheet resistance (ρ_{s1}) underneath electrode extraction method has been mentioned in appendix-A4. The contact resistance, (R_c) between MnAs/InAs and specific contact resistance (ρ_c) are summarized in table 3.2.

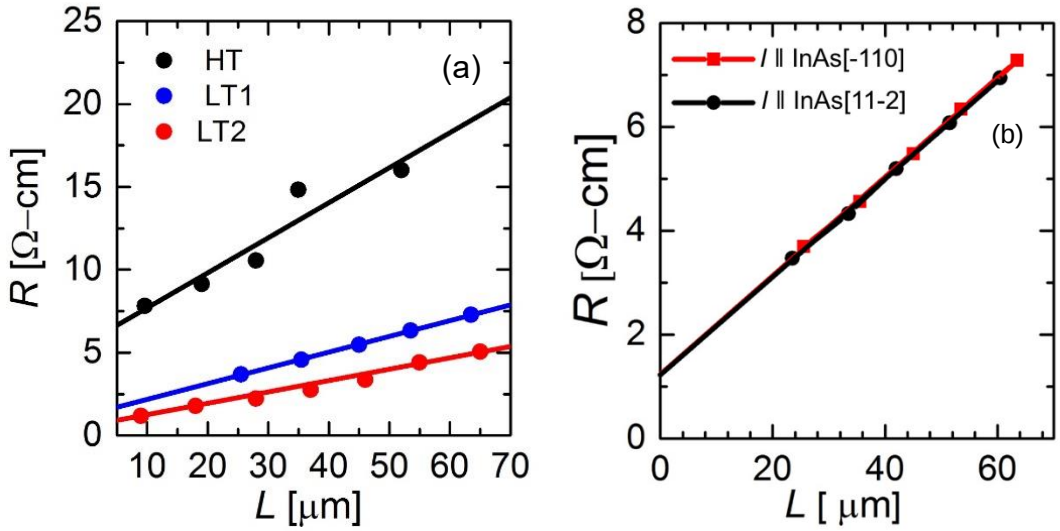

Fig. 3.7 (a) TLM plots of HT, LT1 and LT2 samples. (b) Isotropic TLM of LT1 sample

Table 3.2 Extracted TLM parameters

Sample	ρ_{s1}[Ω/sq.]	R_c[Ω-cm]	$L_t = R_c/\rho_{s1}$ [μm]	$\rho_c = \frac{R_c^2}{\rho_{s1}}$ [Ω-cm^2]
HT	2023	2.8	13.8	$3.8x10^{-3}$
LT1	910	0.6	6.6	$3.9x10^{-4}$
LT2	660	0.2	3.0	$6.0x10^{-5}$

From the table 3.2, we see HT sample shows very higher (ρ_{s1}) and ρ_c than LT1 and LT2 samples. The reason is due to rough sample surface which results in increasing the resistance. The ρ_{s1} of LT1 and LT2 samples seems not significant different in their TLM properties. Above all, the low temperature grown MnAs samples seems better electrical properties. However, low temperature grown MnAs samples have little higher specific contact resistance through MnAs/InAs interface than typical Ohmic contact of III-V semiconductors [6].

3.3 Lateral spin valve device

To confirm spin injection (Inj.), transport and detection (Det.) into MnAs/GaAs/InAs/GaAs(111)B hybrid structures. We attempt to process lateral spin valve geometry of this structure. The details of device processing and measurements have been discussed in section 3.3.1 and 3.3.2 sections.

3.3.1 Device processing

We fabricated lateral spin-valve devices of chip size (2x2) mm^2. We carried out electron-beam lithography (EBL) for FM MnAs electrode formation. With considering the side etching of MnAs as mentioned in TLM processing and also considering LSV device size, we used the combination of electron-beam lithography (EBL) and Ar+ ion beam etching to precisely control device size. The Ar^+ etching is expected to be advantageous point for avoiding side etching. The etching rate of MnAs, GaAs and InAs were ~25 nm/min, ~30 nm/min and ~100 nm/min respectively. The dteails of process flow is shown in Fig. 3.8. Table 3.1 shows the details of process steps.

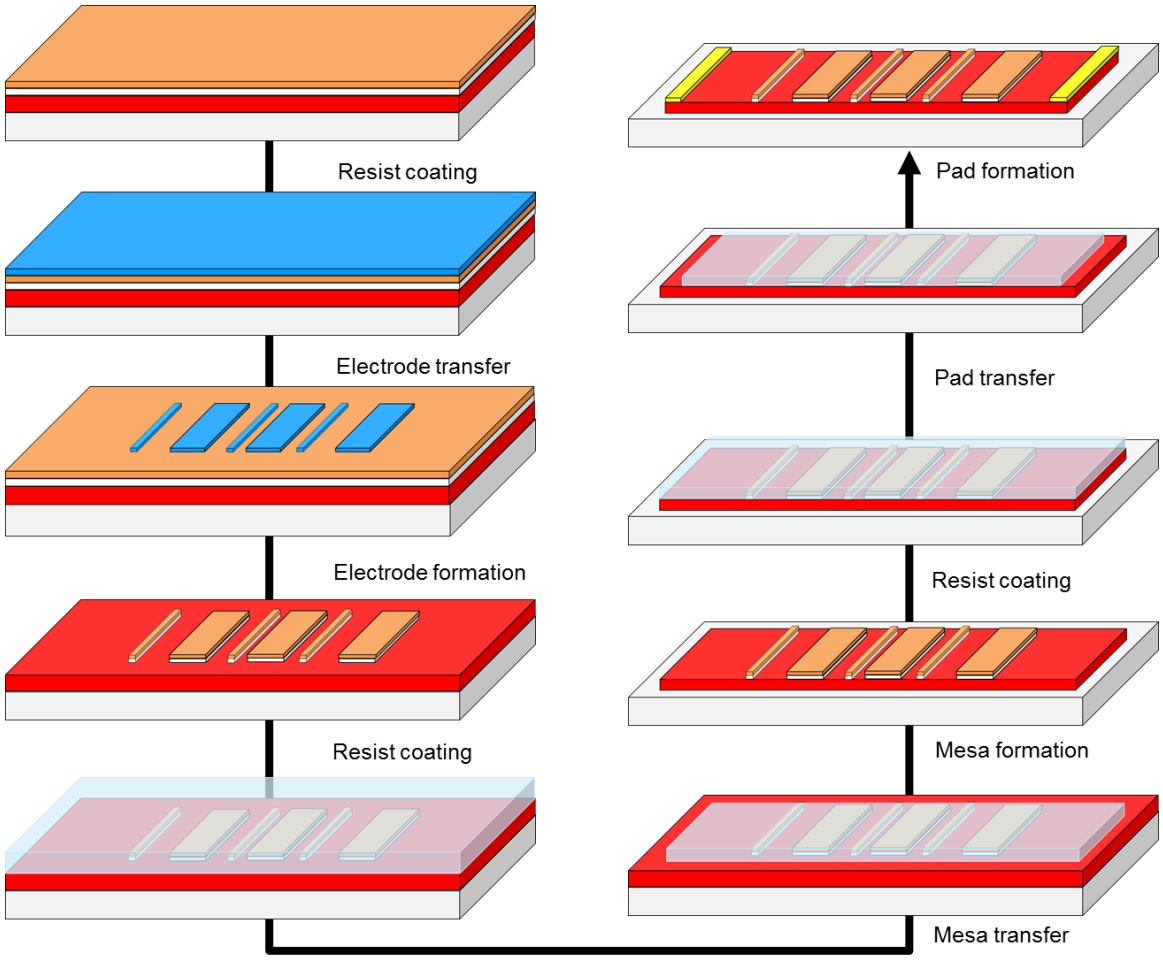

Fig.3.8 Lateral spin valve device process flow.

Table 3.1 lateral spin valve device process steps

1. MnAs/GaAs Electrode formation		
Process	Action and condition	Comments
Cleaning	Acetone dip (3min); Methanol dip (3min) ,N_2 blow	
Baking	Hot-plate (110 ^{0}C, 3 min)	
OAP coat	N_2 blowing, OAP dropping 500rpm 3sec, slope 2sec 3000rpm 30sec, slope 2sec Hot-plate (110 ^{0}C, 3min)	
SAL601-SR7 coat	N_2 blowing SAL601-SR7 dropping 500rpm 3sec, slope 2sec 4000rpm 60sec, slope 2sec Hot-plate (110 ^{0}C, 1min)	
Lithography	Exposure (4-8μC/sqcm, 50pA, 0.7μs)	
Post exposure baking	Hot-plate (100 ^{0}C, 5min)	
Development	NMD-W (12min) DIW dipping (3min)	
Baking	Hot-plate (120 ^{0}C, 5min)	
Descum	Ashing (O_2, 50Pa, 150W, 0.5min)	

Ar+ etching	ECR(Ar: 1sccm, 500eV, 100W, 2.5 min) (I_E: 10-11mA, J_I: 0.75-0.8mA/sqcm)	(60-70)nm
Resist removal	1165 dipping (60 ^{0}C,15min) Methanol dip (3min) N_2 blow Ashing (O_2, 50Pa, 30W, 2-3min)	MnAs moisture sensitive
2. InAs MESA formation		
Cleaning	Acetone dip (3min) Methanol dip (3min) N_2 blow	
Baking	Hot-plate (110 ^{0}C, 3 min)	
OAP coat	N_2 blowing OAP dropping 500rpm 3sec, slope 2sec 3000rpm 30sec, slope 2sec Hot-plate (110 ^{0}C, 3min)	
SAL601-SR7 coat	N_2 blowing SAL601-SR7 dropping 500rpm 3sec, slope 2sec 4000rpm 60sec, slope 2sec Hot-plate (110 ^{0}C, 1min)	
Lithography	Exposure (4-8μC/sqcm, 50pA, 0.7μs)	
Post exposure baking	Hot-plate (100 ^{0}C, 5min)	
Development	NMD-W (12min)	

	DIW dipping (3min)	
Baking	Hot-plate (120 ^{0}C, 5min)	
Descum	Ashing (O_2, 50Pa, 150W, 0.5min)	
Ar+ etching	(Ar: 1sccm, 500eV, 100W, 4.5min) (*I*$_E$: 10.6mA, *J*$_I$: 0.78mA/sqcm)	260-270 nm
Resist removal	1165 dipping (60 ^{0}C, 20min) Acetone (3min) Methanol dip (3min) N_2 blow Ashing (O_2, 50Pa, 30W, 1 min)	
3. Ti/Au metal pad formation		
Cleaning	Acetone dip (3min) Methanol dip (3min) N_2 blow	
Baking	Hot-plate (110 ^{0}C, 3 min)	
Resist coat	N_2 blowing LOL-2000 dropping 500rpm 3sec, slope 2sec, 3000rpm 30sec, slope 2sec 6000rpm 2sec slope 2sec Hot-plate (180 ^{0}C, 3min) N_2 blowing, TSMR 8900 dropping 500rpm 3sec, slope 2sec 4000rpm 60sec, slope 2sec 6000rpm 2sec slope 2sec	

	Hot-plate (110 ^{0}C, 1.5min)	
Lithography	Exposure (70-80mJ/sqcm)	
Development	NMD-W dipping (60sec) DIW dipping (2min) N_2 blowing	
Descum	Ashing (O_2, 50Pa, 10W, 30sec) Semico-clean dipping (3min) DIW dipping (3min) N_2 blowing	
Evaporation	Vaccum pressure (~10^{-4} Pa) Ti (~0.05nm/sec, 10nm) Au (~0.3nm/sec, 150nm)	
Lift-off	1165 dipping on hot-plate (60 ^{0}C) Acetone dipping(3min) Methanol dipping(3min) N_2 blowing	

We have observed almost no side etching during MnAs/GaAs electrode and InAs channel formation. Figure.3.9 shows an optical image of the fabricated device structure.

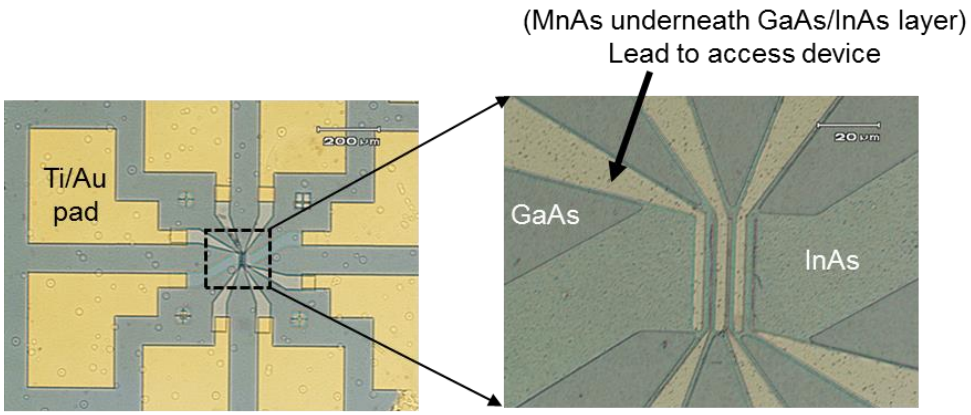

Fig.3.9 Optical microscope image of lateral spin valve device geometry.

3.3.2 Non-local spin valve (NLSV) measurements

Typically, the NLSV signal is measured outside the input circuit. The concept of NLSV measurement is shown in Fig. 3.10 (a) where the input bias between Ohmic and FM electrode and non-local voltage measured between one different size FM near input FM and Ohmic electrode. We can measure pure spin current as clearly seen in electro-chemical potential distribution with bias electric field as shown in Fig. 3.10 (b).

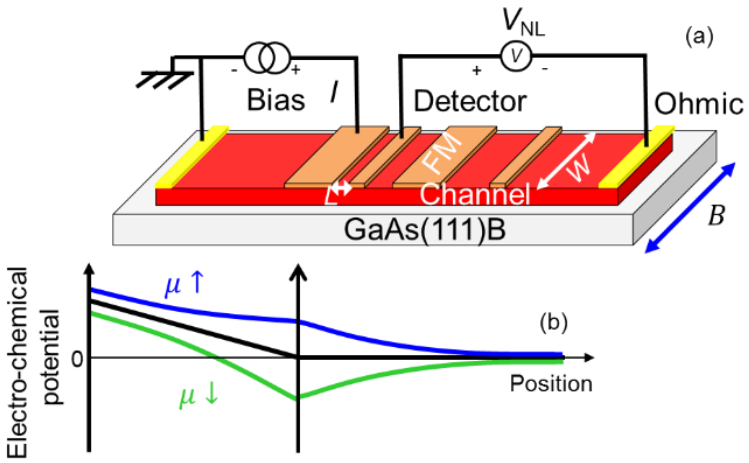

Fig. 3.10 (a) NLSV measurement circuit (b). Electro-chemical potential distribution with bias electric field.

However, to observe spin valve signal we carried out magnetization switching behavior of the designed FM electrodes by MFM measurement. We could clearly observe magnetization switching in lateral direction. The details of magnetization switching behavior is shown in Fig. 3.11 which is hopeful for lateral spin valve device application.

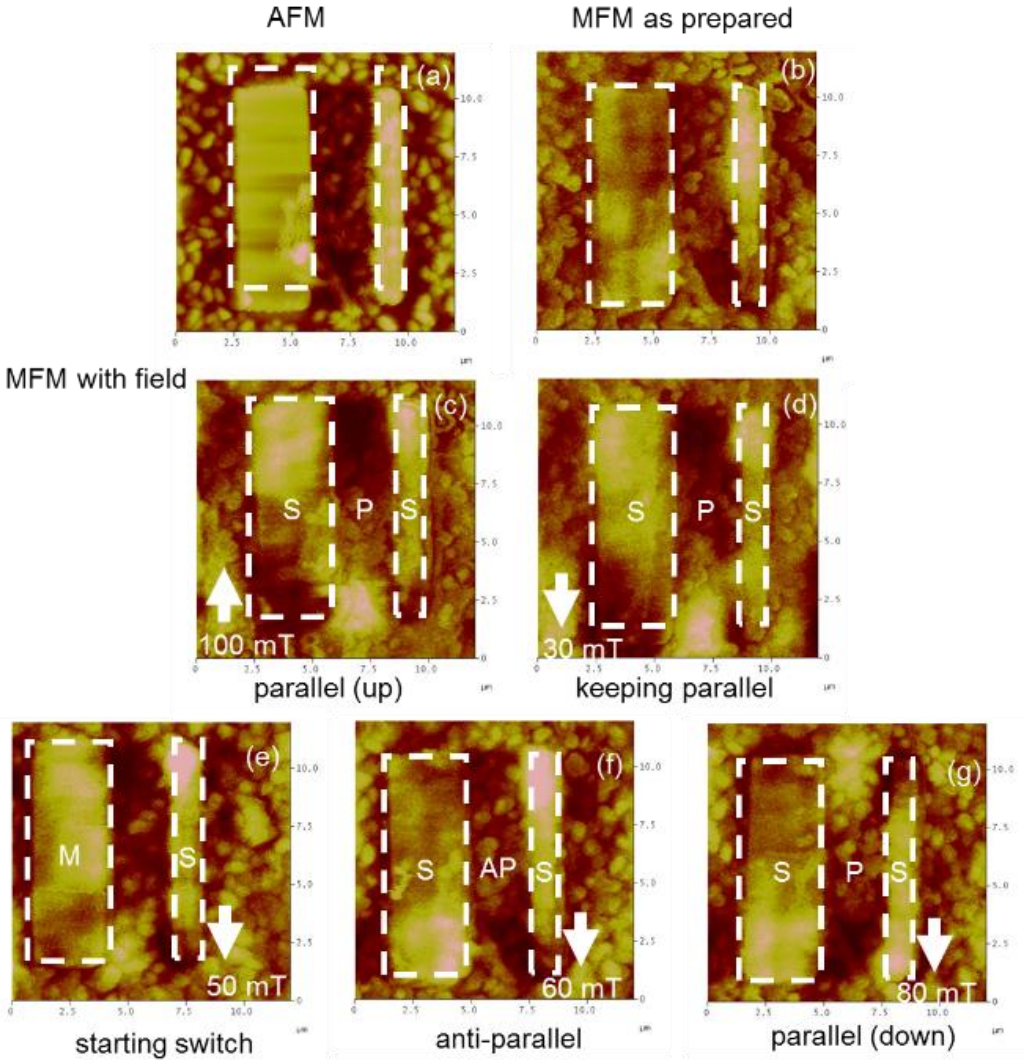

Fig. 3.11 No external magnetic field (a) AFM, (b) MFM; MFM with applied magnetic field (c) applied field 100 mT makes parallel (P) magnetization of electrodes, (d) Opposite direction magnetic field applied 30 mT to start switching magnetization directions, (e) Magnetic field increased to 50 mT seems magnetic switching, (f) 3 µm size FM switched earlier than 1 µm as expected which makes antiparallel (AP) state, (g) 1 µm FM switching complete becomes parallel.

Figure 3.12 (a) shows a schematic of NLSV measurement configuration for both samples. We carried out electrical measurement of the configuration at 1.5 K with AC lock-in technique setting lock in frequency 397 Hz. The input current was 1 µA (AC). We superimposed 10 µA

(DC) with 1 µA (AC) input to make AC current flow in one direction. We sweep magnetic field (B) between ± 150 mT parallel to GaAs[-110] and current flow through InAs channel along GaAs[11-2] lateral directions. Appendix A-5 shows details of the low temperature measurement setup. We converted the measured non-local voltage, V_{NL} (AC) in terms of R_{NL} resistance signal by diving the measured voltage by the 1 µA (AC) input current. The NLSV signals are unclear and seems obscured by noise of both samples. The similar behavior repeats when we exchange the injection and detection FM.

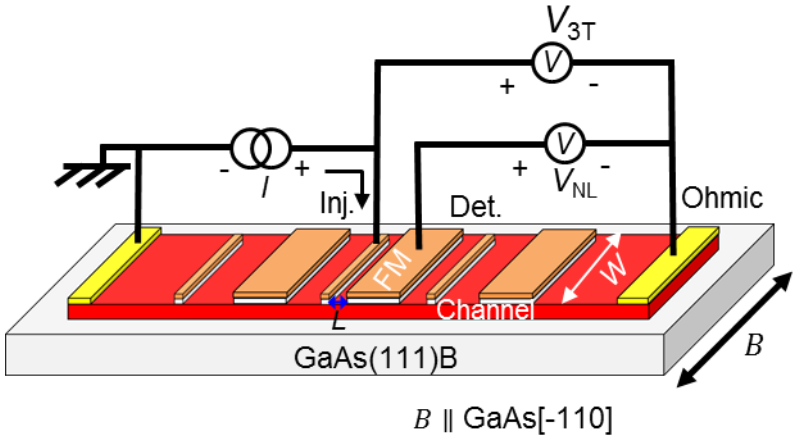

Fig.3.12 NLSV measurement configuration.

Fig. 3.13 (a) and (b) show NLSV curves at FM electrode spacing 1 µm of 1 and 3 nm GaAs insertion samples respectively.

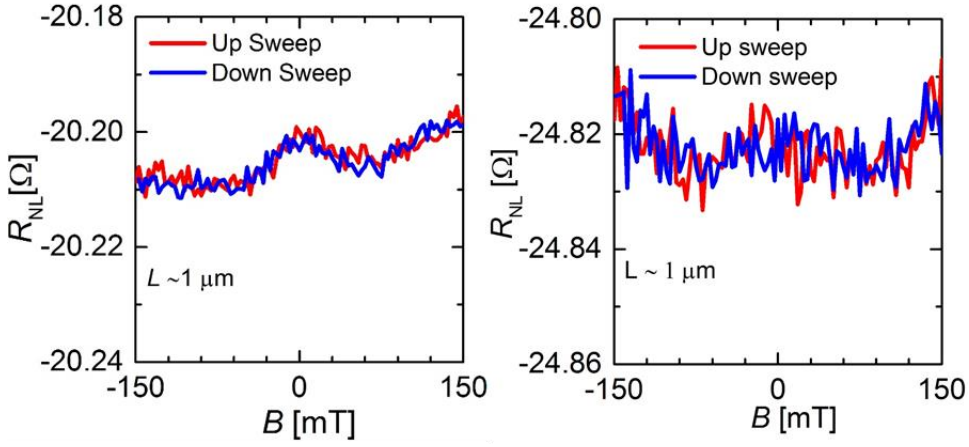

Fig.3.13 Unclear NLSV signal of (a) 1 nm GaAs, (b) 3nm GaAs insertion samples.

The reason why NLSV unclear because, from 3-terminal measurement, we see very small difference of the magnetization switching between 0.5 and 3 µm size FM electrodes as can be seen from the 3-terminal subtraction signal shown in Fig.3.14. The difference between them seems ~10 mT.

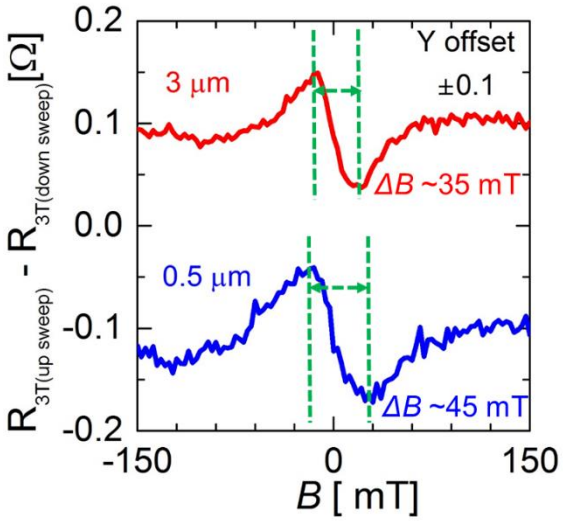

Fig.3.14 3-terminal subtraction signal of 3 and 0.5 µm electrode.

It seems larger size device accessing lead (Fig.3.9) than FM electrode in the device dominating switching behavior of FM electrode in the device. Also, from TLM study under section 3.2, chapter 3, we see transfer length ~ 3 µm. As the device accessing lead is far away from device and larger length laterally than transfer length, there is a possibility of current penetration around device accessing lead which may weaken input current into the device.

Therefore, considering these possible problems, we have processed device with replacing the device accessing lead with ferromagnetic Ni to keep constant current input into the device. The details of device processing will be discussed in section 3.3.3.

3.3.3 Modified lateral spin valve device processing

We kept same device geometry same as discussed in section 3.3.1. We have only replaced device accessing lead with Ni lead. We used GaAs 1 nm insertion sample for the device processing. The main steps of device processing are as follows;

1. InAs mesa formation
2. MnAs/GaAs electrode formation
3. Ni lead formation
4. Ti/Au metal pad formation

Figure.3.15 shows the details of processed device image. Table 3.2 shows process steps details.

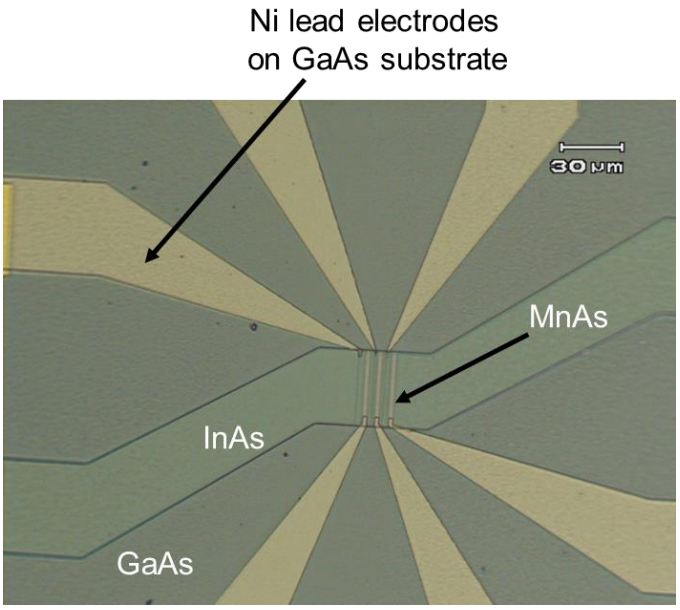

Fig.3.15 Optical microscope image of modified lateral spin valve device geometry.

Table 3.2 Modified lateral spin valve device process steps

1. InAs Mesa formation		
Process	Action and condition	Comments
Cleaning	Acetone dip (3min); Methanol dip (3min) ,N_2 blow	
Baking	Hot-plate (110 ^{0}C, 3 min)	
OAP coat	N_2 blowing, OAP dropping 500rpm 3sec, slope 2sec 3000rpm 30sec, slope 2sec Hot-plate (110 ^{0}C, 3min)	
SAL601-SR7 coat	N_2 blowing SAL601-SR7 dropping 500rpm 3sec, slope 2sec 4000rpm 60sec, slope 2sec Hot-plate (110 ^{0}C, 1min)	
EB Lithography	Exposure (4-8μC/sqcm, 100 pA, 0.7μs)	
Development	NMD-W (1.5min) DIW dipping (10 min)	
Ar+ etching	ECR(Ar: 1sccm, 500eV, 100W, 4.5min) (I_E: 10.6mA, J_I: 0.78mA/sqcm)	260-270 nm
Resist removal	1165 dipping (60 ^{0}C, 20min) Acetone (3min)	

	Methanol dip (3min) N_2 blow Ashing (O_2, 50Pa, 30W, 1 min)	
2. MnAs/GaAs electrode formation		
Cleaning	Acetone dip (3min) Methanol dip (3min) N_2 blow	
Baking	Hot-plate (110 ^{0}C, 3 min)	
OAP coat	N_2 blowing OAP dropping 500rpm 3sec, slope 2sec 3000rpm 30sec, slope 2sec Hot-plate (110 ^{0}C, 3min)	
SAL601-SR2 coat	N_2 blowing SAL601-SR2 dropping 500rpm 3sec, slope 2sec 4000rpm 60sec, slope 2sec Hot-plate (110 ^{0}C, 1min)	
EB Lithography	Exposure (4-8μC/sqcm, 50pA, 0.7μs)	
Development	NMD-W (2min), DIW water dipping (3min)	
Ar+ etching	ECR(Ar: 1sccm, 500eV, 36 W, 2.5 min) (I_E: 4.0mA, J_I: 0.30mA/sqcm)	(60-70)nm
Resist removal	1165 dipping (60 ^{0}C,1hour),ultrasonic 1165(40% 2min)	MnAs moisture sensitive

	Acetone (3min) Methanol dip (3min) N_2 blow	
3. Ni lead formation		
Cleaning	Acetone dip (3min) Methanol dip (3min) N_2 blow	
Baking	Hot-plate (110 ^{0}C, 3 min)	
Resist coat	N_2 blowing LOL-2000 dropping 500rpm 3sec, slope 2sec, 3000rpm 60sec, slope 2sec Hot-plate (180 ^{0}C, 3min) N_2 blowing, GL-2000-M dropping 500rpm 3sec, slope 2sec, 4000rpm 60sec, slope 2sec Hot-plate (180 ^{0}C, 3min)	
EB Lithography	100 pA, 4.5 μsec	
Development	ZED-N50 dipping (1 min) ZMD-B dipping (30 sec) NMD-W dipping (5sec) DIW (1min) N_2 blowing	
Descum	Ashing (O_2, 50Pa, 10W, 30sec) Semico-clean dipping (3min)	

	DI water dipping (3min) N_2 blowing	
Evaporation	Vaccum pressure (~10^{-4} Pa) Ni (~1Å/sec, 100nm)	
Lift-off	1165 dipping on hot-plate (60 ^{0}C) Acetone (3min) Methanol dipping (3min) N_2 blowing	
4. Ti/Au pad formation		
Cleaning	Acetone dip (3min) Methanol dip (3min) N_2 blow	
Baking	Hot-plate (110 ^{0}C, 3 min)	
Resist coat	N_2 blowing LOL-2000 dropping 500rpm 3sec, slope 2sec, 3000rpm 60sec, slope 2sec 6000rpm 2sec slope 2sec Hot-plate (180 ^{0}C, 3min) N_2 blowing, TSMR 8900 dropping 500rpm 3sec, slope 2sec 4000rpm 60sec, slope 2sec 6000rpm 2sec slope 2sec Hot-plate (110 ^{0}C, 1.5min)	
Photo lithography	Exposure (100mJ/sqcm)	

Development	NMD-W dipping (60sec) DIW dipping (2min) N_2 blowing	
Descum	Ashing (O_2, 50Pa, 10W, 30sec) Semico-clean dipping (3min) DIW dipping (3min) N_2 blowing	
Evaporation	Vaccum pressure (~10^{-4} Pa) Ti (~3Å/sec, 5nm) Au (~3Å/sec, 200nm)	
Lift-off	1165 dipping on hot-plate (60 ^{0}C) Acetone dipping(3min) Methanol dipping(3min) N_2 blowing	

3.3.4 Local and non-local spin valve (LSV and NLSV) measurements

We focus on simultaneous measurements of local and non-local spin valve at two different input configurations to investigate spin injection, detection. One is input between FM-NM and another one is input between FM-FM. We compare their behaviors in details through LSV and NLSV measurements to understand in depth about spin-related parameters and their relations. Figure 3.16 (a) and (b) show device schematic and measurement configuration for local (V_L) and non-local (V_{NL}) (AC) voltages measurements with FM-NM and FM-FM input cases respectively. We carried out electrical measurement at 1.5 K and 300K with AC lock-in technique setting lock in frequency 397 Hz. The input current was 1 μA (AC). We superimposed 10 μA (DC) with 1 μA (AC) input to make AC current flow in one direction. At 1.5 K, We sweep magnetic field (B) between ± 600 mT parallel to GaAs[-110] and current flow through InAs channel along GaAs[11-2] lateral directions. Here also, we similarly converted the measured V_{3T}, V_L and V_{NL} voltages (AC) in terms of R_{3T}, R_L and R_{NL} resistance by diving the measured AC voltages by 1 μA (AC) input current. In Figure. 3.17 (a), the 3T resistances (R_{3T}) for the two different size FM electrodes show different magnetization switching field to create parallel and anti-parallel state in spin valve measurements. The subtraction of R_{3T} up sweep and down sweep as shown in Fig. 3.17 (b) clearly indicates that 0.5 μm and 3 μm have ~110 mT difference in their hysteresis. Also we have measured R_{3T} at B=0 with sweeping DC bias current with superimposed with 1 μA (AC) current to see the contact nature of MnAs/GaAs/InAs. Figure 3.18 shows the resistance area product (RA) response seems tunnel like nature at varying DC bias.

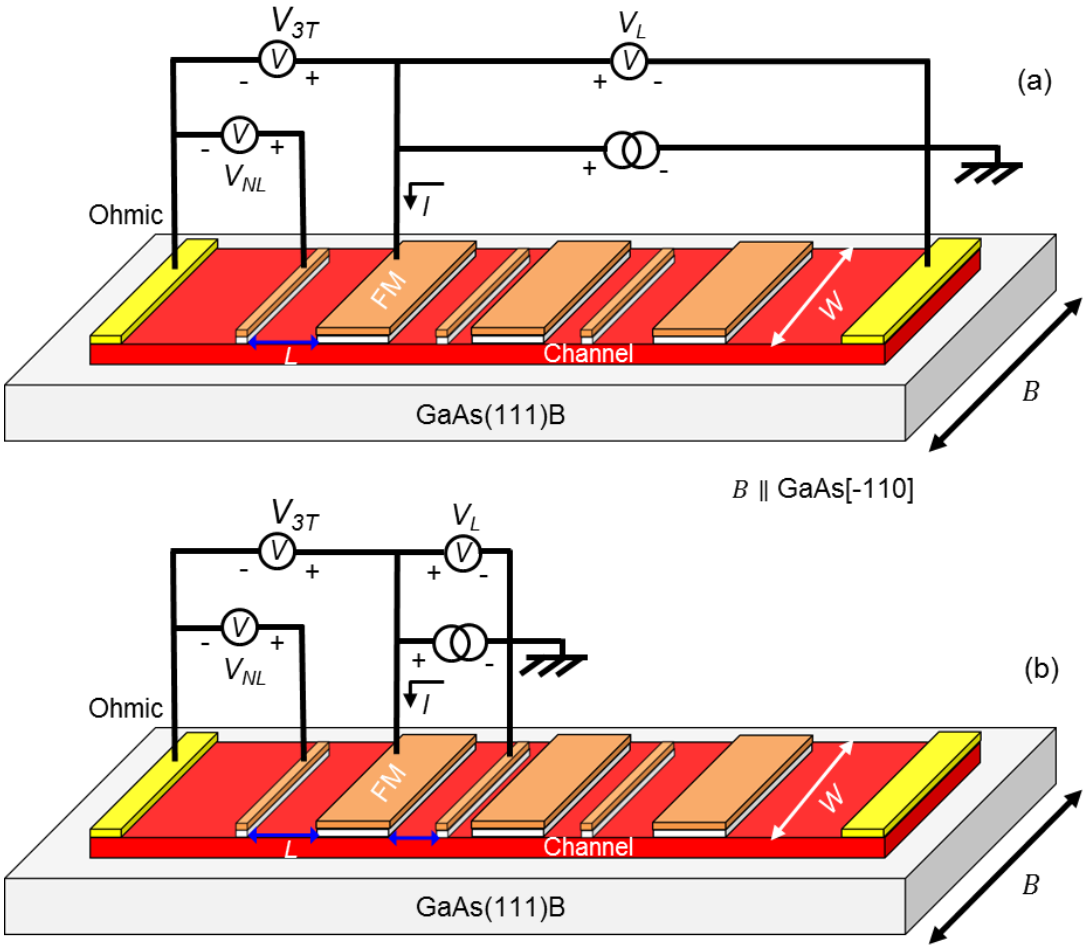

Fig. 3.16 Device schematic structure and measurement configuration for local and non-local at input between (a) FM-NM and (b) FM-FM.

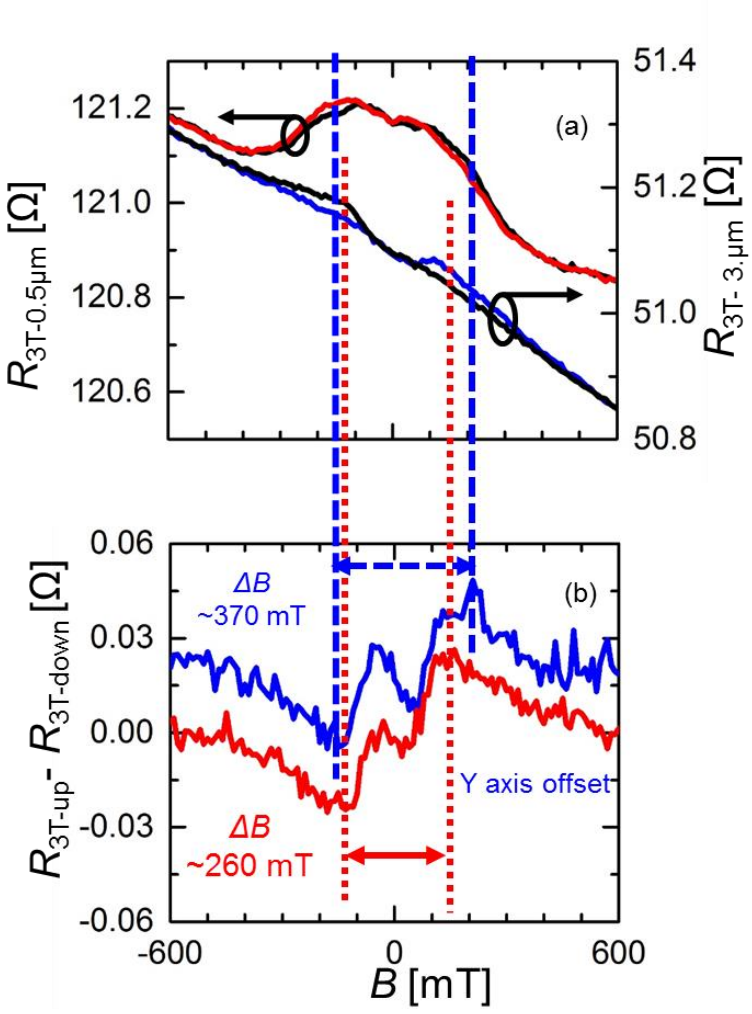

Figure. 3.17 (a) 3T resistances (R_{3T}) for 0.5 µm and 3 µm FM electrodes show different magnetization behavior (b) Clearly indicates that 0.5 µm and 3 µm have ~110 mT difference in their hysteresis.

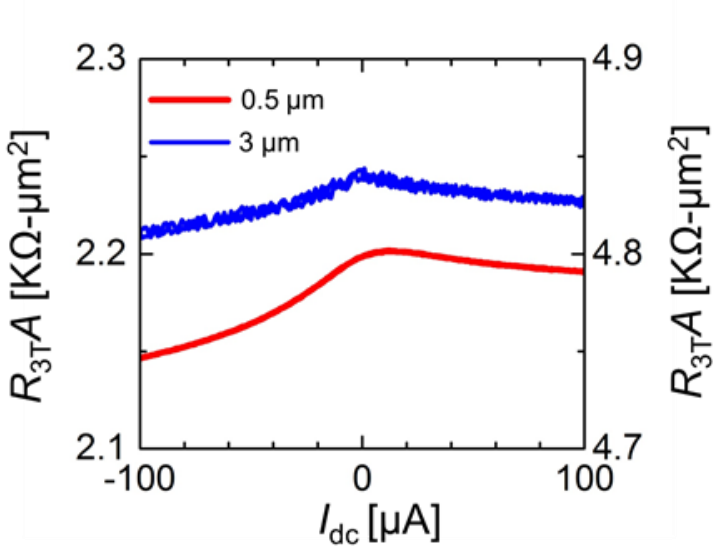

Figure. 3.18 (a) 3T resistance area product for 0.5 µm and 3 µm versus DC bias current

However, the local R_L between FM-NM electrodes with sweeping magnetic field shows no hysteresis as shown in Fig.3.19 (a) and R_L between FM-FM shows spin valve like hysteresis as shown in Fig.3.19 (b). This LSV like hysteresis behavior implies that it comes from different switching behavior of two different size input FM electrodes which is well-known phenomenon in spin valve study. However, the large difference in resistance in local measurement due to measurement electrode separation. In the case of FM-NM the separation several 10's μm but in the case of FM-FM the separation only 2 μm. Another point the contact difference between FM-NM and FM-FM contributes in the resistance values.

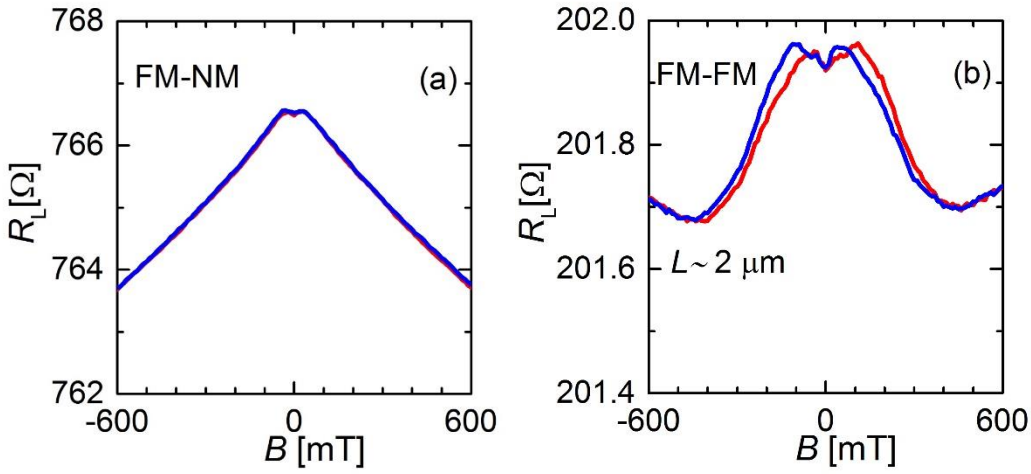

Fig. 3.19 (a) Absence of LSV hysteresis between FM-NM local circuit and (b) LSV between FM-FM local circuit.

However, we also observed clear NLSV hysteresis with input between FM-NM and FM-FM cases. Figure.3.20 (a, c) and (b, d) shows NLSV hysteresis curves at different channel lengths in the case of input between FM-NM and FM-FM respectively. In the case of FM-FM input, the simultaneously-measured non-local signal, R_{NL} seems ~2 times larger than that of the non-local signal in FM-NM input case. This enhancement of non-local signal mainly comes from the two FM-FM electrodes contribution. This is because in parallel magnetization between two

close FM electrodes in the local circuit, spin accumulation i.e electrochemical potential ($\mu_{channel}$) in the non-local channel become zero due to opposite direction spin current flow across the two input FM interface cancel out each other (each electrode has equal contribution as mentioned earlier). On the other hand, in anti-parallel condition the $\mu_{channel}$ become constructive (twice) because the spin current induced by each FM flow in the same direction and hence it is expected to enhance total R_{NL} in the NLSV measurement. Enhancement of non-local signal also have been observed in FM/metal system if FM-FM is used in the spin injection circuit [7-9].

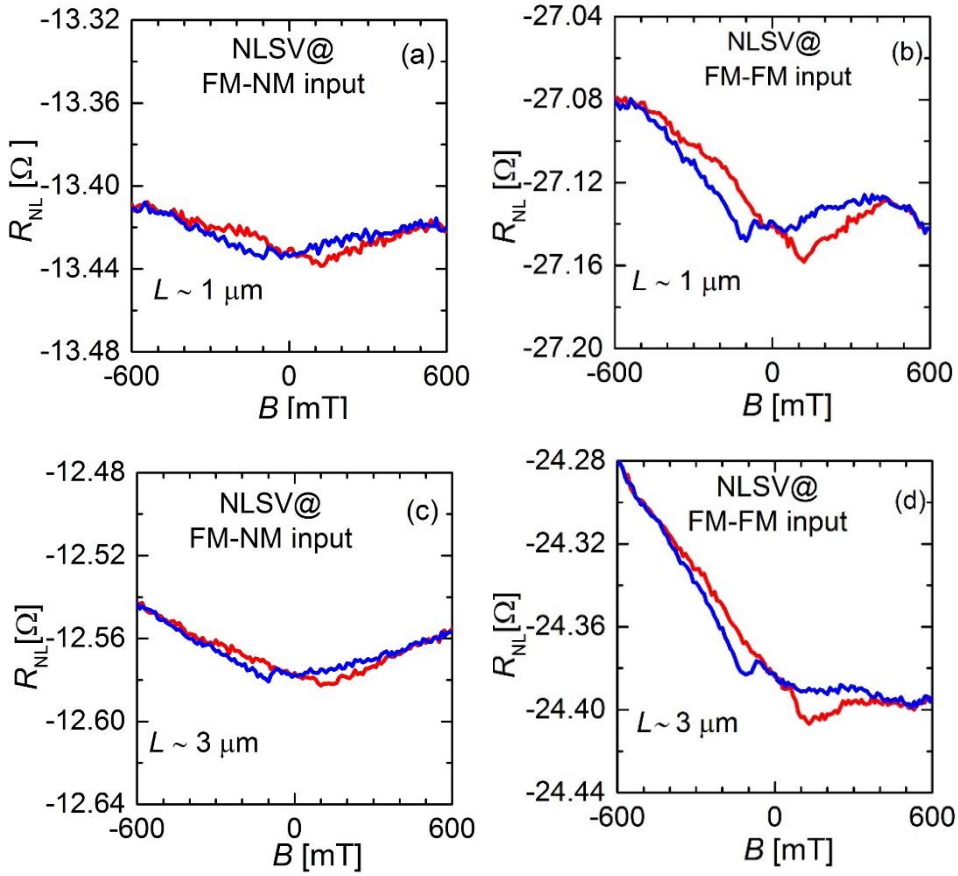

Fig. 3.20 NLSV hysteresis curves at different channel length in the case of input between (a,c) FM-NM and (b,d) FM-FM.

To study in depth about spin injection and detection in LSV and NLSV measurements, we carried out similar measurements at different channel length and extracted LSV and NLSV amplitude signals (ΔR) from the subtraction of up and down-sweep signals as shown in Fig.3.21

(a). We find LSV and NLSV amplitude signals at different channel length as shown in Fig.3.21 (b) seems exponentially decaying with increasing L which implies spin transport in LSV and NLSV measurements.

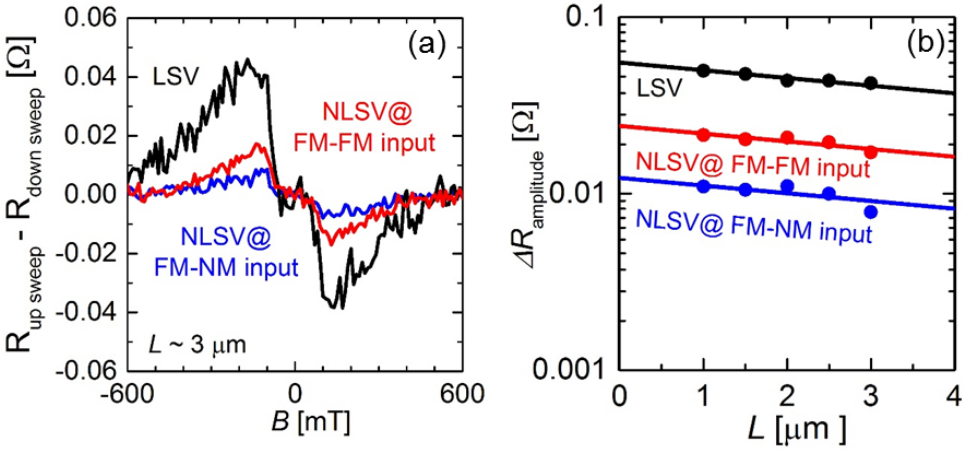

Fig. 3.21 (a) Subtracted signal of up sweep and down sweep of LSV and NLSV signals at 3μm channel length and (b) Extracted channel length dependent signal amplitude from subtracted signal for LSV and NLSV.

Hence, spin accumulation at interface can be written in the form [10, 11];

$$\Delta R(L) = \Delta R_0 \exp\left(\frac{-L}{L_S}\right) \quad (3.2).$$

Where, ΔR_0 is the amplitude at $L = 0$, L_s is the spin diffusion length. From the exponential fitting lines (not shown here), the fitting parameters L_S seems widely deviated in each measurement conditions as summarized in table 3.3.

Table 3.3 Extracted parameters form spin valve measurements

Parameter	NLSV FM-NM input	NLSV FM-FM input	LSV FM-FM input
L_s [μm]	8±4	11±3	12±2
ΔR_0 [Ω]	0.013±0.001	0.024± 0.001	0.054±0.001

As drift electric field only exists in local channel, as a consequence the field can play important role to enhance, L_S in LSV than NLSV measurement. We found drift electric field is around ~100 μV/μm in our measurement and also we examine the, L_S value of LSV and NLSV measurements. The L_S values of LSV and NLSV measurements which are similar to each other even though they have large deviation which implies the local drift field has no significant effect on L_S values in LSV measurement. Also we see insignificant deviation of amplitude ΔR_0. We think the deviations mainly have come due to scatter data points. Therefore, we have assumed one fixed value L_S ~10 μm which suits well for fitting lines as shown in Fig.3.21 (b). We also see amplitude enhancement in NLSV and LSV in FM-FM input case than FM-NM input case but the L_S and η should be same in NLSV and LSV at FM-FM input case also. Therefore, we can introduce an amplitude enhancement factor, (α) in LSV and NLSV measurements which can be written as [8, 9] ;

$$\Delta R_0 = \alpha \frac{\eta^2 \rho_S L_S}{W} \quad (3.3).$$

Where, η is the spin polarization at L =0, ρ_S sheet resistance and it is ~180 Ω/sq. at 1.5 K of the InAs channel and channel width, W is ~40 μm. We assume, α=1 for NLSV in the case of FM-NM input because only diffusive spin transport between single FM electrode in the input

to non-local detection FM electrode. Now using, α=1 and with the values of L_S, ρ_S and W, the calculated η value is ~1.6%. Using the η value, we have calculated α values from equation (3.3) for NLSV and LSV in the case of FM-FM input and the values are ~2.0 and 4.7 for NLSV and LSV respectively. Considering the two FM electrodes contribution, the NLSV amplitude enhancement factor ~2.0 seems reasonable. Details of extracted parameter are summarized in table 3.4. Moreover, we see significantly large enhancement of LSV signal amplitude which is deviated from well-established theoretical relation between local and non-local signal amplitude of one-dimensional spin diffusion model [11, 12] where, $\frac{\Delta R_L}{\Delta R_{NL}} = 2$ at $L_S \gg L$. A large deviation than the theoretical factor 2 also have been experimentally demonstrated in FM/SC [13] and FM/metal [14, 15] hybrid structures. Typical effect involves with such deviation are drift electric field [16], anisotropic magnetoresistance (AMR) [17], local Hall effect (LHE) [18] or spatial distribution of device geometry [19]. Here, due to separation between spin polarized charge current path and non-local voltage probe, neither AMR nor LHE can contribute to the deviation from NLSV measurement. Also similar spin diffusion length in LSV and NLSV measurements as mentioned early implies insignificant influence drift electric field in local channel as well. We have not measured magnetoresistance of FM electrode independently but the AMR effect of FM electrodes may have contribution to the LSV amplitude which might makes the large deviation. Also we have considered one dimensional diffusion model but in realistic case two dimensional spatial spin diffusion can become influencing factor in the LSV and NLSV measurement simultaneously [19]. However, the extracted spin diffusion length and injection efficiency are similar to FM/narrow gap semiconductor [10, 20] hybrid structures.

Table 3.4 Extracted parameters at certain spin diffusion length

Parameter	NLSV FM-NM input	NLSV FM-FM input	LSV FM-FM input
L_s [μm]	10		
ΔR_0 [Ω]	0.012	0.024	0.055
η [%]	1.6		
α	1.0	2.0	4.7

On the other hand at 300 K, we could clearly see LSV signal but we could not see NLSV signal. Figure 3.22 (a) and (b) shows LSV and NLSV signal respectively. The reason why we could not see the NLSV seems related to very small (~6mT) difference of magnetization switching between two different size FM electrodes as shown in Fig. 3.23 (a) and (b).

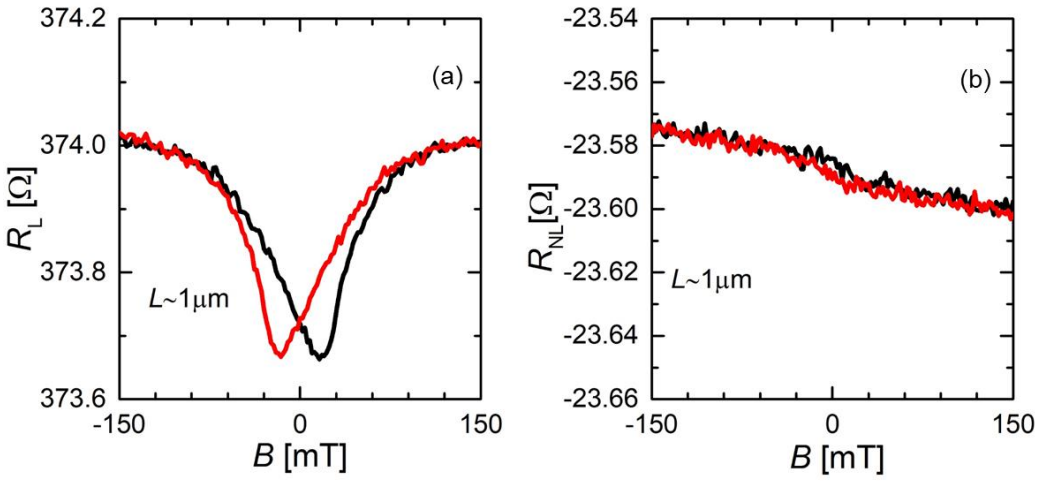

Fig. 3.22 Hysteresis curves of (a) LSV and (b) NLSV at 300 K.

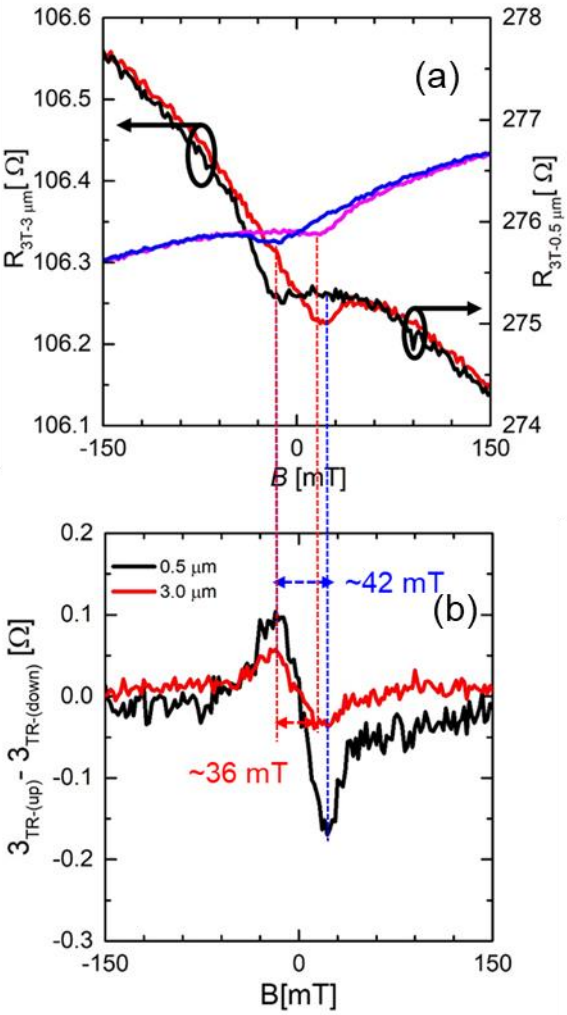

Figure. 5.23 (a) 3T resistances (R_{3T}) for 0.5 μm and 3 μm FM electrodes show almost similar magnetization behavior (b) It seems that 0.5 μm and 3 μm have ~6 mT difference in their hysteresis.

However, assuming similar enhancement factor (4.7 at 1.5 K), we extracted spin diffusion length and injection efficiency at 300 K for LSV signal using the following equation.

$$\Delta R_0 = 4.7 \frac{\eta^2 \rho_S L_S}{W} \left(\frac{-L}{L_S} \right) \quad (3.4)$$

The extracted spin diffusion length ~2.6 µm, sheet resistance ρ_S~180 Ω/sq. similar to 1.5 K condition and hence extracted spin injection efficiency ~6.3%. It is surprising that the injection efficiency is higher at~300 K compared to 1.5 K spin valve measurement. Figure 3.24 shows the comparison of spacing dependence curves of LSV signals.

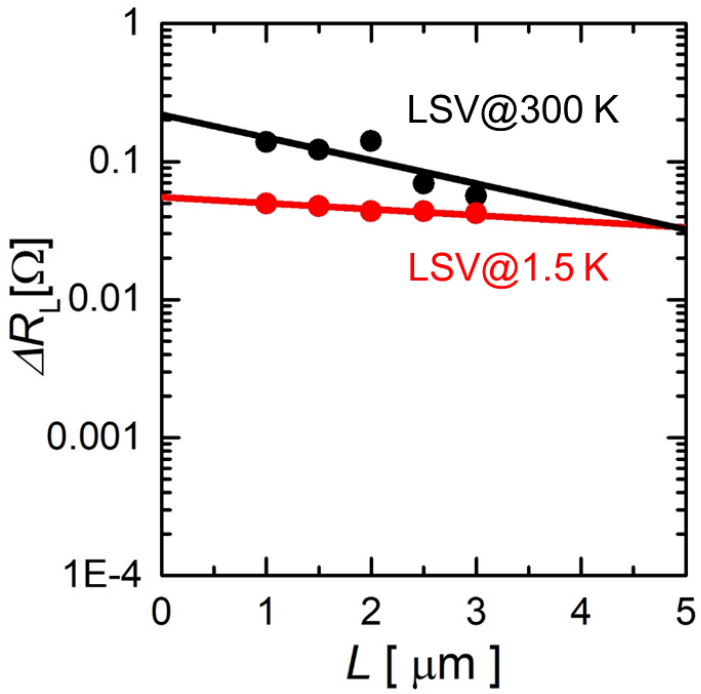

Fig. 3.24 Spacing dependence LSV signal amplitude comparison at 1.5 K and 300K.

To reveal the injection efficiency enhancement at 300 K, we simply compare the sheet resistance of InAs and MnAs at two different temperature for impedance matching. In our measurement, we find constant sheet resistance ~180 Ω/sq. of InAs in the device at 1.5 K and 300 K but we see varied sheet resistance of MnAs at temperature dependent sheet resistivity measurement of MnAs(~50 nm)/InAs(~200 nm)/GaAs(111)B as shown in Fig.3.25,

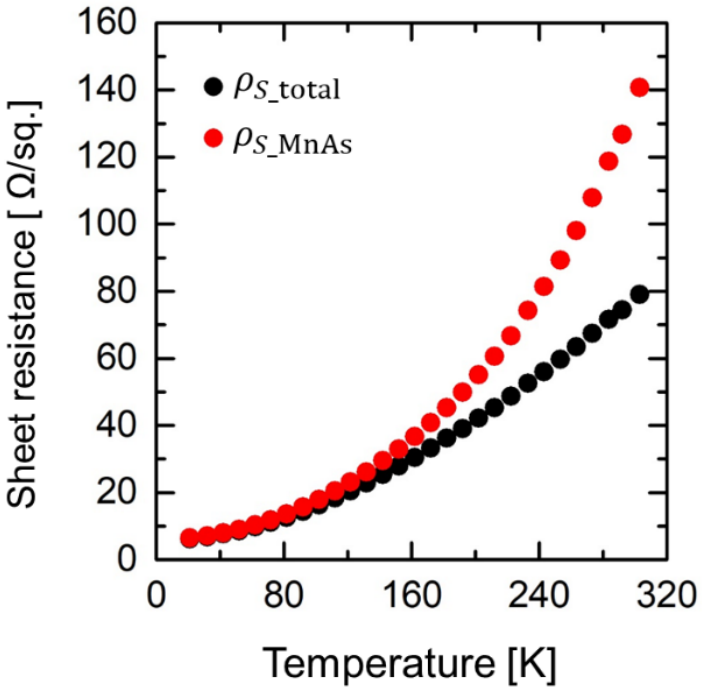

Fig. 3.25 Sheet resistivity measurement of MnAs(~50 nm)/InAs(~200 nm)/GaAs(111)B.

We separated MnAs sheet resistance using the following basic equation,

$$\frac{1}{\rho_{S\_total}} = \frac{1}{\rho_{S\_MnAs}} + \frac{1}{\rho_S} \quad (3.5)$$

Using this relation we find MnAs sheet resistance (ρ_{S_MnAs}) ~6 Ω/sq. and ~140 Ω/sq. at 20 K and 300 K respectively. Therefore, in comparison, the sheet resistances of MnAs at 300 K better impedance matching with that of InAs ~180 Ω/sq. result in high injection efficiency at 300 K rather than 1.5 K.

3.4 Conclusion

We found isotropic Ohmic behavior between MnAs and InAs, and the best sheet resistance and specific contact resistance in the low-temperature grown samples. ρ_c of MnAs/InAs interface at room temperature is ~ (10^{-5}-10^{-4}) Ω-cm^2 which is higher than typical Ohmic contact. Also we tried to fabricate and characterize lateral spin valve devices. We studied trials of lateral spin device of GaAs (1, 3) nm grown samples in lateral spin valve device application. Through the study, we improved device processing and carried out lateral spin valve measurement using AC lock in technique. We successfully confirmed spin injection and detection through simultaneous LSV and NLSV measurements in lateral spin valve device of 1 nm GaAs insertion sample at 1.5 K. We obtained large spin diffusion length ~10 μm and spin injection efficiency ~1.6%. However, ~2.0 time enhancement of NLSV signal can be seen in FM-FM input case than that of FM-NM input case. On the other hand, at 300 K, the extracted spin diffusion length ~2.6 μm and spin injection efficiency ~6.3%. The enhancement of spin injection efficiency is due to better impedance matching between MnAs/InAs at 300 K rather than at 1.5 K.

References

[1]. E.H Phoderick, IEEE Proc. **129** (1982) 1.

[2]. K. Sugiura *et al.,* Appl. Phys. Lett. **89** (2006) 072110.

[3]. http://www.matprop.ru/InAs_basic

[4]. M. Noguchi *et al.,* Phys. Rev. Lett. **66** (1991) 2243.

[5]. G. K. Reeves and H. B. Harrison, IEEE Electron Device Lett. **3** (1982) 111.

[6]. A.G Baca *et al.,* Thin Solid Films **308** (1997) 599.

[7]. T. Kimura et al., Appl. Phys. Lett. 85 (2004) 5382.

[8]. H. Idzuchi et al., Sci. Rep. 628 (2012) 1.

[9]. H. Idzuchi et al., Appl. Phys. Lett. 103 (2013) 162403.

[10]. S. Hidaka et al., Appl. Phys. Express 5 (2012) 113001.

[11]. F. J. Jedema et al., Nature 416 (2002) 713.

[12]. A. Fert, and S. F. Lee, Phys. Rev. B 53, 6554 (1996).

[13]. P. Bruski et al., Appl. Phys. Lett. 103 (2013) 052406.

[14]. F. J. Jedema et al., Phys. Rev. B 67 (2003) 085319.

[15]. T. Kimura et al., Appl. Phys. Lett. 85 (2004) 3501.

[16]. I. Appelbaum et al., Nature 447 (2007) 295.

[17]. M. Shiraishi, and T. Ikoma, Physica E 43 (2011) 1295.

[18]. T. Last et al., J. Supercond. Nov. Magn. 18 (2005) 385.

[19]. T. Kimura et al., Appl. Phys. Lett. 85 (2004) 3501.

[20]. H. C. Koo et al., Appl. Phys. Lett. 90 (2007) 022101.

Chapter 4

Summary and future prospect

In spintronics, electron spin is used as information carrier in addition to its charge. It is already well established metal-based spin-devices practical applications. To use spin degree of freedom into semiconductor spintronic device technology such as in spin field effect transistor (spin-FET), there are three main technological challenges are, firstly, injection of spin polarized carrier from a ferromagnetic (FM) into semiconductor (SC) channel and detection by FM, secondly, SC channel should have strong spin-orbit coupling (SOC) to precess spin during transport through SC channel, and finally, control of the spin precession by gate electric field to modulate spin signal. Therefore, exploring promising FM/SC hybrid structures are important. Here, we synthesized MnAs/III-As hybrid structures on GaAs(111)B as a candidate for future spin-FET and investigated the first challenging issue into the hybrid structures. Now I will discuss the findings.

We carried out successful molecular beam epitaxial (MBE) growth of MnAs(~5-200 nm)/GaAs(~0-10 nm)/thick-InAs(~200-1200 nm) /GaAs(111)B hybrid structures at low temperature MnAs epitaxial growth. We see double step lattice transition ~4 nm of InAs from GaAs surface and abrupt lattice transition of GaAs ~3.6 nm from InAs lattice respectively in RHEED study. The origin of these transition is still unclear for such lattice mismatch growth. In 2θ x-ray diffraction (XRD) measurement, we see single phase epitaxial growth of hexagonal MnAs with cubic InAs and GaAs. Also, the extracted lattice parameters are consistent with their bulk values which imply that the grown epitaxial layers are strain relaxed. To check deviation of c-axis, we carried out thickness dependent ω scanning. From ω and 2θ measurement, we also observed less deviation (InAs ~0.12° and MnAs~0.22°) of c-axis normal

to the planes of thicker MnAs(200 nm) and InAs(1200 nm) layers. Hence, the 2θ and ω scanning indicates good epitaxial growth of MnAs and InAs. We also see reduction of estimated thickness dependence threading dislocation density from the ω-θ broadening with increasing grown layer thickness following pair annihilation mechanism. It means better crystal quality in thicker case. We also see that GaAs and InAs show 3-fold, and MnAs shows 6-fold rotational symmetry which implies good stacking of MnAs and InAs on GaAs(111)B.

In Hall effect measurements, the low temperature grown MnAs sample shows better basic electrical properties than HT sample. The p-type conduction of MnAs hided the n-type conduction of underneath InAs layer. Besides, we also confirmed smooth surface and maze-like magnetic structures on the low-temperature grown samples by AFM and MFM measurements. By SQUID magnetometry measurement, the MnAs/III-As/GaAs(111)B grown sample shows strong magnetic anisotropy along [-2110] and [0-110] lateral and [0001] out of plane directions. It shows easy and isotropic magnetization in lateral directions. The MnAs isotropic behavior almost similar to MnAs directly on GaAs(111)B. We see higher MnAs thickness higher saturation magnetization in lateral directions which seems related to crystal quality. In lateral directions, it shows over room temperature magnetism (estimated Curie temperature ~320-324 K). Over room temperature T_c value and isotropic magnetic behaviors in lateral directions gives a good choice of MnAs for lateral spintronic device design on GaAs(111)B. Therefore, we believe that the MnAs/InAs/GaAs(111)B can be a base structure for future spin-FETs.

To evaluate contact between MnAs/InAs on GaAs(111)B, we carried out transmission line model (TLM) device processing by photolithography and H_3PO_4 based wet chemical etching technique. The electrode width and length were ~180 μm and ~90 μm respectively. In TLM study, we found isotropic Ohmic behavior between MnAs and InAs as expected, and the best sheet resistance and specific contact resistance in the low-temperature grown samples. We

found isotropic Ohmic behaviors in lateral directions of cubic InAs. Specific contact resistance, of MnAs/InAs interface at room temperature is ~(10^{-5}-10^{-4}) Ω-cm^2 which is little higher than typical Ohmic contact. However, over room temperature (~300 K) isotropic magnetic behavior and isotropic electric behaviors in lateral directions gives good flexibility to design lateral spintronic device.

We studied trials of lateral spin valve device of MnAs (~50 nm)/GaAs (~1, 3)/InAs (~200 nm)/GaAs(111)B grown samples in lateral spin valve device application. Through the study, we improved device processing and carried out lateral spin valve measurement using AC lock in technique. We successfully confirmed spin injection and detection through simultaneous LSV and NLSV measurements in lateral spin valve device of 1 nm GaAs insertion sample at 1.5 K. We obtained large spin diffusion length ~10 μm and spin injection efficiency ~1.6% which is similar to other FM/narrow gap hybrid structures. However, ~2.0 time enhancement of NLSV signal can also be seen in FM-FM input case than that of FM-NM input case. On the other hand, at 300 K, the extracted spin diffusion length ~2.6 μm and spin injection efficiency ~6.3%. The enhancement of spin injection efficiency at 300 K is due to better impedance matching between MnAs/InAs rather than at 1.5 K.

In conclusion, we can say that large spin injection efficiency ~6.3 % of the hybrid structures is record value at ~300 K which is very promising for future spin-FET application. Further, higher GaAs thickness dependence investigations are necessary to clarify spin injection efficiency more in details as well as other two challenging issues also have to be investigated before approaching spin-FET applications.

Spin-orbit coupling (SOC)

It is a relativistic effect in which spin and orbits are coupled by magnetic energy. Fig. A1.1 (a) shows, electrons moving with velocity $\boldsymbol{v}$ at a distance $\boldsymbol{r}$ from a nucleus having a charge of $+Ze$. In the coordinate system where the electron is stationary, it seems that the nucleus is turning around the electron at the velocity v as shown in Fig. A1.1 (b). The magnetic field created by the motion of the nucleus creates at the position of the electron.

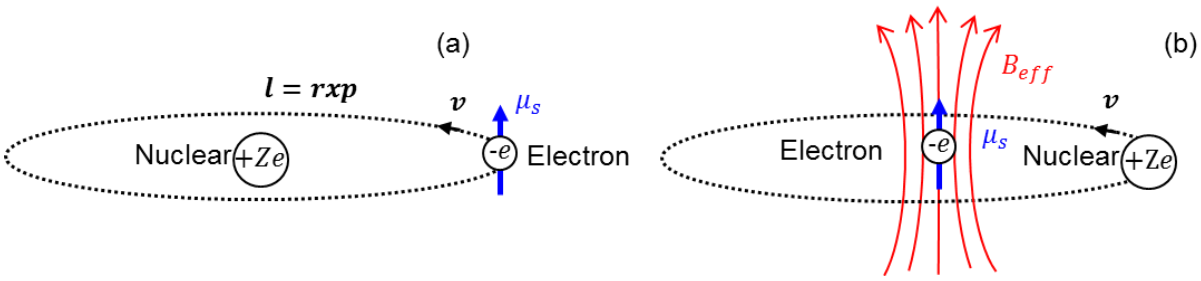

A1.1 (a) Model of spin orbit coupling at atoms (b) Stationary electron and positive charge of the nucleus makes a circular motion, and the spin of the electron feels the effective magnetic field.

Then according to Biot-Savart's law, we can write down the generated magnetic field $\boldsymbol{B}$ as;

$$\boldsymbol{B} = \frac{\mu_0 Ze}{4\pi r^3}\boldsymbol{rxv} = \boldsymbol{B} = \frac{\mu_0 Ze}{4\pi m_0 r^3}\boldsymbol{l} \qquad (A1.1)$$

Angular momentum, $\boldsymbol{L} = \boldsymbol{r} \times \boldsymbol{p}$, m_0 is electron rest mass.

However, electron spin $\boldsymbol{s}$ has magnetic moment $\boldsymbol{\mu}_s$ and they are related by the relation

$$\boldsymbol{\mu}_s = -\frac{2\mu_B}{\hbar}\boldsymbol{s} \qquad (A1.2)$$

Here, $\mu_B = \frac{e\hbar}{2m_0}$ is a Bohr magneton. Now the energy in the magnetic field

$$-\boldsymbol{\mu}_s.\boldsymbol{B} = -\frac{\mu_0 \hbar Z e^2}{4\pi m_0^2 r^3}\boldsymbol{l}.\boldsymbol{s} \qquad \text{(A1.3)}$$

This relation differs from the result by relativistic quantum mechanics by a factor of two, and the energy relation given by the following equation.

$$H_{SO} = -\frac{\mu_0 \hbar Z e^2}{8\pi m_0^2 r^3}\boldsymbol{l}.\boldsymbol{s} \qquad \text{(A1.4)}$$

Now, consider Pauli's spin matrix, $\boldsymbol{\sigma}$ as, $\boldsymbol{s} = (\frac{\hbar}{2})\boldsymbol{\sigma}$, and $\boldsymbol{p} = \hbar\boldsymbol{k}$. Now electric field

$$\boldsymbol{E} = -\nabla\phi = \frac{Ze}{4\pi\epsilon_0 r^3}\boldsymbol{r} \qquad \text{(A1.5)}$$

$\nabla\phi$ is the electrostatic potential gradient. Then using equation (A1.4), finally we can derived,

$$H_{SO} = -\mu_B\boldsymbol{\sigma}.\left(\frac{\hbar\boldsymbol{k} \times \boldsymbol{E}}{2m_0c^2}\right) \qquad \text{(A1.6)}$$

Here, in analogy to Zeeman Hamiltonian $H_z = -\mu_B\boldsymbol{\sigma}.\boldsymbol{B}$ with the Zeeman effect the magnetic field inside the parenthesis, and we can rewrite this into the effective magnetic field B_{eff} and we can write down,

$$\boldsymbol{B}_{eff} = \left(\frac{\hbar\boldsymbol{k} \times \boldsymbol{E}}{2m_0c^2}\right) \qquad \text{(A1.7)}$$

From this, it can be seen that the effective magnetic field is generated in the direction perpendicular to the particle's motion direction. $2m_0c^2$ is energy gap between particle (electron) and antiparticle (positron). This is 1 MeV order for free electron. This energy gap is known as Dirac gap. In a typical semiconductor, this energy gap is a band gap reduced to ~1

eV. The Dirac gap is replaced by the energy-band gap using $\boldsymbol{k}.\boldsymbol{p}$ perturbation theory [1]. It results in six time increase of SOC in semiconductor. More specifically, SOC for group III-V compound semiconductors, we consider an independent p orbital. If we introduce the full-angular momentum, $\boldsymbol{j} = \boldsymbol{l} + \boldsymbol{s}$, we get,

$$\boldsymbol{l}.\boldsymbol{s} = \frac{1}{2}[(\boldsymbol{l}+\boldsymbol{s})^2 - \boldsymbol{l}^2 - \boldsymbol{s}^2] = \frac{1}{2}[(\boldsymbol{j}^2 - \boldsymbol{l}^2 - \boldsymbol{s}^2] \quad \text{(A1.8)}$$

Therefore, H_{so} is commutative to $\boldsymbol{j}^2$, j_z. We know the motion of electrons in a crystalline solid is described by the energy band dispersion, $\boldsymbol{E} - \boldsymbol{k}$ relation. The band structure in the solid is shown in Fig.A1.2. The electron state at valence band edge with orbital angular momentum $\boldsymbol{l}$=1 with SOC included, we get states with $\boldsymbol{j}$ = 3/2 and 1/2, and the latter is called the spin orbital separation band. When the wavenumber is large, the band of $\boldsymbol{j}$ = 3/2 splits into bands of $\boldsymbol{j}_z$ = ±3/2, ±1/2. The wave function in the vicinity of the top end of these valence bands, near the lower end of the conduction band. We call heavy hole (HH) and light hole (LH), respectively, from wave function near the top of the valence band near the lower end of the conduction band SOC is considered to be absent because it consists of constituent atoms' s orbit

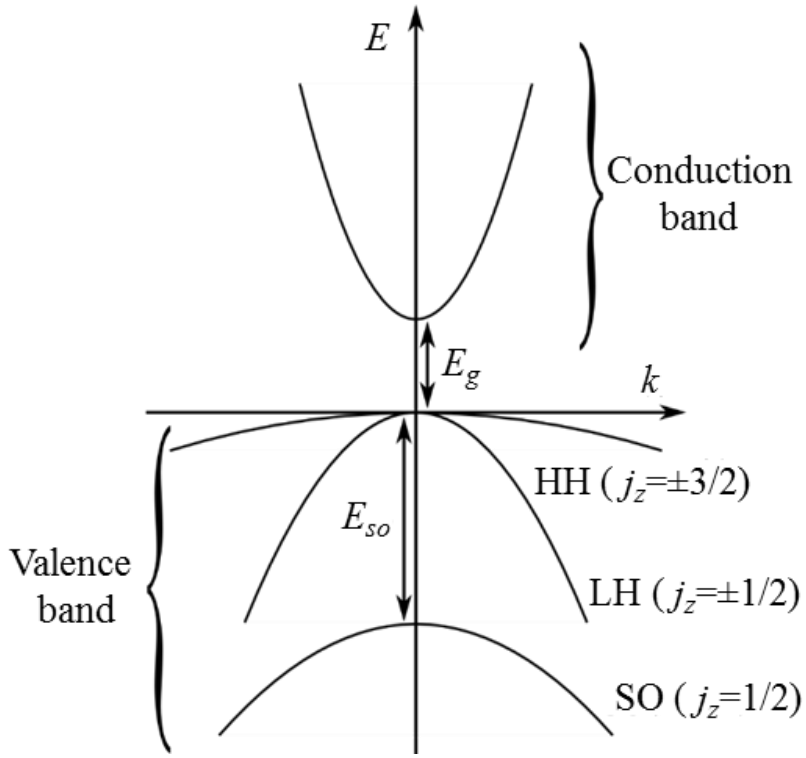

Fig.A1.2 Band structure near Γ point of III-V compound semiconductor

($\boldsymbol{l} = 0$) but in practice SOC contributes greatly to the conduction electrons by hybridization of the orbits between the bands. The wave function of electrons in solid can be written by replacing the mass of electrons with the effective mass in Schrödinger equation. The equation (A1.9) is a band structure near the Γ point of the group III-V compound semiconductor obtained from the **k · p** perturbation as [2],

$$H_{so} = \frac{P^2}{3}\left[\frac{1}{E_g^2} - \frac{1}{(E_g + E_{so})^2}\right]\frac{1}{\hbar}\boldsymbol{\sigma}.(\boldsymbol{p} \times \boldsymbol{\nabla}\phi) \qquad \text{(A1.9)}$$

P is the matrix element between the conduction band and the valence band, E_g is the band gap, E_{so} is the energy difference between j = 3/2 and j = 1/2 in the valence band. From equation (A1.9), we see the narrower the band gap the higher the SOC. Now, we briefly introduced about two fundamental Rashba and Dresslhaus type SOC. Rashba type SOC associated 2-dimesional electron gas (2DEG) system for example in narrow gap III-V (for example InAs,

InGaAs, InGaSb) semiconductor hybrid structure. Because in 2DEG system electrons are conducted at high speed in an electric field caused by the structure inversion asymmetry (SIA) property of 2DEG system which makes asymmetric potential distribution in the direction perpendicular to the 2D plane and conduction band degeneracy take place [3, 4]. There are reports from various aspects such as magnetic field dependence, origin, size of SOC in narrow gap 2DEG [5-8] system. Considering Rashba term H_R as a perturbation to the Hamiltonian $H^0_{x,y}$ in the x, y direction under zero magnetic field, then the Hamiltonian $H_{x,y}$ of (001) oriented crystal becomes,

$$H_{x,y} = H^0_{x,y} + H_R \quad \text{(A1.10)}$$

$$H^0_{x,y} = \frac{\hbar^2}{m^*}\left(k_x^2 + k_y^2\right) \quad \text{(A1.11)}$$

$$H_R = \alpha\left(\sigma_x k_y - \sigma_y k_x\right) \quad \text{(A1.12)}$$

Thus we obtain energy eigenvalue for $H_{x,y}$ where α is the spin orbital coupling coefficient representing the strength of Rashba SOC. The eigenstate of $H^0_{x,y}$ is $\left|k_x, k_y, \sigma\right\rangle$ can be represented as,

$$\langle k_x, k_y, \sigma_1 \left| H^0_{x,y} \right| k_x, k_y, \sigma_2 \rangle = \frac{\hbar^2 k^2}{2m^*}\delta_{\sigma_1,\sigma_2} \quad \text{(A1.13)}$$

In matrix form that is,

$$H^0_{x,y} = \begin{bmatrix} \frac{\hbar^2 k^2}{2m^*} & 0 \\ 0 & \frac{\hbar^2 k^2}{2m^*} \end{bmatrix} \quad \text{(A1.14)}$$

Then using equation (A1.12), H_R becomes,

$$H_R = \alpha(\sigma_x k_y - \sigma_y k_x)$$

$$H_R = \alpha k_y \begin{bmatrix} 0 & 1 \\ 1 & 0 \end{bmatrix} - \alpha k_x \begin{bmatrix} 0 & -i \\ i & 0 \end{bmatrix}$$

$$or, H_R = \alpha \begin{bmatrix} 0 & k_y + ik_x \\ k_y - ik_x & 0 \end{bmatrix} \quad \text{(A1.15)}$$

Now,

$$H_{x,y} = H^0_{x,y} + H_R$$

$$\begin{bmatrix} \frac{\hbar^2 k^2}{2m^*} & 0 \\ 0 & \frac{\hbar^2 k^2}{2m^*} \end{bmatrix} + \alpha \begin{bmatrix} 0 & k_y + ik_x \\ k_y - ik_x & 0 \end{bmatrix}$$

$$or, H_{x,y} = \begin{bmatrix} \frac{\hbar^2 k^2}{2m^*} & \alpha(k_y + ik_x) \\ \alpha(k_y - ik_x) & \frac{\hbar^2 k^2}{2m^*} \end{bmatrix} \quad \text{(A1.16)}$$

Then energy eigenvalue E_R can be obtained using (A1.16),

$$(\frac{\hbar^2 k^2}{2m^*} - E_R)^2 - \alpha^2 (k_y + ik_x)(k_y - ik_x) = 0$$

$$or, (\frac{\hbar^2 k^2}{2m^*} - E_R)^2 - \alpha^2 k^2 = 0$$

$$or, E_R = \frac{\hbar^2 k^2}{2m^*} \pm \alpha k \quad \text{(A1.17)}$$

Therefore, dispersion relation at zero magnetic field,

$$E_{R\uparrow,\downarrow} = \frac{\hbar^2 k^2}{2m^*} \pm \alpha k \uparrow,\downarrow \quad \text{(A1.18)}$$

It can be seen that spin is split energetically with respect to finite k. Also, its spin splitting energy is ΔE_R,

$$\Delta E_R = 2\alpha k_F \quad \text{(A1.19)}$$

Where, k_F is the Fermi wavenumber. Now comparing equation (A1.19) with the Zeeman $\Delta E_Z = g^* \mu_B \boldsymbol{B}$ separation energy. We get,

$$\left|B_{eff(R)}\right| = \frac{2|\alpha| k_F}{|g^*| \mu_B} \quad \text{(A1.20)}$$

The effective magnetic field $B_{eff(R)}$ due to the Rashba SOC is determined. Figure A1.3 shows the Fermi circle by Rashba SOC and the direction of the effective magnetic field.

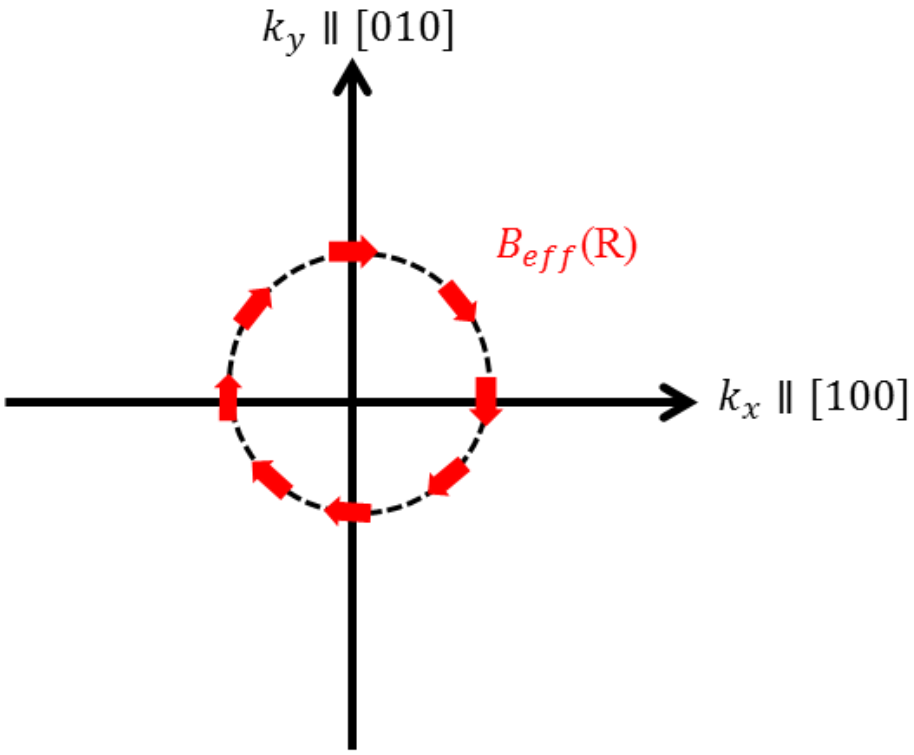

Fig.A1.3 Fermi circle and direction of effective magnetic field at Rashba SOC.

On the other hand, Dresslhaus type SOC also induced in compound semiconductors with zinc-blend structure from the bulk inversion asymmetry (BIA) property of the crystal structure. All of [100], [111] crystal orientation have been exhibited Dresslhaus SOC which is proportional to k^3 in the k space [9]. Let us consider the Dresselhaus term H_D as a perturbation to the Hamiltonian $H_{x,y}^0$ in the x, y direction under zero magnetic field of (001) oriented crystal becomes,

$$H_{x,y} = H_{x,y}^0 + H_D \quad \text{(A1.21)}$$

$$H_{x,y}^0 = \frac{\hbar^2}{m^*}\left(k_x^2 + k_y^2\right) \quad \text{(A1.22)}$$

$$H_D = H_{D1} + H_{D3} = \beta_1\left(\sigma_y k_y - \sigma_x k_x\right) + \gamma\left(-\sigma_y k_y k_x^2 + \sigma_x k_x k_y^2\right) \quad \text{(A1.23)}$$

Here,$\beta_1 = \gamma\langle k_Z^2\rangle$ and in equation (A1.23) the first term is proportional to k so it is called a linear term and the second term is proportional to k^3 so it is called a Cubic term. β_1 is a strong Dresslhaus SOC coefficient. Since k_Z depends on the expansion of wave function. We can control β_1 by changing the width of the quantum well but γ is a parameter peculiar to a material. The precision of γ determines β_1. Thus we obtain energy eigenvalue for $H_{x,y}$. The eigenstate of $H_{x,y}^0$ is $\left|k_x, k_y, \sigma\right\rangle$ can represent as,

$$\langle k_x, k_y, \sigma_1 \left| H_{x,y}^0 \right| k_x, k_y, \sigma_2\rangle = \frac{\hbar^2 k^2}{2m^*}\delta_{\sigma_1,\sigma_2} \quad \text{(A1.24)}$$

Then,

$$H_{x,y}^0 = \begin{bmatrix} \frac{\hbar^2 k^2}{2m^*} & 0 \\ 0 & \frac{\hbar^2 k^2}{2m^*} \end{bmatrix} \quad \text{(A1.25)}$$

Appendix-A1

The Hamiltonian H_{D1} of the linear term in Dresslhaus SOC is,

$$H_{D1} = \beta_1(\sigma_x k_y - \sigma_y k_x) \quad \text{(A1.26)}$$

$$or, H_{D1} = \beta_1 k_y \begin{bmatrix} 0 & 1 \\ 1 & 0 \end{bmatrix} - \beta_1 k_x \begin{bmatrix} 0 & -i \\ i & 0 \end{bmatrix}$$

$$or, H_{D1} = \beta_1 \begin{bmatrix} 0 & k_y + ik_x \\ k_y - ik_x & 0 \end{bmatrix} \quad \text{(A1.27)}$$

Using equation (A1.25) and (A1.27), equation (A1.21) becomes,

$$H_{x,y} = H^0_{x,y} + H_D$$

$$or, H_{x,y} = \begin{bmatrix} \frac{\hbar^2 k^2}{2m^*} & 0 \\ 0 & \frac{\hbar^2 k^2}{2m^*} \end{bmatrix} + \beta_1 \begin{bmatrix} 0 & k_y + ik_x \\ ik_y - k_x & 0 \end{bmatrix}$$

$$or, H_{x,y} = \begin{bmatrix} \frac{\hbar^2 k^2}{2m^*} & \beta_1(k_y + ik_x) \\ \beta_1(ik_y - k_x) & \frac{\hbar^2 k^2}{2m^*} \end{bmatrix} \quad \text{(A1.28)}$$

Then energy eigenvalue E_{D1} can be obtained using (A1.28),

$$(\frac{\hbar^2 k^2}{2m^*} - E_{D1})^2 - \beta_1^2(ik_y - k_x)(k_y + ik_x) = 0$$

$$or, (\frac{\hbar^2 k^2}{2m^*} - E_{D1})^2 - \beta_1^2 k^2 = 0$$

$$or, E_{D1} = \frac{\hbar^2 k^2}{2m^*} \pm \beta_1 k \quad \text{(A1.29)}$$

Therefore, dispersion relation at zero magnetic field,

$$E_{D1\uparrow,\downarrow} = \frac{\hbar^2 k^2}{2m^*} \pm \beta_1 k \uparrow,\downarrow \quad \text{(A1.30)}$$

The spin splitting energy is ΔE_{D1},

$$\Delta E_{D1} = 2\beta_1 k_F \quad \text{(A1.31)}$$

Now comparing equation (A1.31) with the Zeeman $\Delta E_Z = g^* \mu_B \boldsymbol{B}$ separation energy. We get,

$$\left|B_{eff(D1)}\right| = \frac{2|\beta_1| k_F}{|g^*|\mu_B} \quad \text{(A1.32)}$$

The effective magnetic field $B_{eff(D1)}$ due to Dresslhaus SOC is determined. Figure. A1.4 shows the Fermi circle by the Dresslhaus SOC and the direction of the effective magnetic field in contrast to the Rashba SOC, the effective magnetic field vector $B_{eff(D1)}$ depends on the wave vector k.

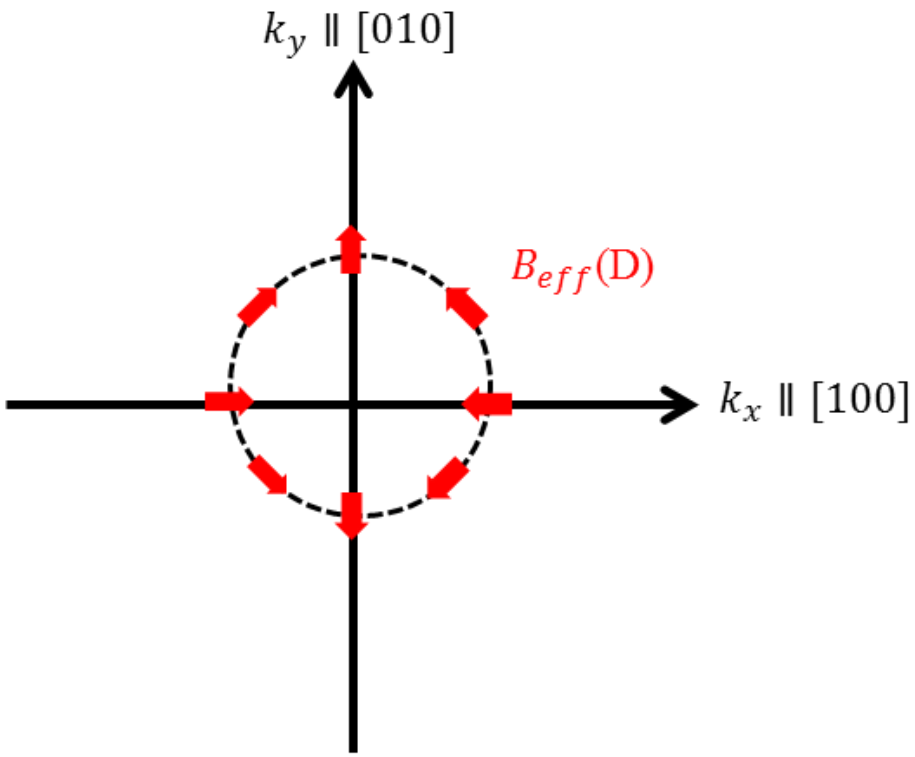

Fig.A1.4 Fermi circle and direction of effective magnetic field at Dresslhaus SOC.

Therefore, choice of suitable FM/SC hybrid structure and understanding about electrically spin injection, controlling spin transport and detection into the hybrid structure are crucial to decide the candidacy of FM/SC for future spin-FET.

References:

[1]. Th. Schäpers *et al.*, J. Appl. Phys. **83** (1998) 4324

[2]. E. O. Kane, J. Phys. Chem. Solids **1** (1957) 249.

[3]. E. Rashba, Soviet Physics-Solid State **2** (1960) 1109.

[4]. Y. Bychkov and E. Rashba, J. Phys. C **17** (1984) 6039.

[5]. G. Lommer *et al.,* Phys. Rev. Lett. **60** (1988) 728.

[6]. P. Pfeffer and W. Zawadzki, Phys. Rev. B **52** (1995) R14332.

[7]. Y. S. Gui *et al.,* Phys. Rev. B **61** (2000) 7237.

[8]. M. Akabori *et al.*, Physica. E, low dimensional systems and nanostructures **34** (2006) 413.

[9]. G. Dresselhaus, Phys. Rev. **100** (1995) 580.

X-ray diffraction (XRD) for structural analysis

Atomic structure of crystalline solids usually examined by x-ray diffraction techniques. X-ray radiation has wavelengths in the range of 0.1 to 10 Å. We consider x-ray interference effects with crystal lattice. The diffraction condition first established by Bragg. He studied with a monochromatic x-ray beam having coherent radiation incident on a crystal as represented in Fig.A2.1. Moreover, atoms which constitute the actual diffraction centers are sets of parallel planes reflect x-rays. The spacing of these planes, d having miller indices (hkl) is connected with lattice constant(a); In a cubic crystal,

$$d_{(hkl)} = \frac{a}{\sqrt{h^2 + k^2 + l^2}} \quad \text{(A2.1)}$$

and for hexagonal unit cell d having miller indices (hkl) is connected to lattice constant(c);

$$d_{(hkl)} = \sqrt{\frac{3}{4}} \frac{a}{\sqrt{h^2 + hk + k^2}} + \frac{c}{l} \quad \text{(A2.2)}$$

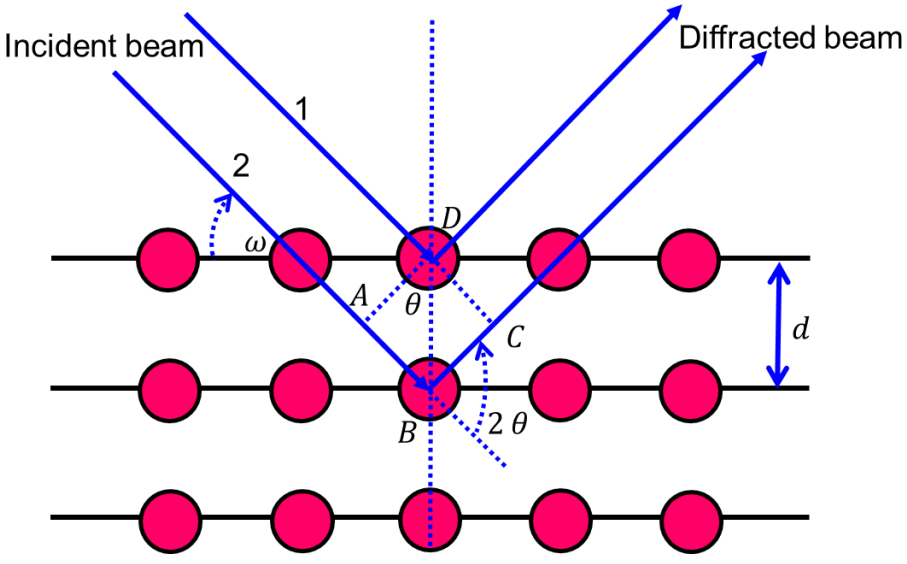

Fig.A2.1 Bragg diffraction: two beams with identical wavelength and phase approach a crystalline solid and are scattered off two different atoms within it.

Appendix-A2

We can find diffraction peak at constructive interference of diffracted beams from successive planes. Therefore, it is necessary to have in phase of the diffracted beams after leaving crystal surface. We labeled beams 1 and 2 in Fig.A2.1. The path difference between the two beams $(AB + BC)$ be equal to an integral number (n) of wavelengths (λ) of the indicent radiation.

$$AB + BC = n\lambda \quad \text{(A2.3)}$$

$$\text{Since } AB = BC \text{ and } \sin\theta = \frac{AB}{d_{(hkl)}}$$

Therefore, AB=$d_{(hkl)}\sin\theta$; then from equation (A2.3) can be written as;

$$n\lambda = 2d\sin\theta \quad \text{(A2.4)}$$

This is known as Bragg's law. It demonstrates angular relation of diffracted beam with λ and $d(hkl)$. For first order diffraction (n = 1) Bragg's law becomes;

$$\lambda = 2d\sin\theta \quad \text{(A2.5)}$$

At diffraction condition, the incident angle, ω is equal to diffracted angle θ which meets the relation, $\lambda = 2d\ sin\ \theta$. The diffraction experiment provides quantitative data on lattice constant and shape characteristics of simple cubic, body centered cubic and face centered cubic unit cell. However, Bragg's law treats size and shape of unit cell not with atom positions. Diffraction peaks selection rules for cubic system are given in table A2.1

Table A2.1: Diffraction peaks selection rules for cubic system

Bravais Lattice	Peak present	Peak absent
Simple cubic	Every	None
Body center cubic	$h+k+l$ = even	$h+k+l$= odd
Face center cubic	h,k,l unmixed (either all even or all odd)	h,k,l mixed

Figure.A2.2 shows basic setup up and relationship of x-ray diffraction measurement. Here, ω angle between incident x-rays and sample surface, 2θ angle between incident x-rays and detector, ψ Sample tilt, φ lateral direction of sample and Z vertical displacement of sample.

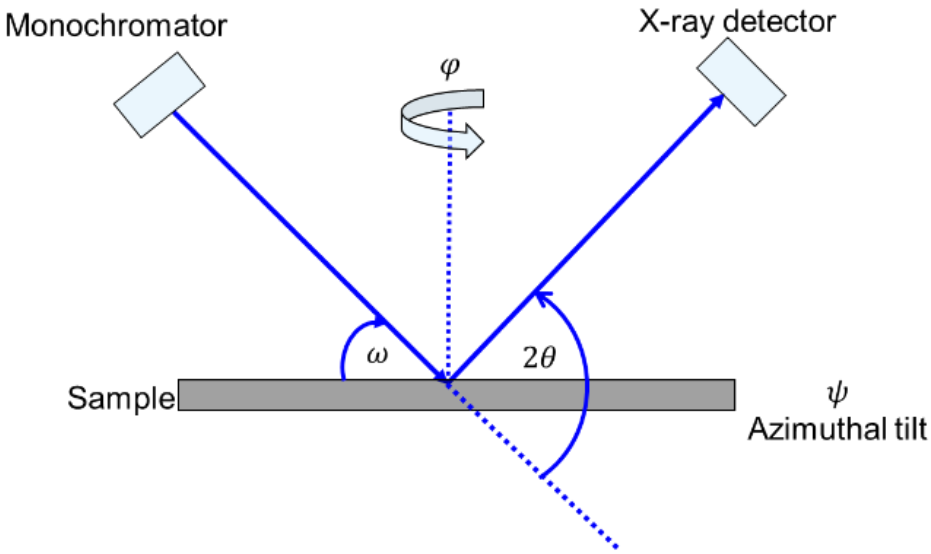

Fig.A2.2 X-ray diffraction measurement setup.

Transmission coefficient through a tunnel barrier

Consider a potential barrier with barrier height qV_0 as shown in the figure below. We will consider transmission coefficient of a particle (i.e electron) through this barrier having thickness, t in x direction.

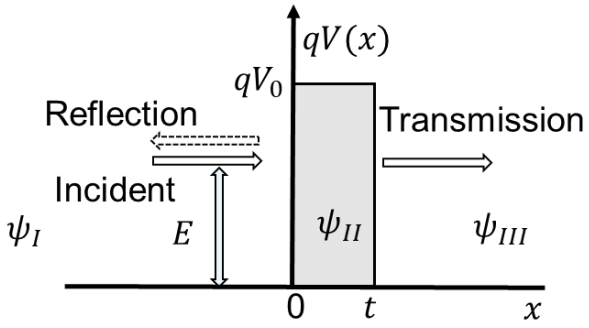

Fig.A3.1 Schematic of one dimensional potential barrier.

In classical mechanics, the electron will be reflected completely if its energy E is smaller than the barrier height. However, in quantum mechanics, the electron has a finite probability to transmit or tunnel through the potential barrier. So the behavior of the electron in outside the barrier is free i.e $qV_0(x) = 0$ can be described by Schrödinger equation;

$$\frac{\hbar^2}{2m_n}\frac{d^2\psi}{dx^2} = -E\psi \quad \text{(A3.1)}$$

Where, m_n is effective mass, $\hbar$ is the reduced Planck constant, E is the kinetic energy, and ψ is the wave function of the electron. Equation (A3.1) can be written in the form,

$$\frac{d^2\psi}{dx^2} = -\frac{2m_n}{\hbar^2}E\psi$$

$$or, \frac{d^2\psi}{dx^2} + k^2\psi = 0 \quad \text{(A3.2)}$$

$$\text{Where, } k = \sqrt{\frac{2m_n E}{\hbar^2}}$$

The equation (A3.2) for region (I) and (III) becomes

$$\frac{d^2\psi_I}{dx^2} + k^2\psi_I = 0 \quad \text{(A3.3)}$$

$$\frac{d^2\psi_{III}}{dx^2} + k^2\psi_{III} = 0 \quad \text{(A3.4)}$$

Equation (A3.3) and (A3.4) are homogeneous second order deferential equation. First, to find general solution of (A3.3), we consider,

$$\psi_I = e^{mx}$$

$$or, \frac{d\psi_I}{dx} = me^{mx}$$

$$or, \quad \frac{d^2\psi_I}{dx^2} = m^2e^{mx}$$

Using these values in equation (A3.3), the auxiliary equation is found to be

$$m^2e^{mx} + k^2e^{mx} = 0$$

$$\text{But, } e^{mx} \neq 0$$

then,

$$m^2 + k^2 = 0$$

$$\text{Or, } m = \pm jk$$

Hence, the general solution of equation (A3.3) at $x \leq 0$, is in the form,

$$\psi_I(x) = Ae^{jkx} + Be^{-jkx} \text{ (A3.5)}$$

Similarly way, the solution of equation (A3.4) is in the form

$$\psi_{III}(x) = Ce^{jkx} + De^{-jkx} \text{ (A3.6)}$$

But, at $x \geq t$, we have only transmitted wave function, so reflected wave amplitude in region (III) is zero, then equation (A3.6) can be of the form,

$$\psi_{III}(x) = Ce^{jkx} \text{ (A3.7)}$$

However, consider, the finite barrier height of the potential barrier at, $qV_0 > E$, the Schrödinger equation in region II becomes;

$$\frac{d^2\psi_{II}}{dx^2} = \frac{2m_n}{\hbar^2}(qV_0 - E)\psi_{II} \quad \text{(A3.8)}$$

$$or, \frac{d^2\psi_{II}}{dx^2} = \beta^2\psi_{II}$$

$$\frac{d^2\psi_{II}}{dx^2} - \beta^2\psi_{II} = 0 \quad \text{(A3.9)}$$

Where, $\beta = \sqrt{\frac{2m_n(qV_0-E)}{\hbar^2}}$

The solution of equation (A3.9) can be written of the form,

$$\psi_{II}(x) = Fe^{\beta x} + Ge^{-\beta x} \quad \text{(A3.10)}$$

The continuity of ψ and $\frac{d\psi}{dx}$ at $x = 0$ and $x = d$ which is required by the boundary conditions, provides four relations between the coefficient, A, B, C, F, G. To get transmission coefficient,

We can write at $x = 0$,

$$\psi_I(0) = \psi_{II}(0)$$

Appendix-A3

$$\frac{d\psi_I(0)}{dx} = \frac{d\psi_{II}(0)}{dx}$$

Hence, using these relations, we can write down from equation (A3.5) and (10) at $x = 0$

$$A + B = F + G \quad \text{(A3.11)}$$

$$Ajk - Bjk = F\beta - G\beta \quad \text{(A3.12)}$$

Multiplying equation (A3.11) by jk and add with equation (A3.12) and simplified, we get,

$$A = \frac{[F(jk + \beta) + G(jk - \beta)]}{2jk} \quad \text{(A3.13)}$$

At $x = t$

$$\psi_{II}(t) = \psi_{III}(t)$$

$$Fe^{\beta t} + G\beta e^{-\beta t} = Cjke^{jkt} \text{ (A3.14)}$$

$$\frac{d\psi_{II}(t)}{dx} = \frac{d\psi_{III}(t)}{dx}$$

$$or, F\beta e^{\beta t} - G\beta e^{-\beta t} = Cjke^{jkt} \text{ (A3.15)}$$

Multiplying equation (A3.14) by β and adding with equation (A3.15), we can write down,

$$F = \frac{\left[C(jk + \beta)e^{jkt}\right]}{2\beta e^{\beta t}} \quad \text{(A3.16)}$$

Again multiplying equation (A3.14) by β and subtracting equation (A3.15), we can write down,

$$G = \frac{\left[C(\beta - jk)e^{jkt}\right]}{2\beta e^{-\beta t}} \quad \text{(A3.17)}$$

Putting the value of F and G in equation (A3.13), we get,

$$A = \frac{\left[\frac{[C(jk+\ \beta)e^{jkt}]}{2\beta e^{\beta t}}(jk+\beta) + \frac{[C(\ \beta - jk)e^{jkt}]}{2\beta e^{-\beta t}}(jk-\beta)\right]}{2jk}$$

$$or, A = \frac{C(jk+\ \beta)e^{jkt}(jk+\beta)}{4jk\beta e^{\beta t}} + \frac{C(\ \beta - jk)e^{jkt}(jk-\beta)}{4jk\beta e^{-\beta t}}$$

$$or, A = Ce^{jkt}\left[\frac{(jk+\ \beta)(jk+\beta)}{4jk\beta e^{\beta t}} + \frac{(\ \beta - jk)(jk-\beta)}{4jk\beta e^{-\beta t}}\right]$$

$$or, A = \frac{Ce^{jkt}}{4jk\beta}\left[(jk+\ \beta)^2 e^{-\beta t} - (jk-\ \beta)^2 e^{\beta t}\right]$$

$$or, A = \frac{Ce^{jkt}}{4jk\beta}\left[(\beta^2 - k^2)e^{-\beta t} + 2jk\beta e^{-\beta t} - (\beta^2 - k^2)e^{\beta t} + 2jk\beta e^{\beta t}\right]$$

$$or, A = \frac{Ce^{jkt}}{4jk\beta}\left[(\beta^2 - k^2)e^{-\beta t} - (\beta^2 - k^2)e^{\beta t} + 2jk\beta e^{-\beta t} + 2jk\beta e^{\beta t}\right] \text{ (A3.18)}$$

We can represent (A3.18) in terms $\sinh(x)$ function, we can define it as

$$sinh(x) = (e^{-x} - e^{x})/2$$

$$cosh(x) = (e^{-x} + e^{x})/2$$

Using these relations we can represent equation (A3.18) as follows,

$$A/C = \frac{e^{jkt}}{4jk\beta}[2(\beta^2 - k^2)sinh^2\beta t + 4jk\beta cosh^2\beta t] \text{ (A3.19)}$$

The complex quantity of equation (A3.19) can be obtained, $j = -j$,

$$A^*/C^* = \frac{e^{-jkt}}{-4jk\beta}[2(\beta^2 - k^2)sinh^2\beta t - 4jk\beta cosh^2\beta t] \text{ (A3.20)}$$

Multiplying (A3.19) by (A3.20), we get,

$$\frac{A \times A^*}{C \times C^*} = \frac{1}{16k^2\beta^2}[4(\beta^2 - k^2)^2 sinh^2(\beta t) + 16k^2\beta^2 cosh^2(\beta t)] \quad \text{(A3.21)}$$

Using, $cosh^2 x = 1 + sinh^2 x$ relation we can write down the modulus of (A3.21) as follows,

$$\frac{A^2}{C^2} = \frac{1}{16k^2\beta^2}[4(\beta^2 - k^2)^2 sinh^2(\beta t) + 16k^2\beta^2 cosh^2(\beta t)]$$

$$or, \frac{A^2}{C^2} = \frac{1}{16k^2\beta^2}[4(\beta^2 - k^2)^2 sinh^2(\beta t) + 16k^2\beta^2\{1 + sinh^2(\beta t)\}]$$

$$or, \frac{A^2}{C^2} = \frac{1}{16k^2\beta^2}[\{4(\beta^2 - k^2)^2 + 16k^2\beta^2\} sinh^2(\beta t)\} + 16k^2\beta^2]$$

$$or, \frac{C^2}{A^2} = \frac{16k^2\beta^2}{[\{4(\beta^2 - k^2)^2 + 16k^2\beta^2\} sinh^2(\beta t)\} + 16k^2\beta^2]}$$

$$or, \frac{C^2}{A^2} = \frac{1}{[\{4(\beta^2 - k^2)^2 + 16k^2\beta^2\} sinh^2(\beta t)\}/16k^2\beta^2] + 1}$$

$$or, \frac{C^2}{A^2} = \frac{1}{1 + [\{(\beta^2 - k^2)^2 + 4k^2\beta^2\} sinh^2(\beta t)\}/4k^2\beta^2]}$$

$$or, \frac{C^2}{A^2} = \frac{1}{1 + [\{\beta^4 - 2\beta^2k^2 + k^4 + 4k^2\beta^2\} sinh^2(\beta t)\}/4k^2\beta^2]}$$

$$or, \frac{C^2}{A^2} = \frac{1}{1 + [\{\beta^4 + 2\beta^2k^2 + k^4\} sinh^2(\beta t)\}/4k^2\beta^2]}$$

$$or, \frac{C^2}{A^2} = \frac{1}{1 + [\{(\beta^2 + k^2)^2 sinh^2(\beta t)\}/4k^2\beta^2]}$$

$$or, \frac{C^2}{A^2} = \frac{1}{1 + [\frac{\{(\beta^2 + k^2)^2 sinh^2(\beta t)\}}{4k^2\beta^2}]} \quad \text{(A3.22)}$$

Putting the values of $k = \sqrt{\frac{2m_nE}{\hbar^2}}$ and $\beta = \sqrt{\frac{2m_n(qV_0 - E)}{\hbar^2}}$; we get from equation (A3.22),

$$or, \frac{C^2}{A^2} = \frac{1}{1 + [\frac{\{(2m_n(qV_0 - E)/\hbar^2) + (2m_nE/\hbar^2)\}^2 sinh^2(\beta t)}{4\{2m_n(qV_0 - E)/\hbar^2\}(2m_nE/\hbar^2)}]}$$

$$or, \frac{C^2}{A^2} = \frac{1}{1 + [\frac{(2m_nqV_0 - 2m_nE + 2m_nE)^2 sinh^2(\beta t)}{16m_n^2E(qV_0 - E)}]}$$

$$or, \frac{C^2}{A^2} = \frac{1}{1 + [\frac{(2m_nqV_0)^2 sinh^2(\beta t)}{16m_n^2E(qV_0 - E)}]}$$

$$or, \frac{C^2}{A^2} = \frac{1}{1 + [\frac{(qV_0)^2 sinh^2(\beta t)}{4E(qV_0 - E)}]} \quad \text{(A3.23)}$$

This is an expression of transmission coefficient for a one dimensional barrier height qV_0. We consider three different energies of conduction electron (0.1, 0.2, 0.3) eV of a finite potential barrier 0.9 eV with GaAs mass ratio, o.067. We have theoretically calculated transmission coefficient using equation (A3.23) at three different particle energy and varying barrier thickness. Fig.A3.2, shows the barrier thickness dependence transmission coefficient. We see the transmission coefficient decreases monotonically as E decreases. To get a finite transmission coefficient, we require small thickness of tunneling barrier, t, a low potential barrier and a small effective mass.

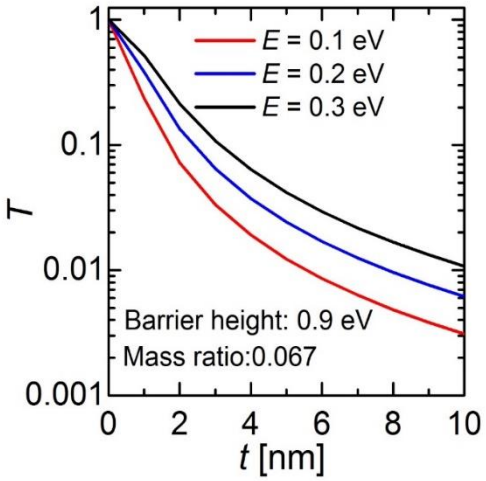

Fig.A3.2 Barrier thickness versus transmission coefficient curve.

However, At, $x \gg 1$, the definition of $sinh(x)$ becomes,

$$sinh(x) = (e^{-x} - e^{x})/2$$

$$or, sinh(x) \approx (-e^{x})/2$$

Hence doing similar manner in equation (A3.23) at $\beta t \gg 1$,

$$\frac{C^2}{A^2} = \frac{1}{[\frac{\{qV_0 sinh(\beta t)\}^2}{4E(qV_0 - E)}]}$$

$$or, \frac{C^2}{A^2} = \frac{1}{[\frac{(-qV_0 e^{\beta t}/2)^2}{4E(qV_0 - E)}]}$$

$$or, \frac{C^2}{A^2} = \frac{1}{[\frac{(-qV_0 e^{\beta t})^2}{16E(qV_0 - E)}]}$$

$$\frac{C^2}{A^2} = \frac{16E(qV_0 - E)}{(qV_0)^2}\, e^{-2\beta t} \quad \text{(A3.24)}$$

This is the approximate form of transmission coefficient.

Transmission line model device (TLM)

This is a method for measuring Ohmic contact resistance in a planar device to evaluate Ohmic contact resistance. Figure A4.1 shows a conceptual diagram of TLM.

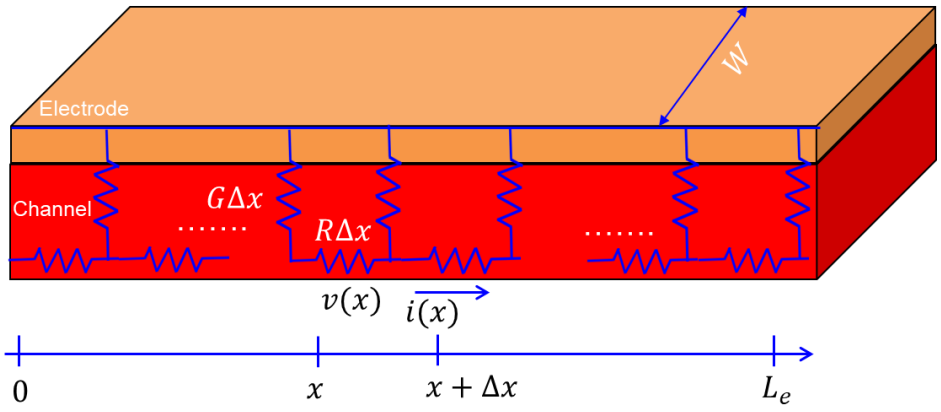

Fig.A4.1 Conceptual diagram of contact in TLM.

The sheet resistance of the device channel layer is ρ_s $\left[\frac{\Omega}{\text{sq}}.\right]$, specific contact resistance between electrode and channel layer is $\rho_c[\,\Omega.cm^2]$, electrode width and channel width is same W, and electrode length is L_e. At this time, the lateral resistance per unit length of the channel layer is $R=\frac{\rho_s}{W}\left[\frac{\Omega}{cm}\right]$, the longitudinal conductance per unit length between the electrode and the channel layer is, $G=\frac{w}{r_c}\,[\frac{S}{cm}]$. Assuming that the constant potential of the electrode is 0, the potential $v(x)$ and the current $i(x)$ at the position x of the channel are,

$$\frac{dv}{dx}=-iR=-\frac{\rho_s}{W}i \quad \text{(A4.1)}$$

$$\frac{di}{dx}=-Gv=-\frac{W}{\rho_c}v \quad \text{(A4.2)}$$

Taking derivative of (A4.1) and (A4.2) can be represent written in the following form respectively,

Appendix-A4

$$\frac{d^2v}{dx^2} = -\frac{\rho_s}{W}\frac{di}{dx}$$

$$or, \frac{d^2v}{dx^2} = \frac{\rho_s}{\rho_c}v \quad \text{(A4.3) using (A4.2)}$$

And similarly way, using (A4.1) we get,

$$or, \frac{d^2i}{dx^2} = \frac{\rho_s}{\rho_c}i \quad \text{(A4.4)}$$

The differential equations can be solved under the boundary condition at $x = 0; i = 0$

and $x = L_e; i = I$,

$$i(x) = I\frac{sinh(\frac{x}{L_t})}{sinh(\frac{L_e}{L_t})} \quad \text{(A4.5)}$$

$$v(x) = -I\frac{\sqrt{\rho_s\rho_c}}{W}\frac{cosh(\frac{x}{L_t})}{sinh(\frac{L_e}{L_t})} \quad \text{(A4.6)}$$

Here, $L_t = \sqrt{\rho_c/\rho_s}$, therefore, the contact resistance R_c between the point $x = L$ of the channel and the electrode is,

$$R_c = -\frac{v(L)}{i(L)} = \frac{\sqrt{\rho_s\rho_c}}{W}\frac{1}{tanh\left(\frac{L_e}{L_t}\right)} \quad \text{(A4.7)}$$

This is an expression of the Ohmic contact resistance, and if $\frac{L_e}{L_t} \gg 1$, $tanh\left(\frac{L_e}{L_t}\right) \simeq 1$. Then (A4.7) becomes,

$$R_c \simeq \frac{\sqrt{\rho_s\rho_c}}{W} \quad \text{(A4.8)}$$

L_t is an important value for designing the electrode length.

Total resistance R_T between the two electrodes as shown in Fig.A4.2 at interval L is the sum of channel resistance, $R_{sc} = \frac{\rho_s L}{W}$ between the two electrodes and two contact resistance, $2R_c$.

$$R_T = R_{sc} + 2R_c \simeq \frac{\rho_s L}{W} + 2\frac{\sqrt{\rho_s \rho_c}}{W} \quad \text{(A4.9)}$$

If we know the linear relationship between l and R_T we can determine ρ_s from the slope and R_c from the intercept, and ρ_c can be determined using equation (A4.7) or (A4. 8).

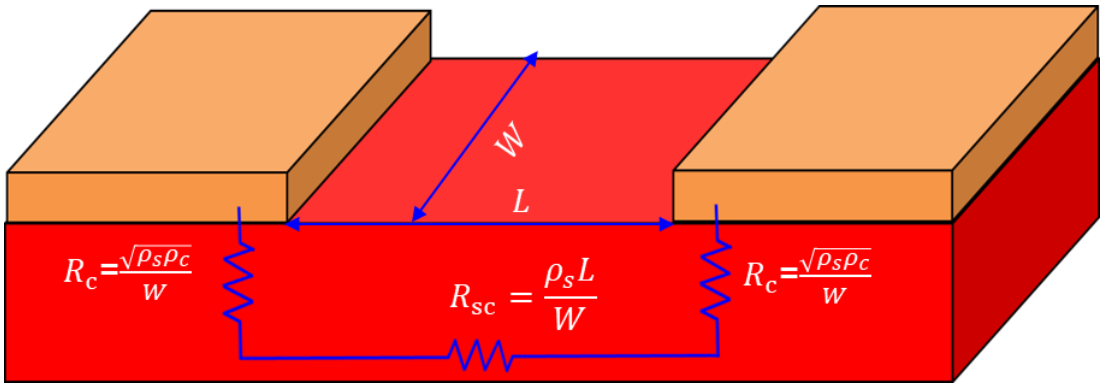

Fig.A4.2. Total resistance between two electrodes.

When $\frac{L_e}{L_t} \ll 1$, $tanh\left(\frac{L_e}{L_t}\right) \simeq \frac{L_e}{L_t}$, then, eequation (A4.7) can be written in the following approximated form,

$$R_c \simeq \frac{\rho_c}{W L_e} \quad \text{(A4.10)}$$

However, considering etched out InAs channel (~50 nm) during MnAs electrode formation, there is different InAs sheet thickness of InAs channel underneath and between electrodes.

Therefore, we have modified the TLM structure as shown in Fig.A4.3. The total resistance relation becomes;

$$R_T = R_{sc} + 2R_c \simeq \frac{\rho_{s2}L}{W} + 2\frac{\sqrt{\rho_{s1}\rho_c}}{W} \quad \text{(A4.11)}$$

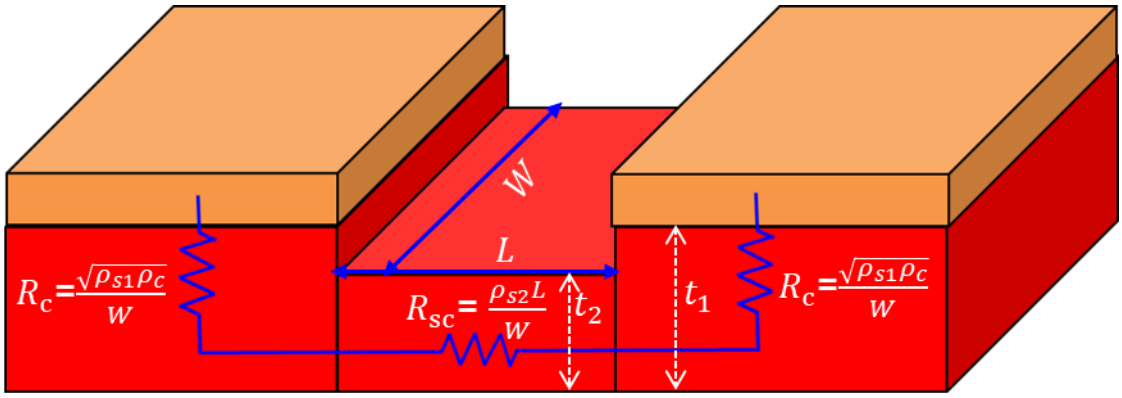

Fig.A4.3. Total resistance between two contacts in modified structure.

Hence from the measured TLM, we can know the sheet resistance (ρ_{s2}) of InAs channel between MnAs electrode and hence sheet resistance (ρ_{s1}) of InAs channel underneath MnAs electrode can be written in the form as follows:

$$\rho_{s1} = \frac{t_2}{t_1}\rho_{s2} \quad \text{(A4.12)}$$

Where, t_1 and t_2 are the InAs thickness underneath MnAs and between MnAs electrodes respectively.

Low temperature measurement system

In this study, we were carried out spin valve measurement at low temperature ~1.5 K environment using ^{4}He cryostat shown in Fig A5.1. There is superconducting magnet (SCM) placed in dewar. We can apply magnetic field up to ±8 T to a sample at variable temperature insert (VTI) unit. The VTI is connected from the Helium-dewar with needle pipe and its opening can be adjusted by the needle valve. The liquefaction temperature of ^{4}He is ~4.2 K. However, when the pressure is reduced by evacuation, the liquefaction temperature close to ~1.5 K.

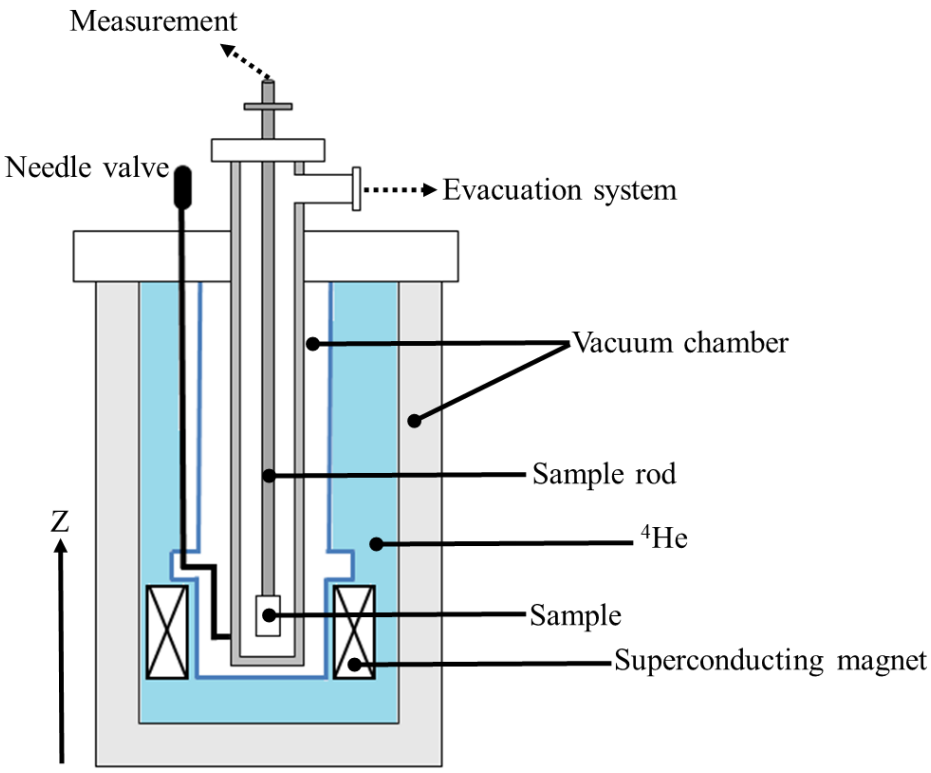

Fig. A5.1 liquid ^{4}He cryostat configuration.

We mainly measured very small signal strength at non-local spin valve (NLSV) measurement. There is possibility to suppress the measured signal by thermal noise at room temperature, electromagnetic noise from environment and so on. For this reason, at low temperature by combining an AC power supply and lock-in amplifier, we can avoid the inclusion of noise into

the measured signal. The measurement set up is shown in Fig A5.2. To keep constant current flowing to the device, a resistor of 1 MΩ and a standard resistor of 10 kΩ are connected in series. 1 MΩ resistor stabilizes the current and measure the voltage drop across the standard resistance. In the signal detection, a preamplifier, an isolation amplifier and a lock-in amplifier are connected in series. The lock-in amplifier plays act as a band pass filter and the signal component of the same period as alternating current is measured by digital multimeter, and these measuring instruments are connected in parallel by general purpose interface bus (GPIB) and control by LabVIEW programming software.

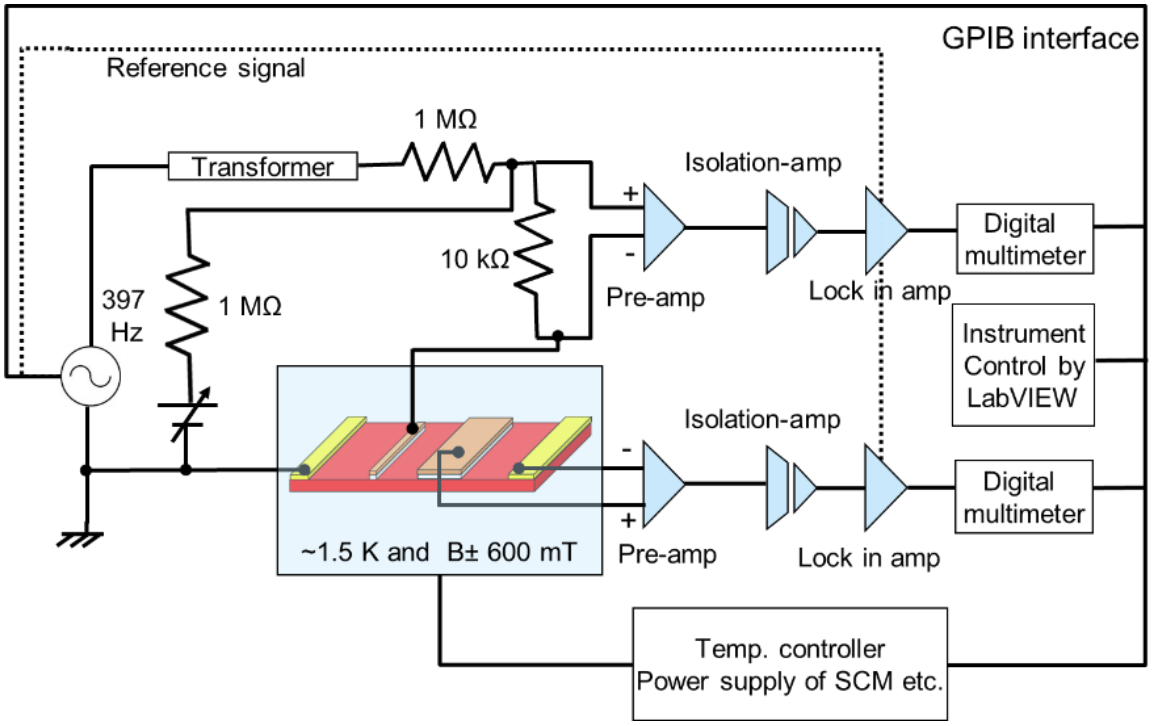

Fig. A5.2 Low temperature measurement set up.

Scientific contributions

Original paper:

1. **Md. Earul Islam** and Masashi Akabori, “In-plane isotropic magnetic and electrical properties of MnAs/InAs/GaAs(111)B hybrid structure” Physica B: Accepted (2017).
2. **Md. Earul Islam** and Masashi Akabori, “Growth and magnetic properties of MnAs/InAs hybrid structure on GaAs(111)B”, J. Cryst. Growth 463 (2017) 86.
3. Huyen T. Pham, Tam D. Nguyen, **Md. Earul Islam**, Dat Q. Tran and Masashi Akabori, “Enhanced ferromagnetism of ZnO@Co/Ni hybrid core@shell nanowires grown by electrochemical deposition method”. RSC Adv. **8** (2018) 632-639.

Technical report:

1. **Md. Earul Islam**, Cong Thanh Nguyen and Masashi Akabori, “In-plane electrical properties of MnAs/InAs/GaAs(111)B heterostructures”, IEICE Tech. Rep., vol. 115, no. 156, ED2015-43, (2015) pp. 35-38.

International conference:

Oral:

1. Huyen T. Pham, Tam D. Nguyen, Dat Q. Tran, Md. Earul Islam, **Masashi Akabori**, “Electrochemical Deposited ZnO/Magnetic-Metal Hybrid Core/Shell Nanowires for Spintronic Device Application”, 4th International Symposium on Frontiers in Materials Science, 9B-3, Greifswald, Germany, September 4-6 (2017).

2. **Md. Earul Islam,** Kazuki Hayashida and Masashi Akabori, “Simultaneous measurement of local and non-local spin-valve signals in MnAs/GaAs/InAs/GaAs(111)B hybrid structure” 6th International Symposium on Organic and Inorganic Electronic Materials and Related Nanotechnologies, PA4-2-2, Fukui, Japan, June 18-21 (2017).

3. Md. Earul Islam, Kazuki Hayashida and **Masashi Akabori**, “Molecular beam epitaxial growth of ferromagnetic-MnAs/III-As semiconductor heterostructures on (111)B surfaces for lateral spin device application” 3rd International Symposium on Frontiers in Materials Science, SS-I1.2, Hanoi, Vietnam, September 28-30 (2016).

Poster:

1. Huyen T. Pham, Dat Q. Tran, **Md. Earul Islam**, Masashi Akabori, “Electrochemical Deposition of ZnO/Magnetic-Metal Hybrid Core/Shell nanowires” 6th International Symposium on Organic and Inorganic Electronic Materials and Related Nanotechnologies, P02-54, Fukui, Japan, June 18-21 (2017).

2. **Md. Earul Islam,** Cong Thanh Nguyen and Masashi Akabori, “In-Plane Transport Properties of MnAs/InAs/ GaAs(111)B Grown by Molecular Beam Epitaxy” 2nd International Symposium on Frontiers in Materials Science, P3-26, Tokyo, Japan, November 19-21 (2015).

3. **Md. Earul Islam,** Cong Thanh Nguyen and Masashi Akabori, “Contact properties of MnAs/InAs grown on GaAs(111)B by molecular beam epitaxy” 5th International Symposium on Organic and Inorganic Electronic Materials and Related Nanotechnologies, P2-17, Niigata, Japan, June 16-19 (2015).

Domestic conference:

Oral:

1. **林田一希**、イスラムヤールル、赤堀誠志：「MnAs/GaAs/InAs ヘテロ構造を用いた横型スピンバルブ素子の作製」、平成 28 年度応用物理学会 北陸・信越支部学術講演会、B13、富山、12/10　(2016).

2. イスラムヤールル、**赤堀誠志**：「MnAs/InAs ヘテロ構造を用いた横型スピンバルブ素子の試作」、平成 27 年度応用物理学会 北陸・信越支部学術講演会、B14、長野、December 12 (2015).

3. **Md. Earul Islam,** Kazuki Hayashida and Masashi Akabori, Enhancement of non-local signal in lateral spin valve device of MnAs/III-V hybrid structure with multi ferromagnetic electrodes" Japan Society of Applied Physics branch meeting, Ishikawa, Kanazawa, Japan, E06, December 9 (2017)

Poster:

1. **Md. Earul Islam,** Kazuki Hayashida and Masashi Akabori, "Non-local spin-valve measurements in MnAs/GaAs/InAs/GaAs(111)B heterostructures" 64th Japan Society of Applied Physics Spring Meeting, 14p-P10-7, Pacifico, Yokohama, Japan, March 14-17 (2017).

2. **Md. Earul Islam,** Kazuki Hayashida and Masashi Akabori, "GaAs barrier insertion into MnAs/InAs hybrid heterostructures on GaAs(111)B for lateral spin valve device application" 77th Japan Society of Applied Physics Autumn Meeting, 13p-P8-41, Niigata, Japan, September 13-16 (2016).

3. **Md. Earul Islam,** and Masashi Akabori, “In-plane magnetic and electric properties of MnAs/InAs/GaAs(111)B” 3rd Organic and Inorganic Electronics Symposium, Ishikawa, Kanazawa, Japan, July 15-16 (2016).

4. **Md. Earul Islam,** and Masashi Akabori, “Magnetic properties and lateral spin-valve device application of MnAs/InAs/GaAs(111)B”, 63rd Japan Society of Applied Physics Spring Meeting, 19p-P1-53, Tokyo Institute of Technology, Japan, March 19-22 (2016).

5. **Md. Earul Islam,** Cong Thanh Nguyen and Masashi Akabori, “In-plane Transport Properties of MBE grown MnAs/InAs on GaAs(111)B” JAIST symposium on Advanced Science and Technology, AP-1, JAIST, Ishikawa, Japan, November 10-12 (2015).

6. **Cong Thanh Nguyen**, Md. Earul Islam and Masashi Akabori, “Molecular beam epitaxial growth of MnAs/InAs/GaAs(111)B heterostructure” 62rd Japan Society of Applied Physics Spring Meeting, 13a-P15-5, Tokai University, Japan, March 11-14 (2015).